Consequences of the thermal effects generated during fatigue crack growth on the mode one stress intensity factor

Zaid Boussattine

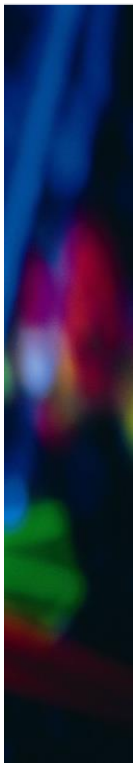

2018-ENAM-0047

École doctorale n° 432 : Sciences des Métiers de l'ingénieur

Doctorat ParisTech

T H È S E

pour obtenir le grade de docteur délivré par

l'École Nationale Supérieure d'Arts et Métiers

Spécialité " Mécanique-Matériaux "

présentée et soutenue publiquement par

Zaid BOUSSATTINE

le 12 novembre 2018

Consequences of the thermal effects generated during fatigue crack growth on the mode one stress intensity factor

Directeur de thèse : **Nicolas RANC**
Co-directeur de la thèse : **Thierry PALIN-LUC**

Jury

M. Bertrand WATTRISSE, Professeur, LMGC, Université de Montpellier	Président
Mme Catherine MABRU, Professeur, ICA, ISAE SUPAERO	Rapporteur
M. Gilbert HENAFF, Professeur, Institut Pprime, ISAE ENSMA	Rapporteur
M. Alberto CARPINTERI, Professeur, Politecnico di Torino	Examinateur
M. Nicolas RANC, Professeur, PIMM, Arts & Métiers ParisTech	Examinateur
M. Thierry PALIN-LUC, Professeur, I2M, Arts & Métiers ParisTech	Examinateur

T H È S E

Arts et Métiers ParisTech - Campus de Paris
Laboratoire Procédés et Ingénierie en Mécanique et Matériaux, Paris CNRS UMR 8006
Institut de Mécanique et d'Ingénierie, Bordeaux CNRS UMR 5295

"If you know what you are looking
for and find it, you have learned nothing.
The important thing is to find what you
did not expect. This is how science advances."

Dr. Samuel Ting, Nobel Prize in Physics 1976.

Acknowledgments

My first thanks go to my supervisors, Professor Nicolas Ranc, and Professor Thierry Palin-Luc, for their consistent support, guidance, and direction during this PhD work. They have always been there to meet with me and answer my long lists of questions, most of which began with "do you have five minutes please?", which most of the time turned into long talks. They have shown me, by their example, what a good scientist and person should be. They deserve my ultimate deep gratitude.

I am deeply grateful to all the members of the jury for agreeing to read the manuscript and participate in the defense of this thesis. Very special thanks to the reviewers for taking the time to provide quite valuable comments and suggestions.

I extend my sincere thanks to the research team DySCo of PIMM laboratory with whom I have had the pleasure to share amazing moments during my stay in their famous 'Hall 3'. Thanks also go to my colleagues: the two Maximes (one speaks too fast and the other is a good football player, they will recognize themselves!!), Alain, Eeva, Noushin, Nassim, Quentin, Hadrien, well the list is long... I will particularly miss the epic conversations about everything and nothing with Lounes and Imade, I will never forget the moments I cried laugh with these guys. I would especially like to thank Jonathan Merzeau and Mohamed El May from I2M institute for their kind welcome and availability whenever I went to I2M.

Last but not the least, nobody has been more important to me in the pursue of this PhD project than the members of my family. I would like to thank my parents whose love and support are with me in whatever I pursue. They have always been supportive of my career goals. I can not thank them enough for all what they sacrificed for me. I also want to dedicate this work to my late maternal grandfather who has always been available when I needed him, my maternal grandmother, and my aunt Zineb.

Contents

List of Figures

List of Tables

Glossary

ASTM	American Society for Testing and Materials
CCT	Center Cracked Tensile
FEA	Finite Element Analysis
IR	Infrared
LEFM	Linear Elastic Fracture Mechanics
RCPZ	Reverse Cyclic Plastic Zone
SIF	Stress Intensity Factor

List of Principal Symbols

f	Loading frequency
a	Crack half-length
a_i	Initial crack half-length at the beginning of one loading block
a_f	Final crack half-length at the end of one loading block
t	Time
t_i	Initial time of one loading block
t_f	Final time of one loading block
Δt	Cyclic loading duration
W	Half-width of the CCT specimen
L	Half-length of the CCT specimen
e	Thickness of the CCT specimen
r_p	Radius of the monotonic plastic zone
r_p^*	Radius of the reverse cyclic plastic zone
N	Number of cycles
$\frac{da}{dN}$	Fatigue crack growth rate per cycle
s_{the}	Thermoelastic coupling source
s_{the}^a	Amplitude of the thermoelastic coupling source
d_1	Intrinsic dissipation due to microplasticity
q	Heat source due to the cyclic plasticity in the RCPZ
T	Temperature
T_0	Reference temperature
θ	Temperature variation $(T - T_0)$
θ_{the}	Thermoelastic temperature variation
θ_d	Temperature variation generated by the intrinsic dissipation d_1
θ_q	Temperature variation generated by the heat source q
ΔK_{th}	Threshold for crack growth
K_c	Material toughness
E	Young's modulus

ν	Poisson's ratio
σ_y	Yield stress under quasi-static monotonic loading
$\sigma_y^{cyc.}$	Cyclic yield stress
R_m	Ultimate tensile strength
A	Material elongation after fracture
ρ	Material density
α	Thermal expansion coefficient
k	Thermal conductivity coefficient
c	Specific heat capacity
h	Convective heat transfer coefficient
$\bar{\bar{\sigma}}$	Stress tensor
$\bar{\bar{\varepsilon}}$	Strain tensor
$\bar{\bar{1}}$	Second order identity tensor
$\bar{\bar{\bar{\bar{C}}}}$	Stiffness tensor
σ_{xx}	Normal stress component along x direction
σ_{yy}	Normal stress component along y direction
σ_{zz}	Normal stress component along z direction
τ_{xy}	Shear stress component in the (x, y)-plane
u_x	Displacement component along x direction
u_y	Displacement component along y direction
u_z	Displacement component along z direction
$\Delta\sigma$	Stress range under cyclic loading
σ_m	Mean stress under cyclic loading
σ_{max}	Maximum stress per cycle
σ_{min}	Minimum stress per cycle
R	load ratio
K	Stress intensity factor
K_I	Mode I stress intensity factor
K_{II}	Mode II stress intensity factor
K_{III}	Mode III stress intensity factor
ΔK	Stress intensity factor range
ΔK_I	Mode I stress intensity factor range
ΔK_{I_i}	Applied SIF range at the beginning of one loading block
ΔK_{I_f}	Applied SIF range at the end of one loading block
$K_{I_{max}}$	Maximum SIF over a load cycle
$K_{I_{min}}$	Minimum SIF over a load cycle
K_I^m	Mean SIF under cyclic loading

$K_{I_{temp}}^{the}$	Thermal correction of the SIF due to the thermoelastic coupling
$K_{I_{temp}}^{d}$	Thermal correction of the SIF due to the intrinsic dissipation related to microplasticity
$K_{I_{temp}}^{q}$	Thermal correction of the SIF due to the cyclic plastic dissipation in heat in the RCPZ
$K_{I_{temp}}$	Total thermal correction of the SIF
$K_I^{corr,the}$	SIF corrected by taking into account the thermoelastic coupling effect
$\Delta K_I^{corr,the}$	SIF range correction due to the thermoelastic coupling effect
$K_{I_{min}}^{corr,the}$	Minimum SIF over a load cycle corrected by taking into account the thermoelastic coupling effect
$K_{I_{max}}^{corr,the}$	Maximum SIF over a load cycle corrected by taking into account the thermoelastic coupling effect
$R^{corr,the}$	Load ratio near the crack tip corrected by taking into account the effect of the thermoelastic coupling
$K_I^{corr,d}$	SIF corrected by taking into account the effect of the intrinsic dissipation due to microplasticity
$K_{I_{min}}^{corr,d}$	Minimum SIF over a load cycle corrected by taking into account the effect of the intrinsic dissipation due to microplasticity
$K_{I_{max}}^{corr,d}$	Maximum SIF over a load cycle corrected by taking into account the effect of the intrinsic dissipation due to microplasticity
$R^{corr,d}$	Load ratio near the crack tip corrected by taking into account the effect of the intrinsic dissipation due to microplasticity
$K_I^{corr,q}$	SIF corrected by taking into account the effect of the cyclic plastic dissipation in heat in the RCPZ
$K_{I_{min}}^{corr,q}$	Minimum SIF over a load cycle corrected by taking into account the effect of the cyclic plastic dissipation in heat in the RCPZ
$K_{I_{max}}^{corr,q}$	Maximum SIF over a load cycle corrected by taking into account the effect of the cyclic plastic dissipation in heat in the RCPZ
$R^{corr,q}$	Load ratio near the crack tip corrected by taking into account the effect of the cyclic plastic dissipation in heat in the RCPZ
K_I^{corr}	Global SIF corrected by the overall thermal corrections
$K_{I_{min}}^{corr}$	Minimum value of the global SIF corrected over a load cycle
$K_{I_{max}}^{corr}$	Maximum value of the global SIF corrected over a load cycle
R^{corr}	Ratio between the minimum and maximum values of the corrected global SIF

Introduction

The risk of failure has always been associated with the use of metallic materials in structures. The failure of a mechanical component can happen through different scenarios and cause large scale losses, both financial and human, as well as serious damage to the environment, for example aircraft crashes, the failure of nuclear reactors, the burst of big pipelines, or the collapse of large bridges. Fatigue cracking in metals is considered as one of the major causes which can lead to the failure of a mechanical component. It is mainly due to the presence of cracks which occur further to eventual manufacturing defects or a stress concentration zone, and propagate during service when the component is subjected to cyclic loading.

The use of fracture mechanics analysis has proven to be a powerful tool to understand fatigue crack extension and is of interest for assessing the use life of structures. Since the 1950s, fracture mechanics has always been a fascinating branch of research in mechanics and materials. It involves the analysis of the stress and strain in a cracked solid, by using a theoretical concept named the K-concept or the concept of stress intensity factor. The use of this concept for studies of fatigue cracking was shown to be of special value to make estimates of the danger of fatigue crack growth by small initial cracks due to cyclic loading during periods of use in service. Moreover, the development of experimental and numerical techniques has enabled engineers and researchers to improve the use of fracture mechanics concepts for studying potential of real fatigue cracks in various complex structural locations.

Of course, the appearance and propagation of fatigue cracks in a metallic structure is an undesirable fact. The role of fracture mechanics concepts is also to provide tools enabling to predict the behavior of fatigue crack propagation through the establishment of physical crack growth laws from calibration tests, commonly named fatigue crack growth tests. These tests, carried out with cracked specimens at room temperature (when the ambient temperature is not of interest), have always been considered as isothermal, in other words, the temperature of the cracked specimen is supposed to remain **constant** and **uniform** during the tests. However, it is well known in the literature that plasticity occurs at the crack tip and mostly converts

into **heat**. As a consequence, this heat generates a temperature field which modifies the temperature of the cracked specimen. Then, the assumption of isothermal fatigue crack growth tests is called into question. In addition, with recent developments of infrared imaging techniques, the generated temperature field at the crack tip turned out to be **heterogeneous**, which confirms the questioning about isothermal fatigue crack growth tests.

The purpose of the work undertaken during this PhD thesis is to estimate the consequences of the heat produced at the tip of a long propagating fatigue crack, on the fracture mechanics concept of stress intensity factor since this is the key parameter for simulating crack extension. Dealing with this problematic is complex and requires a relevant scientific approach of problem-solving since it involves different aspects in fracture mechanics, fatigue of materials, and heat transfer. Moreover, the background literature about the heat produced at the tip of a fatigue crack contains very few studies (mainly [Pippan and Stüwe, 1983]). Many researchers have studied the thermal effect that the heat at the crack tip could produce, but they only focused on the case of a monotonic loading (for instance in [Döll, 1973], or [Fuller and Fox, 1975]). In fatigue, the problem is more complicated since under cyclic loading, cyclic plasticity accumulates at the crack tip, and can depend on several phenomena which appear in fatigue, such us underloads or overloads on the crack, crack closure, and material cyclic behavior. For this purpose, this PhD work, funded by a French ministerial allocation with the support of Arts & Métiers ParisTech, is a joint work which brings together the expertise of the laboratory of Processes and Engineering in Mechanics and Materials (PIMM, Paris), and the Institute of Mechanics and Mechanical Engineering (I2M, Bordeaux).

Prior to this work, Professor Nicolas Ranc from PIMM, and Professor Thierry Palin-Luc from I2M, have initiated a study about the effects of the heat generated at the tip of a fatigue crack on the stress intensify factor. Indeed, in [Ranc et al., 2011], they analytically studied the effect of the heat, produced at a fatigue crack tip, on the stress intensity factor in the case of a sem-infinite propagating fatigue crack in an infinite cracked plate. Subsequently, in [Ranc et al., 2014], they carried out the same study with a finite center-cracked plate where they first proposed a method to estimate the heat dissipated from cyclic plasticity at the crack tip, and then they computed the resulting effect on the stress intensity factor.

The goal of this PhD work was initially the further development of the investigation previously initiated by Prof. Nicolas Ranc and Prof. Thierry Palin-Luc, but the presence of additional thermal effects, produced during fatigue crack growth tests, broadens the investigation to study the associated resulting consequences on

the stress intensity factor. In this dissertation, Chapter I gives a review of the background information relevant to the work carried out in this thesis, namely fracture mechanics concepts, fatigue crack propagation, and dissipative mechanisms produced at the tip of a long crack during its propagation. Additional literature review is discussed as we go along the following chapters. Chapter II explains the origins of thermal effects generated during fatigue crack growth as well as the instrumentation and methods enabling to characterize and quantify these effects. Afterward, Chapter III contains the methodology, as well as the development, of calculations leading to achieve the goal of this work. Finally, Chapter IV initiates potential further studies aiming at exploring the effect of the loading frequency, as well as the effect of the material behavior, on the heat dissipated at the tip of a long propagating fatigue crack, which may consequently impact the stress intensity factor.

Before delving into the content of this thesis, it should be mentioned that all the calculations involved in the thermal and the mechanical problems presented in this thesis, are done with a home-made Matlab code, developed within the scope of this work, which uses specific two-dimensional finite elements in heat transfer analysis as well as a specific post-treatment of the stress intensity factor.

Chapter 1

Background and literature review

Contents

Ce premier chapitre présente les notions essentielles de la mécanique de la rupture et de la propagation des fissures de fatigue qui serviront de support et de cadre théorique pour le reste du mémoire. Les concepts clés dans le cadre de la mécanique élastique linéaire de la rupture sont premièrement définis, notamment le champ des contraintes au voisinage d'une fissure, le facteur d'intensité des contraintes, la plasticité confinée en pointe de fissure, et le concept de la zone de plasticité cyclique.

Ensuite, l'application de ces concepts dans le domaine de la propagation des fissures de fatigue est présentée à travers l'exemple de la loi classique dite de Paris. L'accent est mis par la suite sur les effets qui apparaissent en sollicitation cyclique et qui peuvent modifier cette loi de propagation, en particulier les effets associés au rapport de charge et au phénomène de la fermeture de la fissure.

Enfin, les travaux en lien avec ce travail sont présentés afin de situer les objectifs de ce travail par rapport à ce qui a été antérieurement fait dans la littérature.

Il est à noter qu'en plus des éléments de la littérature présentés dans ce premier chapitre, d'autres passages bibliographiques sont présentés au fur et à mesure de l'avancement des parties de ce mémoire, et ce en fonction de l'objectif de chaque partie.

In this first chapter, the main knowledge of fracture mechanics and fatigue crack propagation is presented. It serves as theoretical framework of this dissertation. The key concepts within the linear elastic fracture mechanics are first defined. That concerns the crack tip stress field, the stress intensity factor, the small scale yielding, and the concept of the reverse cyclic plastic zone.

These concepts are afterward used to present the field of fatigue crack growth through the example of the classical law of Paris. The emphasis is made on the effects that appear when a cracked structure is loaded in fatigue, particularly the effect related to the loading ratio and that associated with crack closure phenomena. These effects can actually modify the Paris law.

Finally a background literature is presented in order to set the goal of this PhD work in relation to what has previously done in the literature.

It should be mentioned that besides the literature review presented in this first chapter, additional bibliographic elements are discussed through the following parts of this dissertation, depending on the aim of each part.

1.1 Fracture mechanics issues

Fracture mechanics covers the analysis of the response of materials in the presence of cracks. It is aimed at assessing the stress and strain fields in the vicinity of cracks and establishing experimental procedures in order to determine the kinetics of propagation of cracks as well as their critical size beyond which, under a given loading, the unstable fracture occurs. It is possible to distinguish two aspects of fracture mechanics: the aspect of stress analysis in terms of quantifying the stress fields at the crack tip, and the aspect of material behavior in terms of defining the fracture strength and the resistance to the imposed loading.

A concrete knowledge of the fracture mechanisms of materials was first presented by Griffith in 1920, [Griffith, 1920]. Griffith explained the problem of the rupture of elastic solids by an approach based on energy-balance. Indeed, according to [Poynting and Thomson, 1913], the equilibrium state of an elastic solid body, deformed by specified surface forces, is such that the potential energy of the whole system is a minimum. Griffith's criterion of rupture is obtained by adding the statement that the equilibrium position, if equilibrium is possible, must be one in which rupture of the solid has occurred, if the system can pass from the unbroken to the broken condition by a process involving a continuous decrease in potential energy. When a crack occurs, Griffith defined the surface energy as the rate of loss of stress field energy per unit of new separation area. However, the surface energy is unrealistically high for ductile materials and the usual training in stress analysis did not provide methods of estimating this energy, that is why Griffit's theory was ignored until the 1950s. From a stress analysis standpoint, [Irwin, 1957] proposed a relatively simple method of crack-stress field analysis for linear elastic solids, which allowed to show that the severity of the stress field near the crack tip, tending to cause crack extension, could be represented by a stress intensity factor (SIF), K.

According to [Tada et al., 1973], for linear elastic bodies, the intensity of the local stress field at the crack tip can be affected by: (i) the surfaces of the crack as they are the nearby and stress-free boundaries of the cracked body, (ii) the mechanical loading, and (iii) other eventual remote boundaries. The surfaces of the crack are the dominating influence on the distribution of stresses in the vicinity of the crack. The stress fields near crack-tips can be decomposed into three types, each associated with a local mode of loading as shown in Figure 1.1.

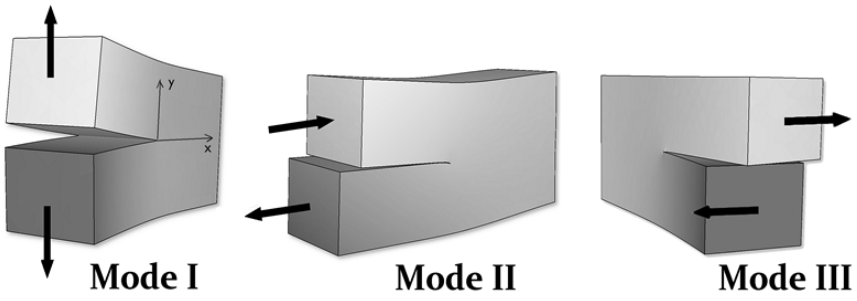

Figure 1.1: Modes of crack loading.

Irwin's linear elastic fracture mechanics (LEFM) approach defines the stress intensity factors K_I, K_{II} and K_{III} from the surrounding crack-tip stress fields associated with each mode. It is based on Westergaard's work presented in [Westergaard, 1939]. For mode I, which is of interest in this thesis, the fields of crack tip stress and displacement are respectively written in Equations (1.1) and (1.2), with plane strain hypothesis, by referring to Figure 1.2 for notation.

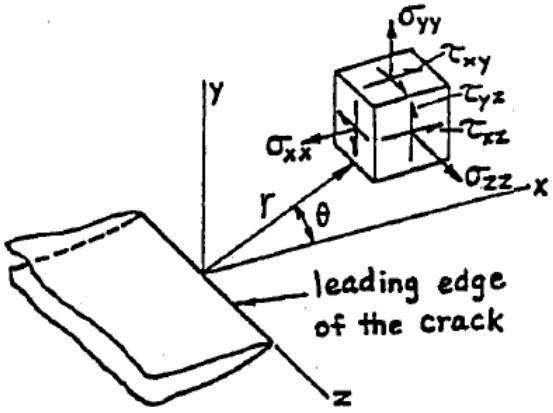

Figure 1.2: Coordinates from leading edge of a crack and stress components in the crack-tip stress field, [Tada et al., 2000].

For $r << a$:

$$\begin{Bmatrix} \sigma_{xx} \\ \sigma_{yy} \\ \tau_{xy} \end{Bmatrix} = \frac{K_I}{\sqrt{2\pi r}} \begin{Bmatrix} \cos(\frac{\theta}{2})[1 - \sin(\frac{\theta}{2})\sin(\frac{3\theta}{2})] \\ \cos(\frac{\theta}{2})[1 + \sin(\frac{\theta}{2})\sin(\frac{3\theta}{2})] \\ \sin(\frac{\theta}{2})\cos(\frac{\theta}{2})\cos(\frac{3\theta}{2}) \end{Bmatrix}, \tag{1.1}$$

for plane strain: $\sigma_{zz} = \nu(\sigma_{xx} + \sigma_{yy})$, $\tau_{xz} = \tau_{yz} = 0$, and:

$$\begin{Bmatrix} u_x \\ u_y \\ u_z \end{Bmatrix} = \frac{E}{K_I}\sqrt{\frac{r}{2\pi}} \begin{Bmatrix} \cos(\frac{\theta}{2})[1 - 2\nu + \sin^2(\frac{\theta}{2})] \\ \sin(\frac{\theta}{2})[2 - 2\nu - \cos^2(\frac{\theta}{2})] \\ 0 \end{Bmatrix}. \tag{1.2}$$

For plane stress hypothesis, Equations (1.1) and (1.2) can be rewritten by taking $\sigma_{zz} = 0$ and replacing Poisson's ratio, ν, in the displacements with $\frac{\nu}{1+\nu}$. Equation (1.1) shows the characteristic singularity in elastic solutions defining the stress fields near and around the crack tip. In a more generic form, the opening mode stress intensity factor, K_I, can be expressed as:

$$K_I = \sigma\alpha\sqrt{\pi a}, \tag{1.3}$$

where σ is the nominal stress remote from the crack tip, a is the crack length, and α is a geometrical function which accounts for effects of boundaries or other cracks, orientations of the crack, shape of the crack and the restraints on the structure containing the crack. It is with the determination of this geometrical function that crack analysis methods are concerned.

As the LEFM approach to determine the SIF became crucial to solve problems of engineering design, a series of handbooks were written to list complete SIF solutions for typical cracked structures and loadings. Some of these handbooks: [Sih, 1973], [Tada et al., 1973], [Rooke and Cartwright, 1976], and [Murakami, 1987]. For instance, for the typical geometry of a finite two-dimensional center-cracked tensile (CCT) plate, which is used in this doctoral work, subjected to a uni-axial and uniform nominal stress, σ, at its extremities as presented in Figure 1.3, the elastic SIF solution is given by Equation (1.4), [Tada et al., 1973], which is one of the asymptotic approximations to calculate the SIF in linear-elastic response.

$$K_I = \sigma\ \sqrt{\pi a}\ 0.5\left(3 - \frac{a}{a+r}\right)\left(1 + 1.243\left(1 - \frac{a}{a+r}\right)^3\right), \tag{1.4}$$

where a is the half-length of the crack, and r is the radius of the central whole.

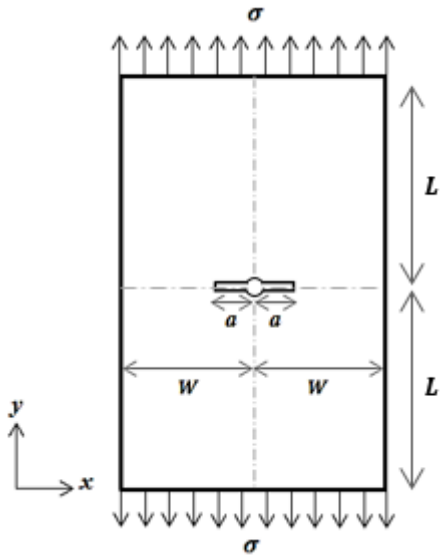

Figure 1.3: Illustration of a finite two-dimensional center-cracked tensile plate.

There are many other methods that were developed for determining solutions of the SIF for linear-elastic cracked solids subjected to arbitrary loading conditions, such as the methods of the complex stress-functions provided in the book of [Muskhelishvili, 1953], the techniques of integral calculation involving the J-integral method in [Rice, 1968], the weight functions method in [Bueckner, 1970] and the Green's functions method in [Cartwright and Rooke, 1980], about which more will be said in Section §3.1 of Chapter III. In all cases where a solution for the SIF cannot be obtained from existing methods, the technique of finite element analysis (FEA) can be used ([Byskov, 1970], [Tracey, 1971]).

It must be pointed out that the LEFM framework is based on two fundamental statements: (i) the inelastic behavior at the crack tip is of no major influence on the elastic stress field near the crack, this leads to introduce the "small scale yielding" assumption which is defined afterward, (ii) the surrounding elastic crack tip stress fields are identical for two configurations if their SIF are equal, and if material elastic properties are identical ([Tada et al., 2000]). Indeed, when a crack is loaded, a plastic zone takes place at the tip of the crack. This plastic zone size establishes a geometric dimension indicating the region over which deviations from elastic behavior occur. Figure 1.4 depicts the shape of the plastic zone computed by FEA according to Von Mises criterion ([Brocks, 2017]). Under the hypothesis of plane stress, the plastic zone size is larger than that computed under the hypothesis of plane strain, and the plane stress hypothesis is adapted to define the crack tip stress field on the outer surfaces of the specimen, while the plane strain hypothesis is considered for

describing the crack tip stress field in the core of the crack front.

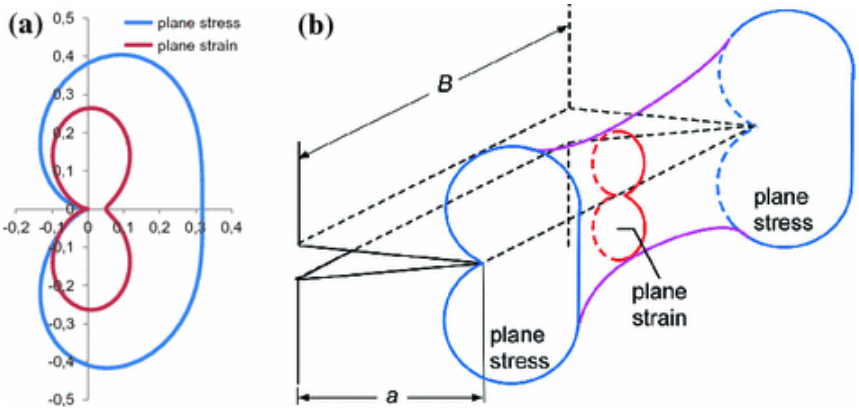

Figure 1.4: Shape of the plastic zone at the crack tip ([Brocks, 2017]): (a) under the assumptions of plane stress and plane strain; (b) illustration of the stress state along the crack front.

When the plastic zone size is small compared to the characteristic length associated with the elastic stress field such as crack length, uncracked width of a finite specimen, distance from crack tip to points of load application, and so forth, the situation is called small scale yielding, [Rice, 1967].

Within this situation, analytic rough estimates of the size of the plastic zone are obtainable by assuming a circular shape of the plastic zone as illustrated in Figure 1.5.

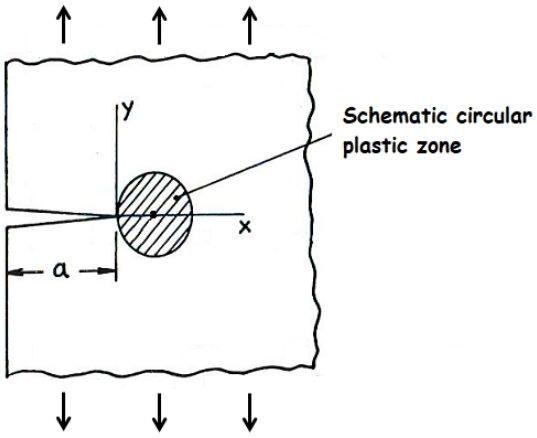

Figure 1.5: Schematic plastic zone ahead of the crack tip.

[Irwin, 1960] proposed an estimation of the size of the plastic zone where he suggested that the elastic stress field beyond the plastic zone is the same as the

one which would be present in the singular linear-elastic solution with the crack tip advanced by the distance $OB - OA$ as shown in Figure 1.6.

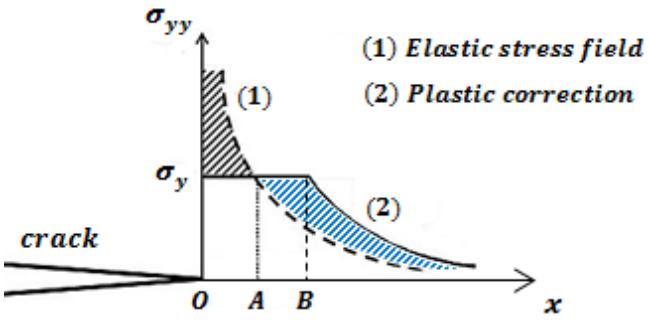

Figure 1.6: Estimation of the plastic zone size, according to Irwin's model, for an elastic perfectly plastic material under monotonic tensile load.

Assuming the plane stress hypothesis, the size of the plastic zone, schematized by a disc whose center is the point A and diameter is the distance OB, is obtained by equalizing the hatched areas of Figure 1.6.

$$\int_O^A \frac{K_I}{\sqrt{2\pi x}} dx - \sigma_y OA = \sigma_y (OB - OA), \tag{1.5}$$

with $OA = \frac{1}{2\pi}(\frac{K_I}{\sigma_y})^2$ according to the crack tip stress field solution given by Equation (1.1) after considering the plane stress hypothesis. Thus:

$$OB = \frac{K_I}{\sigma_y}\sqrt{\frac{2OA}{\pi}}, \tag{1.6}$$

$$= \frac{1}{\pi}\left(\frac{K_I}{\sigma_y}\right)^2. \tag{1.7}$$

In another approach based on cohesive forces principle and developed by [Dugdale, 1960]:

$$OB = \frac{\pi}{8}\left(\frac{K_I}{\sigma_y}\right)^2. \tag{1.8}$$

Although different approaches were used to model the plastic zone size, they give close approximations as shown in Table 1.1.

	Irwin	Dugdale
$\frac{OB}{\left(\frac{K_I}{\sigma_y}\right)^2}$	0.318	0.393

Table 1.1: Comparing estimations of Irwin and Dugdale about the size of the plastic zone with a circular shape.

In the case of cyclic loading, the problem of characterizing the plastic zone becomes more complex since it may depend on several effects such as the effect of underloads or overloads on the crack, or the effect of the material cyclic behavior. Moreover, additional quantities related to cyclic loading of a crack should be defined, such as the SIF range, $\Delta K_I = K_{I_{max}} - K_{I_{min}}$, the ratio $R = \frac{K_{I_{min}}}{K_{I_{max}}}$, and the mean stress intensity factor, $K_I^m = \frac{K_{I_{max}} + K_{I_{min}}}{2}$.

To simplify the problem of characterizing the plastic zone under cyclic loading, the hypothesis of a circular plastic zone is considered within small scale yielding condition. The hypothesis of plane stress can be considered for instance. The estimations of the plastic zone size in the case of a monotonic loading presented above can be used to treat the response to cyclic loading through the plastic superposition method developed by [Hult and McClintock, 1956] and [Rice, 1965]. Indeed, according to [Rice, 1967], when a cracked body is loaded by a system of forces proportional to some parameter F, and that the loading parameter is reduced by ΔF to a lower level $F - \Delta F$, a reverse plastic flow takes place with the first increment of load reduction, creating a new plastic zone of reversed deformation included in the plastic zone accompanying the original loading. This new yielding zone is called the reverse cyclic plastic zone (RCPZ). Figure 1.7 illustrates this phenomenon for an elastic perfectly plastic material.

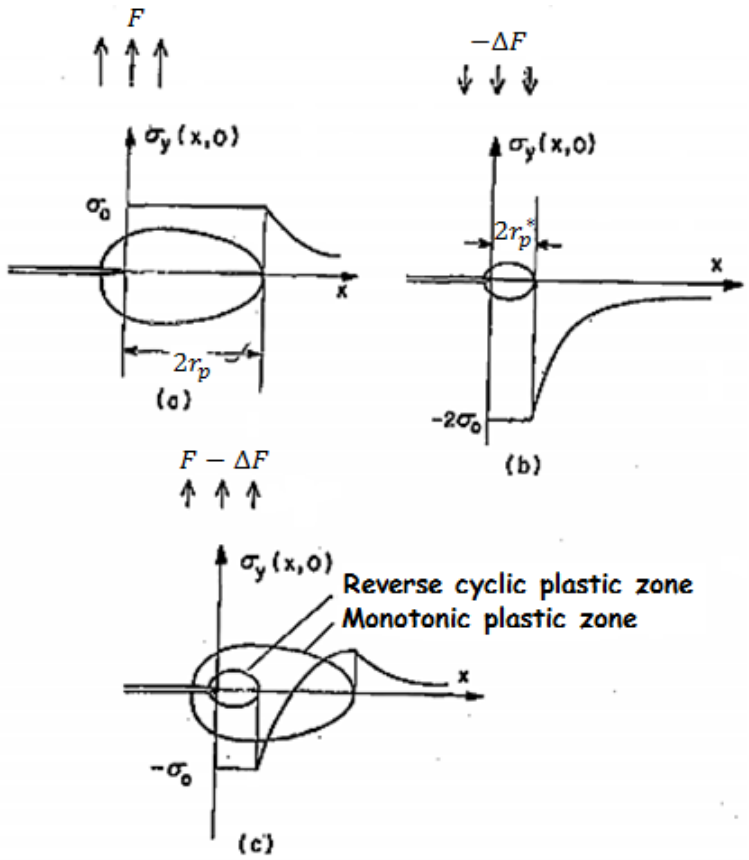

Figure 1.7: Plastic superposition principle: Adding (b) for load $-\Delta F$ with a doubled yield stress to (a) gives the solution (c) resulting after unloading from F to $F-\Delta F$. Reloading $F-\Delta F$ to F restores (a), [Rice, 1967].

[Rice, 1967] explains that, after the first loading step, the effect of unloading is to reverse the direction of stresses without affecting their magnitude or distribution when flow is proportional. The changes in stresses, strains, and displacements due to load reduction are then given by a solution identical to that for original monotonic loading, but with the loading parameter replaced by the load reduction ΔF and the yield strain and stress replaced by twice their values for original loading, so that stresses have the correct magnitude and direction in the RCPZ when the changes due to load reduction are subtracted from the distributions corresponding to the original monotonic loading. Therefore, Rice estimates the diameter of the RCPZ as one-quarter of that estimated by Irwin for the plastic zone under monotonic loading, and that by replacing the SIF, K_I, and the yield stress, σ_y, in Equation (1.7) (in plane stress for example) by the SIF range, ΔK_I, and the cyclic yield stress, $\sigma_y^{cyc.}$,

respectively, which gives the following approximation:

$$2{r_p}^* = \frac{1}{4\pi}\left(\frac{\Delta K_I}{\sigma_y^{cyc.}}\right)^2, \tag{1.9}$$

where r_p^* denotes the radius of the RCPZ. It should be noted here that this equation is an analytic approximation of the diameter of the RCPZ modeled by a disc ahead of the crack tip under the hypothesis of plane stress.

When the effects of yielding are not negligible, *i.e.* large scale yielding case, the small scale yielding condition as well as the concept of the SIF defined by the LEFM are no longer valid. In such a case, the problem becomes non-linear and the characterization of the plastic zone, either under monotonic loading or cyclic loading, can not be done with an analytic approach, because it requires the definition of new boundary conditions around the zone of plasticity, which is complicated and needs a numerical implementation of a non-linear calculation.

Within the scope of this PhD work, the main problem deals with solving the SIF in linear elasticity for a fatigue crack. Therefore, the small scale yielding condition must be fulfilled. By considering the plane stress hypothesis for simplifying the problem, the estimation of the size of the RCPZ, even with a first order approximation as Rice's estimation based on Irwin's model with a circular RCPZ (Equation (1.9)), enables to verify the validity of the small scale yielding condition where the diameter of the RCPZ should be small compared to the crack ligament.

1.2 Bridge between fracture mechanics and fatigue crack propagation

After defining the items of fracture mechanics required for solving the problem of this thesis, namely, the elastic crack tip SIF, and the estimation of the size of the RCPZ created ahead of the crack tip enabling to verify the condition of small scale yielding, it is now important to define the framework of crack growth due to fatigue from the point of view of fracture mechanics.

Fatigue is actually caused by repeated cycling of the load. A structure subjected to cyclic loads develops a crack which usually grows slowly until it reaches a critical size. At this point, the solid undergoes sudden failure and fractures.

At the beginning of the 1960s, numerous researchers became aware that the methods of Irwin's fracture mechanics could be applied to fatigue crack growth.

They have therefore based their studies on the LEFM approach to understand and model the fatigue crack growth process. Several laws, mainly based on empirical representations fitting experimental data, were established to predict the fatigue crack propagation behavior. Hereinafter, the background about fatigue crack growth process is discussed.

1.2.1 Fatigue crack propagation behavior

The first crack propagation model was proposed before Irwin's work on the SIF. It dates back to 1953 when [Head, 1953] employed a mechanical model considering rigid plastic work hardening elements ahead of a crack tip and elastic elements over the remainder of an infinite body. Head's model considered the plastic zone size constant during crack propagation, and took into account its effect on the fatigue crack growth rate. However, this model was based on a limited amount of data and required extensive calculations and deductions. That is why, [Paris and Erdogan, 1960] showed within the LEFM approach, with a wide range of data, that the propagation under cyclic loading of a long fatigue crack could be modeled by a mathematical correlation between the fatigue crack growth rate, $\frac{da}{dN}$, and the SIF range, ΔK, which is commonly known as the Paris' law:

$$\frac{da}{dN}(s) = \lambda.(\Delta K(s))^m, \tag{1.10}$$

with s is the curvilinear abscissa of a current point of the crack front, λ and m are experimental constants that depend on the material and the fatigue crack growth test conditions (R-ratio, environment, etc.). When the cracked specimen is thin and flat, it can be assumed that the crack grows with the same rate along the front, in other words, the curvilinear abscissa s disappears in Equation (1.10).

Experimental measurements of the fatigue crack growth rate, $\frac{da}{dN}$, for a fixed R-ratio, in relation to the SIF range, ΔK, enable to plot the fatigue crack growth curve, as depicted in Figure 1.8, where three stages can be distinguished: (i) crack initiation, (ii) progressive crack propagation across the structure, and (iii) quick propagation with final sudden fracture of the remaining cross section. Indeed, when ΔK reaches a threshold value, ΔK_{th}, the crack starts to propagate at low speeds at first. Then, by increasing ΔK, the crack progressively grows until the last stage where its velocity grows very quickly before the final fracture. The break is reached when the value of the applied maximum SIF over one load cycle, K_{max}, reaches the toughness of the material, K_c. The Paris' law, Equation (1.10), is only valid in the

second stage of crack propagation where $\log(\frac{da}{dN})$ varies linearly against $\log(\Delta K)$.

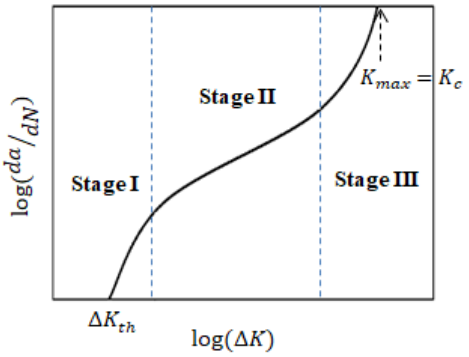

Figure 1.8: Generalized fatigue crack growth rate curve showing the three major crack growth stages.

In general, all available fatigue crack propagation models, based on the conditions of the LEFM, can be classed into three groups: the first one consists of the most primitive model represented by the Paris' law, Equation (1.10). This group does not consider the effect of the load ratio R. Moreover as ΔK tends toward ΔK_{th}, the Paris' law overestimates the crack growth rate $\frac{da}{dN}$. The second group, represented by [Broek and Schijve, 1963], has therefore tried to modify Equation (1.10) in order to correct this overestimation of $\frac{da}{dN}$ at lower ΔK by integrating parameters such as R or K_{max}. The third group is represented by [Saxena et al., 1979] with the Three-Component (TC) model considering the R-ratio effect and covering the stages I and III of fatigue crack growth.

However, no suitable explanation for the R-ratio effect was found until Elber proposed the concept of "crack closure" ([Elber, 1970]).

1.2.2 Effects of crack closure and R-ratio on fatigue crack propagation

Elber observed that the tip of a fatigue crack experienced a modified stress range compared to that calculated from the nominal applied stress, due to a phenomenon of crack closure at some load higher than the minimum of the loading cycle. Indeed, he noticed that a fatigue crack in a finite specimen subjected to zero-to-tension loading is fully open for only a part of the loading cycle. The stress at which the fatigue crack opened fully, σ_{op}, is about 50% of the maximum stress, σ_{max}, for the material he studied (2024-T3). To follow up his studies on the effect of crack

closure on the fatigue crack growth rate, [Elber, 1971] postulated that crack closure is caused by the residual plastic tensile deformation left in the wake of the fatigue crack extension, as shown schematically in Figure 1.9, which reduces crack opening by creating compressive stresses at the crack tip, and results in crack closure during unloading.

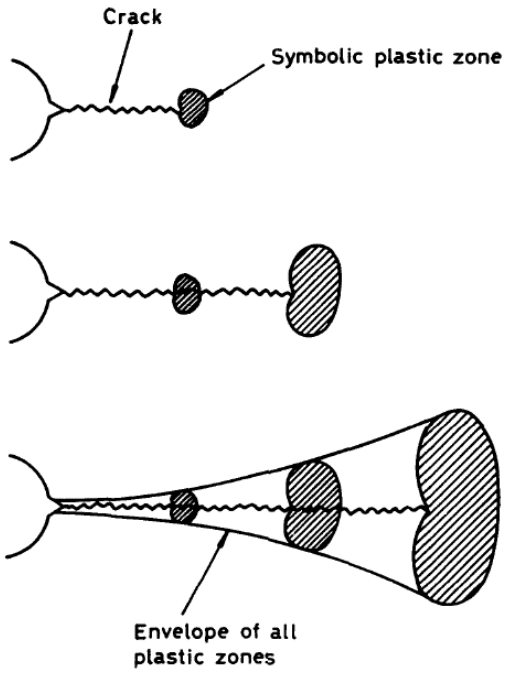

Figure 1.9: Development of a RCPZ envelope around a fatigue crack, [Elber, 1971].

Therefore, Elber differentiated between the crack opening SIF, K_{op}, and the crack closure SIF, K_{cl}, for the loading and unloading half cycles respectively. He proposed that the crack tip SIF range, ΔK, would be replaced with an effective SIF range, ΔK_{eff}, such that $\Delta K_{eff} = K_{max} - K_{op}$ as illustrated in Figure 1.10.

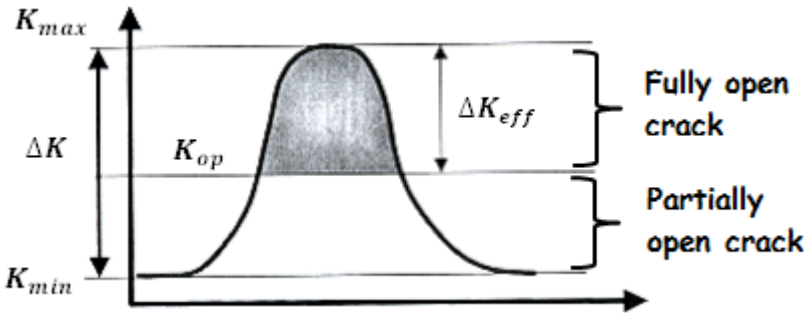

Figure 1.10: Defining the effective SIF range ΔK_{eff} according to Elber.

Furthermore, Elber established a relationship between the effective SIF range, ΔK_{eff}, and the SIF range, ΔK, through a factor, U, as defined by Equation (1.11).

$$\Delta K_{eff} = U\Delta K. \tag{1.11}$$

For the material he studied, he found a linear relationship between U and the R-ratio: $U \approx 0.5 + 0.4R$ for $-0.1 < R < 0.7$.

As a result, the Paris'law (Equation (1.10)) should be corrected according to Elber's effective SIF range as follows:

$$\frac{da}{dN}(s) = \lambda.(\Delta K_{eff}(s))^m. \tag{1.12}$$

The importance of Elber's work in practical fatigue situations has gradually become recognized. For example, the effect of changing the R-ratio, the effect of a short crack geometry, low ΔK crack growth (near-threshold) effects, and retardation due to an overload ([Gan and Weertman, 1983]), have been recognized as involving crack closure mechanisms which modify the SIF range experienced by the crack tip and hence the crack growth rate.

Indeed, the effect of the R-ratio may generate a work of friction resulting from eventual rubbing of contacting regions along the crack faces. Although cracked specimens are cyclically loaded in tension, crack closure may occur at low R-ratios, typically $R < 0.3$ as reported by [Shih and Wei, 1974] for a Ti-6Al-4V alloy. Similar results were obtained by [Katcher and Kaplan, 1974] on Ti-6A-4V alloy and 2219-T851 aluminium, namely, that the crack closure was observed at approximately $R \approx 0.32$.

It is well known that the fatigue crack propagation behavior exhibits a strong dependence upon the load ratio R, especially when decreasing the SIF range ΔK to lower values than the threshold ΔK_{th}, [Ritchie, 1979]. In the usual stage II of crack growth, this dependence upon R is generally not as considerable as that observed in stage I, [Suresh et al., 1979]. Furthermore, [Ohta et al., 1978] showed that for $R \geq 0.4$, the crack closure phenomena, in HT80 steel and SUS304 stainless steel, starts to be less pronounced with respect to loading ranges $\Delta K \leq \Delta K_{th}$. But, for $\Delta K \geq \Delta K_{th}$ in stage II, the crack closure does not occur. For $R = 0.8$, they reported that the crack was fully open over the whole applied SIF ranges. [Suresh et al., 1979] obtained, with SA387-steel, that from $R = 0.5$ the crack closure has no effect on the fatigue crack growth behavior.

Therefore, there is not a fixed standard R value above which it could be said

that the crack closure would not occur. This strongly depends on the material and also on the surrounding environment during fatigue tests (for example vacuum or air, [Cooke et al., 1975]). Within the scope of this work, the fatigue crack growth tests are carried out in the stage II of crack growth with a long fatigue crack for $R = 0.1$, $R = 0.4$ and $R = 0.6$. Moreover, they are carried out under the mode I of crack loading where friction due to contact of crack faces is not as important as that occurring in modes II and III. *For this reason, the effect of the work of friction due to crack closure in the crack tip region is not taken into account in this work.*

1.2.3 Plastic work effect ahead of a long propagating fatigue crack

Since Elber's discovery of the effect of plasticity-induced crack closure on fatigue crack growth rate, other mechanisms in the fatigue crack propagation process were studied, such as the effect of the plastic work at fatigue crack tips. This was first begun by [Weertman, 1973] and elaborated later by [Mura and Lin, 1974] and [Antolovich et al., 1975] who considered the following formulation:

$$\frac{da}{dN} = \eta \frac{\Delta K^4}{\mu p^2 \gamma_F}, \tag{1.13}$$

where η is a proportional constant, μ is the shear modulus, p is a strength parameter, and γ_F is the plastic work absorbed in advancing the crack a unit area. Equation (1.13) shows that for materials with high plastic work at the crack tip, the fatigue crack growth rate decreases, and that decelerates the crack propagation process.

In the same vein, [Pippan and Stüwe, 1992] studied the effect of the applied SIF range on the cyclic plastic work spent at the fatigue crack tip. For this purpose, they defined the specific plastic work necessary to create a unit of fracture surface as:

$$\gamma_F = \frac{\delta W}{2Bda/dN}, \tag{1.14}$$

where δW is the plastic work spent at the crack tip during one fatigue cycle, and B is the length of the advancing crack front. To quantify γ_F, Pippan and Stüwe first showed that δW is mostly dissipated into heat, δQ, by computing δW with a mechanical approach and experimentally estimating δQ by thermal measurements. The values of δW and δQ were plotted against different applied SIF ranges ΔK, as shown in Figure 1.11, where the circles denote computed mechanical quantities of δW, and the triangles and crosses correspond to experimental thermal estimations of

δQ. It can be seen that they both lie on the same straight line, hence the assumption: $\delta W \approx \delta Q$.

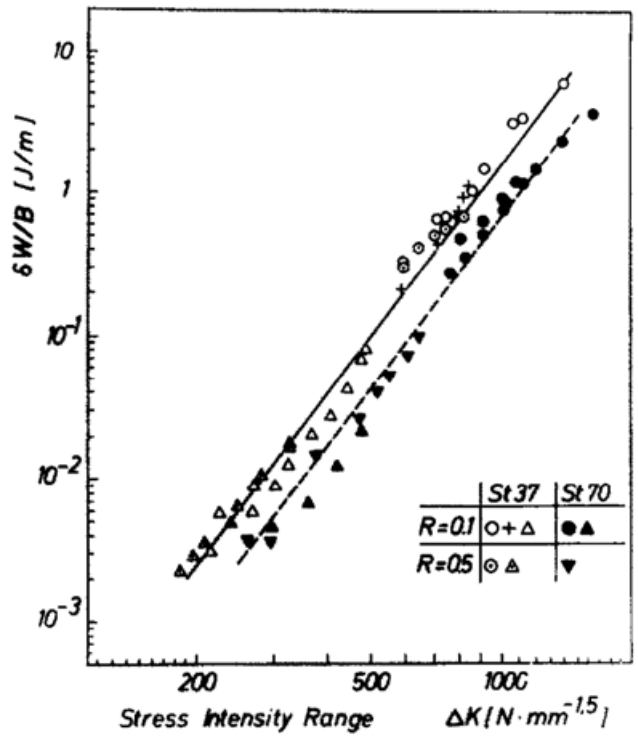

Figure 1.11: Cyclic plastic work spent at the crack tip versus the SIF range (for two structural steels) at a loading frequency $f = 250Hz$, [Pippan and Stüwe, 1983].

Afterward, Pippan and Stüwe measured the fatigue crack growth rate, $\frac{da}{dN}$, so that they could quantify the specific plastic work, γ_F, by using Equation (1.14). This enabled to plot γ_F against ΔK as shown in Figure 1.12 below. In this figure, the steep rise of the curves towards low values of ΔK is because the values of the fatigue crack growth rate drop to virtually zero at low ΔK, thus according to Equation (1.14) the value of γ_F is singular at low ΔK. For intermediate ΔK, γ_F is roughly constant. For high values of ΔK, γ_F dips down to low values because the fatigue crack growth rate increases much faster at this stage of crack growth. Moreover, from Figure 1.12, for the same material and applied ΔK, it can be read that the specific plastic work at the crack tip decreases when the applied R-ratio increases. This remained open for further research as it depends on the material.

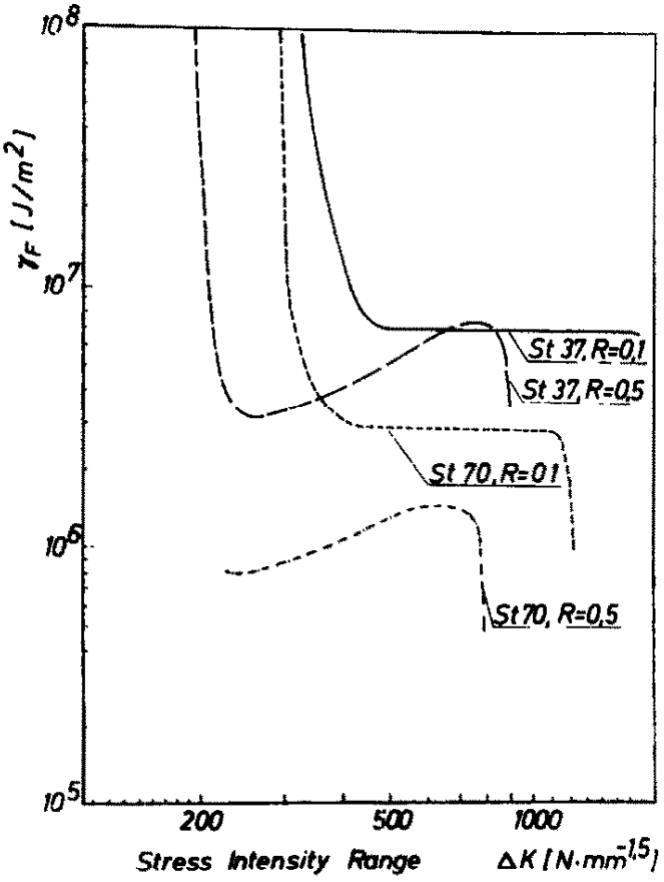

Figure 1.12: Specific plastic work spent to create a unit of fracture surface, [Pippan and Stüwe, 1992].

1.2.4 Heat production mechanisms during fatigue crack propagation

Following the work of Pippan and Stüve, [Flores and Dauskardt, 1999] characterized, from a thermodynamics standpoint, the dissipation of the plastic work as heat generated at the tip of a propagating fatigue crack in a bulk metallic glass. They observed a near tip temperature increase which was found to be consistent with predictions of the dissipation of plastic work as heat. They also observed a locally cooled zone ahead of the crack tip which was consistent with thermoelastic effects.

In fact, many experimental and theoretical works have been done between 1970s and 1990s in order to study the characteristics related to thermal effects induced by the dissipation of plasticity into heat near the tip of cracks. In the area of ex-

perimental studies under **monotonic loading**, [Döll, 1973] was one of the earlier investigators who estimated the overall heat output at the tip of a dynamic propagating crack. From thermocouple measurements on four different polymer specimens, he found that the heat output due to plastic work increases with the crack speed. [Fuller and Fox, 1975] performed similar tests with liquid crystal films and infrared detectors, as well as thermocouples. They estimated that the peak temperature rise near a crack that was growing at a speed in the range of $200 - 650 m.s^{-l}$ was about $500K$. A more surprising result was reported by [Weichert and Schönert, 1978] who measured, with a very sensitive radiation thermometer, temperatures between 2500 and $3000K$ for cracks propagating in glass and about $4700K$ for cracks growing in quartz at very high crack velocities. [Bryant et al., 1986] conducted tests on two titanium alloys. They examined the fracture surface of test specimens using scanning electron microscopy and found out that the melting point of the titanium alloys could be exceeded at the tip of a rapidly moving crack.

Much attention has later been devoted to the search for understanding the mechanism of plastic dissipation in heat at the crack tip under **cyclic loading** ([Ranc et al., 2008]). However, no impact of the associated thermal effect on fracture, in terms of the SIF, was established until [Ranc et al., 2011] proposed a thermomechanical analysis, based on the LEFM, highlighting the consequences on the SIF of the cyclic plasticity dissipated into heat at the tip of a fatigue crack. They addressed the issue because the SIF may be modified because of the cyclic plastic dissipation in heat occurring in the RCPZ, especially since this thermal effect may increase with the loading frequency. They therefore established a direct analytic linear relationship between the cyclic plastic dissipation in heat in the RCPZ and the SIF in an infinite plate with a semi-infinite through crack under mode I cyclic loading. Afterward, [Ranc et al., 2014] studied the problem for a finite CCT specimen made of C40-steel, where they first proposed an experimental method, based on infrared measurements during fatigue crack growth tests, to quantify the heat produced by cyclic plasticity in the RCPZ, and then they computed by FEA the associated effect on the SIF, K_I, under different applied SIF ranges, ΔK_I, and for a fixed applied load ratio, $R = 0.1$. Indeed, under the superposition principle of the LEFM, they showed that a thermal correction of the SIF, denoted by K_{temp}, must be assessed and added to the SIF associated with the applied mechanical loading, $K_I(t)$. They therefore calculated K_{temp} from the estimated cyclic plastic dissipation in the RCPZ of a long propagating fatigue crack, by computing the associated heterogeneous temperature field, and solving the thermomechanical crack-tip stress field enabling to calculate K_{temp} under the hypothesis of plane stress.

Table 1.2 gives the estimation of the cyclic plastic dissipation in heat in the RCPZ, denoted by q, obtained with frequencies of cyclic loading about $100Hz$. It is interpreted as a dissipated power per unit length of the crack front. The calculation of the thermal correction K_{temp} is presented as well.

R	$\Delta K(MPa.\sqrt{m})$	$q(W.m^{-1})$	$K_{temp}(MPa.\sqrt{m})$
0.1	12	17.7	-0.04
0.1	15	62.2	-0.14
0.1	17	84.1	-0.18
0.1	20	153	-0.32

Table 1.2: Results of the estimation of the cyclic plastic dissipation in heat in the RCPZ and the associated thermal corrections of the SIF, on C40 steel. ([Ranc et al., 2014])

From the results of Table 1.2, the thermal correction of the SIF is negative because it describes the compressive state of the stress field around the crack tip, which is due to thermal expansion of the material ahead of the crack tip. As a result, K_{temp} modifies the local load ratio near the crack tip, $R = \frac{K_{min}}{K_{max}}$, since it decreases the minimum and maximum values of the SIF. However, the absolute values of these thermal corrections are small compared to the values of the SIF range.

Therefore, it is interesting to study the effect of additional applied fatigue loading in terms of ΔK_I and R-ratio to see how much this impacts the order of magnitude of the thermal correction K_{temp} resulting from the effect of the cyclic plastic dissipation in heat in the RCPZ.

1.3 Conclusion of Chapter I

This PhD work comes then, not only to complete the study of [Ranc et al., 2014], but also to explore the consequences, on the SIF, of other thermal effects which can develop in fatigue of metallic alloys. It should be noted that many stakes are associated with this problem, especially: (i) quantifying the thermal effects that are likely to be generated under cyclic loading of a finite specimen with a long propagating fatigue crack. This requires a thermodynamic characterization, as well as a specific methodology of assessment which can be either experimental or numerical. More about this item is discussed in Chapter II. (ii) Modeling and solving the thermomechanical problem leading to study the consequences of the thermal

effects on the SIF. This actually needs to define a specific calculation framework with relevant methodology and hypothesis in order to simplify the problem since it deals with non-linearities as well as coupled thermal and mechanical effects.

Chapter 2

Characterization and assessment of the heat sources and their resulting temperature fields

Contents

Le deuxième chapitre de ce mémoire a pour objectifs de quantifier les sources de chaleur présentes pendant la sollicitation mécanique cyclique d'une éprouvette fissurée, et de calculer les champs de température générés par chaque source.

Dans un premier temps, les concepts de la thermodynamique sont rappelés afin d'expliquer l'origine et la nature de chaque source de chaleur. Les sources en question sont la source de couplage thermoélastique, la source de dissipation intrinsèque liée à la microplasticité, et la source de dissipation plastique en chaleur liée à la plasticité cyclique qui se produit en pointe de fissure. Dans un second temps, ces sources de chaleur sont séparément quantifiées suivant des méthodes particulières à chaque source. La source thermoélastique est numériquement calculée par la méthode des éléments finis, et ce après un développement mathématique des équations classiques de la thermoélasticité linéaire. La source de dissipation intrinsèque liée à la microplasticité est quantifiée selon une approche expérimentale basée sur les essais d'auto-échauffement en fatigue. La source de dissipation plastique cyclique en pointe de fissure est aussi quantifiée selon une approche expérimentale basée sur les essais de propagation d'une fissure de fatigue. Enfin, le champ de température associé à chaque source est calculé par éléments finis en résolvant le problème linéaire de l'équation de la chaleur. Il faut souligner que ce calcul thermique constitue la première étape menant à la résolution du problème de cette thèse.

The second chapter aims at quantifying the heat sources generated during cyclic loading of a cracked specimen as well as computing their resulting temperature fields. First, the fundamental theoretical knowledge of thermodynamics is presented to explain the origins and the nature of the heat sources. The heat sources in question are the thermoelastic coupling source, the intrinsic dissipation due to microplasticity, and the cyclic plasticity dissipated into heat in the reverse cyclic plastic zone ahead of the crack tip. Secondly, the heat sources are separately quantified. Each heat source has its specific quantification method. The thermoelastic source is numerically computed by finite element analysis after a mathematical development of classical equations of linear thermoelasticity. The intrinsic dissipation due to microplasticity is quantified with an experimental approach using self-heating fatigue tests. The cyclic plasticity dissipated into heat in the reverse cyclic plastic zone is also experimentally quantified by using infrared measurements at the crack tip.

Having determined the three heat sources, the associated temperature fields are computed by solving the linear heat diffusion equation problem. This is carried out by finite element analysis. It should be noted that solving the thermal problem is the key point to solve this thesis problem which is discussed later in the next chapter.

2.1 Theoretical concepts behind the heat sources

Characterizing the heat sources generated during mechanical cyclic loading of a cracked specimen requires the use of a thermodynamic approach in order to understand their origins and the relationship between mechanical and thermal effects.

Initially, thermodynamics was developed for fluids in the 19^{th} century, and more recently it was extended to solids. Such an approach has already been used in the literature, for instance in [Thomson, 1857], [Germain et al., 1983], and [Rosakis et al., 2000].

The interest of quantifying the heat sources lies in the fact that they are related to the thermomechanical behavior of the material. For instance, elastic or plastic behaviors do not lead to produce the same heat sources.

Before quantifying the heat sources involved in this problem, their origins are presented by using the concepts of thermodynamics.

2.1.1 Fundamental concepts of thermodynamics

In thermodynamics, the state of a volume of a solid system is described by a given number of variables, named state variables, such as temperature and strain. These state variables enable to define the internal energy of the material, e, or the free energy, ψ, which is more used in materials science. The free energy is defined as the Legendre transform of the internal energy according to temperature and entropy variables, T and s, respectively. This is given by Equation (2.1).

$$\psi = e - Ts. \tag{2.1}$$

The use of the free energy concept for describing the thermodynamic state of materials is more convenient than the use of the internal energy since the free energy is easily expressed by the use of measurable quantities such as temperature and strain, while the internal energy uses the entropy and strain. Therefore, in order to describe the thermomechanical behavior of a material, it is necessary to express its free energy with respect to state variables.

When the material undergoes a thermodynamic transformation (evolution of its state variables), the free energy changes, and the final transformation state can be determined by using the first law of thermodynamics. This law postulates that the internal energy is equal to the transferred energy like, work and heat, during the transformation. However, it does not give information about the transformation

direction. That is why, it is necessary to introduce the second law of thermodynamics which allows to describe the irreversibilities taking place during the transformation. This is characterized by Clausius-Duhem inequality:

$$\rho T \dot{s}_i = d_{tot} = \underbrace{\sigma\dot{\varepsilon} - \rho\dot{\psi} - \rho s\dot{T}}_{d_1} \underbrace{-\frac{1}{T}\vec{q}.\overrightarrow{\text{grad}T}}_{d_2} \geq 0, \tag{2.2}$$

where $\dot{\square}$ denotes $\frac{\partial \square}{\partial t}$ with t is time, ρ is the material density, s_i is the entropy associated with irreversibilities, and $\vec{q}$ is the heat flux vector.

Since it is more convenient to describe the irreversibilities by an energy, the total dissipation, d_{tot}, is defined. According to the second law of thermodynamics, $\dot{s}_i \geq 0$, thus, $d_{tot} \geq 0$. Moreover, the total dissipation, d_{tot}, can be decomposed into two parts, d_1, the intrinsic dissipation, and d_2, the thermal dissipation. These two dissipative quantities are independent, and thus, positive or null. When the transformation of the material is reversible, $\dot{s}_i = 0$, and then, $d_{tot} = 0$.

The thermal dissipation, d_2, is the part of dissipation which is associated with thermal losses, by conduction for example. While the intrinsic dissipation, d_1, is related to the thermomechanical behavior of the material, in other words, characterizing the dissipation of a material can be done through defining its intrinsic dissipation, d_1.

Rearranging the first law of thermodynamics (conservation of energy), the free energy, and the total dissipation, lead to write the heat diffusion equation. By considering the classical conduction law of Fourier ($\vec{q} = -k\overrightarrow{\text{grad}T}$, where k is the thermal conductivity coefficient of the material), the volume heat diffusion equation can be written as follows:

$$\rho c\dot{T} = s_{coupling} + d_1 + k\Delta T, \tag{2.3}$$

where c is the specific heat capacity, and $s_{coupling}$ is the power of the thermomechanical coupling due to the dependence of the mechanical part of the free energy with the temperature. This thermochanical coupling power is more important when the material mechanical behavior is sensitive to temperature variation. Moreover, by considering a material with an elastic-plastic behavior for example, $s_{coupling}$ can be written as the sum of a thermoelastic coupling term, s_{the}, associated with the dependence of the mechanical behavior with the temperature, and a thermoplastic coupling term, s_{plas}, associated with the dependence of the material hardening with the temperature, that being: $s_{coupling} = s_{the} + s_{plas}$.

Within the framework of the study carried out in this work, the temperature

of the material does not reach levels at which material hardening can be impacted by the temperature change. *Thus, in this study it is assumed that the temperature has negligible effects on material hardening, and the thermoplastic coupling is then not taken into account.* In Equation (2.3), the thermomechanical coupling power, $s_{coupling}$, can therefore be replaced by the thermoelastic coupling power, s_{the} (called "thermoelastic source" in the following of this thesis), which gives the volume heat diffusion equation:

$$\rho c\dot{T} = s_{the} + d_1 + k\Delta T. \tag{2.4}$$

As mentioned above, the intrinsic dissipation, d_1, is always a positive heat source, while the thermoelastic source, s_{the}, can be either positive or negative depending on the cyclic loading (loading-unloading). Moreover, the thermoelastic source is proportional to the trace of the stress tensor (hydrostatic stress), as well as the loading frequency. This dependence is more detailed afterward in Section §2.4.1.

For a plastic behavior, an intrinsic dissipation can always be generated during the loading of a material. It is generally expressed as the product of the material yield stress, σ_y, and the equivalent plastic strain rate, $\dot{\varepsilon}^p_{eq}$, as given by Equation (2.5).

$$d_1 = \sigma_y.\dot{\varepsilon}^p_{eq}. \tag{2.5}$$

Furthermore, under a cyclic loading for example with an applied stress amplitude lower than the cyclic yield stress of the material, the intrinsic dissipation can also take place. This was experimentally verified in [Boulanger et al., 2004] for instance, as shown in Figure 2.1 on a dual phase steel (DP60). The physical origin of this phenomenon is related to the plasticity at the scale of the microstructure. This is called "microplasticity" in the following.

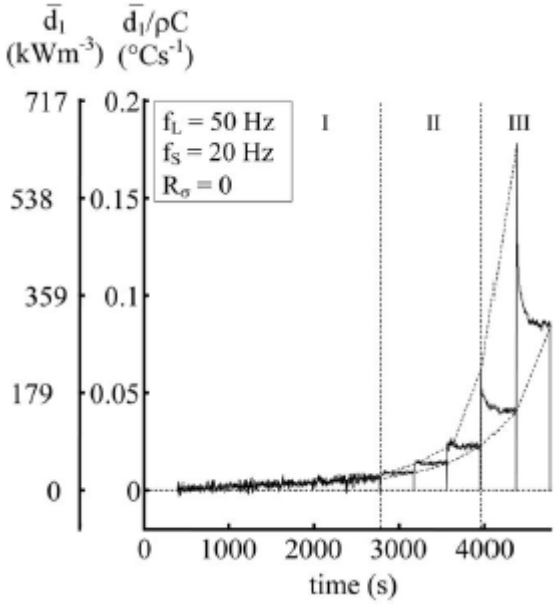

Figure 2.1: Evolution of d_1 over time for several applied load block series, [Boulanger et al., 2004].

From the thermodynamic approach, it is therefore possible to describe the behavior of a loaded material by defining two types of heat sources. The first one is the thermoelastic source which is related to the thermoelastic coupling. The second one is the intrinsic dissipation related to plasticity and microplasticity.

2.1.2 Application of the thermodynamic approach in the presence of a long propagating fatigue crack

The description of thermomechanical processes for a material affected by a long propagating fatigue crack and cyclically loaded, can be done within the thermodynamic approach introduced in the previous section. In other words, the thermoelastic and dissipative heat sources are also present in this situation. But, it is known that the presence of a fatigue crack implies the generation of a heterogeneous stress field around the crack tip, as well as a reverse cyclic plastic zone (RCPZ) ahead of the crack tip (*cf.* Chapter I). This means that, inside this zone, cyclic plastic strains occur and produce an intrinsic dissipation related to plasticity at the macroscopic scale. Moreover, since the size of the RCPZ is small compared to the crack ligament under the small scale yielding condition, the heat produced inside this zone can be expressed as a cyclic plastic power per unit length. In the following, this power per

unit length, which is positive, is denoted by, q. Additionally, outside the RCPZ, the stress in the material is below the cyclic yield stress, which generates microplastic strains leading to an intrinsic dissipation at the grain scale. This is called "the intrinsic dissipation due to microplasticity", denoted by d_1 in the following.

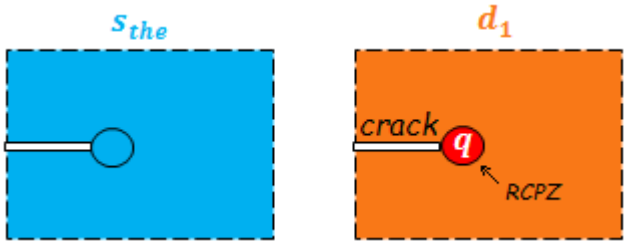

Figure 2.2: Drawing of the distribution of the three types of heat sources considered in this work.

Figure 2.2 illustrates that when a material contains a long propagating fatigue crack and is subjected to a cyclic loading, three heat sources are present: the thermoelastic source, s_{the}, the intrinsic dissipation due to microplasticity, d_1, and the cyclic plasticity dissipated into heat in the RCPZ, q. It should be mentioned that the shape of the RCPZ is represented, for simplification, by a disc ahead of the crack tip as done in the literature when the RCPZ is small compared to the crack ligament.

Furthermore, the dissipative heat sources, d_1 and q, can be separated as illustrated in Figure 2.3. This helps in solving the associated linear thermal problem in Section §2.4.

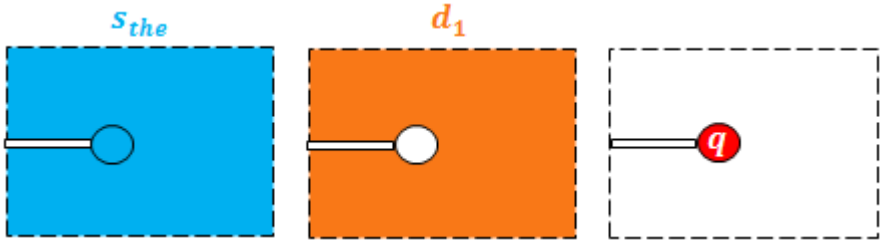

Figure 2.3: Separating the dissipative heat sources d_1 and q.

Then, the linear heat diffusion equation (Equation (2.4)) can be rewritten as follows:

$$\rho c\dot{T} - k\Delta T = s_{the} + d_1 + q_{vol}\delta(M), \tag{2.6}$$

where $q = q_{vol}A_{RCPZ}$, q_{vol} is the volume cyclic plastic power dissipated into heat

in the RCPZ, A_{RCPZ} is the area of the RCPZ, $\delta(M)$ is the Dirac function such that $\delta(M \in A_{RCPZ}) = 1$ and $\delta(M \notin A_{RCPZ}) = 0$. Thermal boundary conditions must be added to the heat diffusion equation in order to fully define the linear thermal problem leading to solve the temperature fields, T_{the}, T_d, and T_q, respectively associated with the heat sources, s_{the}, d_1, and q, such that $T = T_{the} + T_d + T_q$. This is discussed afterward in Section §2.4.

It must be pointed out that the heat diffusion equation (Equation (2.6)) describes a volume thermal problem and does not take into account the heat which may result from frictional contact of crack faces. *This heat is actually considered negligible in the crack mode I loading which is of interest in this work.*

In the next section, the methodology used for quantifying the three types of heat sources characterized above is presented.

2.2 Methodology for quantifying the heat sources

Since the goal is to quantify the three types of heat sources generated during fatigue tests with a cracked specimen, it is important to first explain the methods considered to achieve this goal. It should be noted that each heat source has its specific estimation method.

As mentioned in the previous section, the thermoelastic source, s_{the}, is proportional to the trace of the stress tensor. In other words, by knowing the stress tensor in the cracked specimen, the thermoelastic source can be defined. Therefore, a FEA is carried out in order to compute the fields of the components of the stress tensor in the cracked specimen by considering a linear-elastic and isotropic material behavior. Afterward, based on the relationship between the thermoelastic source and the trace of the stress tensor, detailed in Section §2.4.1, the thermoelastic source is then numerically computed in the cracked material.

For the intrinsic dissipation, d_1, it directly depends on the amplitude of the stress field occurring in the cracked material, for this reason, experimental 'self-heating' fatigue tests, introduced by [Luong, 1995], are carried out. They enable to link the intrinsic dissipation to the normal stress amplitude applied to a smooth uncracked specimen. Indeed, during self-heating fatigue tests, a normal stress amplitude is applied at the top of a smooth uncracked specimen and is homogeneously distributed in its remainder, and while the fatigue test goes on, the temperature of the specimen increases because of the effect of intrinsic dissipation. Therefore, infrared measurements are used to measure this temperature variation, which then leads to estimate the intrinsic dissipation associated with the applied stress amplitude. The resulting

curve showing the dependence of the intrinsic dissipation with the applied stress amplitude is called "self-heating curve". Establishing the self-heating curve with smooth uncracked specimens enables later to approximate the intrinsic dissipation occurring in the cracked specimen, outside the RCPZ. Indeed, by considering a normal stress amplitude applied to the cracked specimen, the field of the amplitude of the Von-Mises equivalent stress is computed in the cracked material by using FEA assuming a linear-elastic and isotropic behavior. Then, by assuming the hypothesis of quasi-static processes and small perturbations, the field of the intrinsic dissipation is deduced in the cracked specimen outside the RCPZ by using the self-heating curve. This method is detailed afterward in Section §2.4.2.

For the cyclic plasticity dissipated into heat in the RCPZ, q, a direct experimental method is used to estimate this heat source. It consists in measuring the increase of temperature occurring at the crack tip during fatigue crack growth tests, and then estimating the associated heat source, q, by using a specific method based on the linearity of the heat diffusion equation. More about this method is explained in Section §2.4.3.

It should be noted that after estimating the heat sources, the temperature field generated by each heat source, is numerically computed, by FEA, by using the linearity of the heat diffusion equation (Equation (2.6)). This step could have been directly done by infrared measurements, but a sub-sampling factor (1/5) associated with the frequency acquisition ($25Hz$) of the infrared camera used in this investigation, was used for optimizing the recording of infrared measurements during fatigue tests conducted at loading frequencies, $f \approx 100Hz$. This is not high enough to measure the thermoelastic effect. Moreover, the optical resolution of the infrared camera is not accurate enough to precisely measure the distribution of the temperature field inside the RCPZ, so this temperature field is computed after quantifying its associated heat source, q, occurring in the RCPZ.

Before presenting the estimations of the heat sources and the computation of the associated temperature fields, the material and the geometry of the cracked specimens used in this work are presented in the next section.

2.3 Material and geometry of the specimens

The cracked specimens used in this work are center-cracked tensile (CCT) plates, made of C40 steel which is a medium carbon steel with the physical properties given in Tables 2.1 and 2.2.

$E(GPa)$	ν	$\sigma_y(MPa)$	$\sigma_y^{cyc.}(MPa)$	$R_m(MPa)$	$A(\%)$	$\rho(kg.m^{-3})$
210	0.3	340	200	600	16	7568

Table 2.1: Mechanical properties of C40 steel.

where E is the Young's modulus, ν is the Poisson's ratio, σ_y is the yield stress under quasi-static monotonic loading, $\sigma_y^{cyc.}$ is the cyclic yield stress, R_m is the ultimate tensile strength, A is the material elongation after fracture, and ρ is the material density.

$\alpha(K^{-1})$	$k(W.K^{-1}.m^{-1})$	$c(J.K^{-1}.kg^{-1})$
1.2×10^{-5}	52	460

Table 2.2: Thermal properties of C40 steel.

where α is the thermal expansion coefficient, k is the thermal conductivity coefficient, and c is the specific heat capacity.

The CCT specimens are designed with a rectangular thin-flat geometry according to fatigue test execution requirements of the ASTM Standard E647, [ASTM-E647, 2013]. The geometry is given in Figure 2.4. The specimens were cut in a way that the central notch, machined by electro-erosion, is perpendicular to the rolling direction.

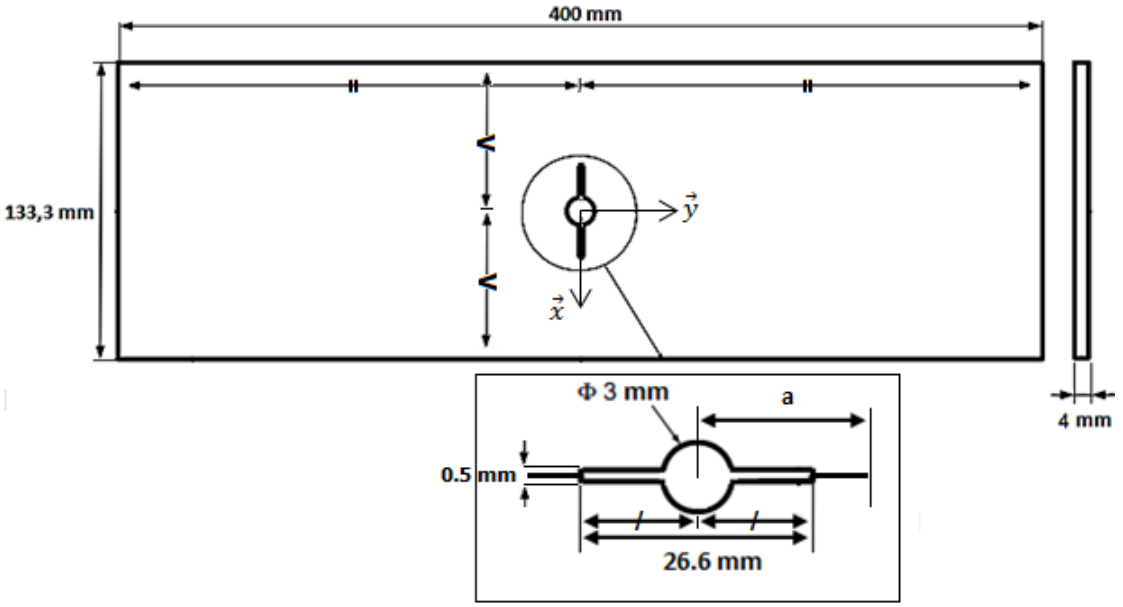

Figure 2.4: Geometry of the CCT plate.

It is important to note that this geometry is originally used for estimating the cyclic plastic dissipation into heat in the RCPZ, q, by carrying out fatigue crack

growth tests. But, in order to be able to compare the thermal effects generated by the three types of heat sources and their resulting consequences on the SIF, the same geometry is considered in the calculation of the thermoelastic source, s_{the}, and the estimation of the intrinsic dissipation due to microplasticity, d_1.

2.4 Quantification of the heat sources and computation of the associated temperature fields

2.4.1 The thermoelastic source

As mentioned in Section §2.2, the thermoelastic source is numerically computed from the trace of the stress tensor calculated in the cracked material. Before developing the calculation enabling to establish the relationship between the thermoelastic source and the trace of the stress tensor, an emphasis is hereinafter made on the assumptions defining the calculation framework.

The thickness of the CCT specimen (Figure 2.4) is very small compared to its length and width. Moreover, during fatigue tests, since the CCT specimen respects ASTM standard requirements, it is reasonable to assume that the load is uniformly applied at its upper boundary by forces acting parallel to its plane and uniformly distributed through the thickness. Having considered these conditions, the hypothesis of plane stresses is adopted in order to simplify the problem and reduce the calculation time.

Furthermore, due to the symmetries of the CCT specimen geometry (Figure 2.4), a two-dimensional model of one-fourth of the specimen is considered. The geometry of this quarter model is presented in Figure 2.5.

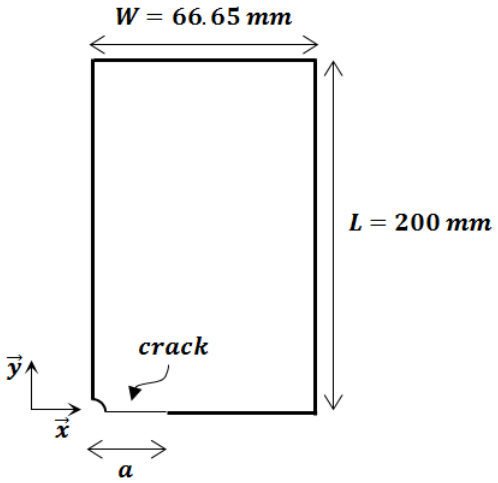

Figure 2.5: Geometry of the quarter model of the CCT plate.

As said before, the thermoelastic source contribution to thermal effects accounts for the power of the thermoelastic coupling. It is defined by the following equation:

$$s_{the}(x,y,t) = T(x,y,t).\frac{\partial \bar{\bar{\sigma}}(x,y,t)}{\partial T} : \dot{\bar{\bar{\varepsilon}}}(x,y,t), \tag{2.7}$$

where $\bar{\bar{\sigma}}$ is the second order stress tensor, and $\bar{\bar{\varepsilon}}$ is the second order strain tensor.

The development of this equation is based on the introduction of the two-dimensional constitutive equation of thermoelasticity written by assuming linear responses and isotropy in both the deformation and dilatation phenomena of the material:

$$\bar{\bar{\sigma}}(x,y,t) = \bar{\bar{\bar{\bar{C}}}} : \left[\bar{\bar{\varepsilon}}(x,y,t) - \alpha.(T(x,y,t) - T_0).\bar{\bar{1}}\right], \tag{2.8}$$

where $\bar{\bar{\bar{\bar{C}}}}$ is the fourth order stiffness tensor, α is the thermal coefficient, T_0 is the reference temperature, and $\bar{\bar{1}}$ is the second order identity tensor.

The derivative of the stress with respect to the temperature gives :

$$\frac{\partial \bar{\bar{\sigma}}(x,y,t)}{\partial T} = -\alpha.\bar{\bar{\bar{\bar{C}}}} : \bar{\bar{1}}. \tag{2.9}$$

To simplify the development of Equation (2.7), it is assumed that the temperature variation, $T - T_0$, is small with respect to T_0 (*i.e.* $T \approx T_0$). This leads to write the strain tensor rate as follows:

$$\bar{\bar{\sigma}}(x,y,t) = \bar{\bar{\bar{\bar{C}}}} : \bar{\bar{\varepsilon}}(x,y,t), \tag{2.10}$$

$$\Rightarrow \dot{\bar{\bar{\varepsilon}}}(x,y,t) = \bar{\bar{\bar{\bar{C}}}}^{-1} : \dot{\bar{\bar{\sigma}}}(x,y,t). \tag{2.11}$$

As a result, the thermoelastic source becomes:

$$s_{the}(x,y,t) = -\alpha.T_0.\bar{\bar{\bar{\bar{C}}}} : \bar{\bar{1}} : \bar{\bar{\bar{\bar{C}}}}^{-1} : \dot{\bar{\bar{\sigma}}}(x,y,t), \tag{2.12}$$

which can finally be written as:

$$s_{the}(x,y,t) = -\alpha.T_0.\frac{\partial \bar{\bar{1}} : \bar{\bar{\sigma}}(x,y,t)}{\partial t} = -\alpha.T_0.\mathrm{tr}(\dot{\bar{\bar{\sigma}}}(x,y,t)), \tag{2.13}$$

with $\mathrm{tr}(\dot{\bar{\bar{\sigma}}})$ is the time derivative of the stress tensor trace resulting from the mechanical response in the material.

During fatigue tests, the load applied at the top of the CCT plate is sinusoidal. Therefore, the stress response in the CCT plate is also sinusoidal and can be expressed as: $\bar{\bar{\sigma}}(x,y,t) = \bar{\bar{\sigma}}_a(x,y).\sin(2\pi ft) + \bar{\bar{\sigma}}_m(x,y)$ where $\bar{\bar{\sigma}}_a$ is the resulting stress tensor amplitude, and $\bar{\bar{\sigma}}_m(x,y)$ is the resulting mean stress tensor. Equation (2.13) can then be developed as:

$$\begin{aligned} s_{the}(x,y,t) &= -\alpha.T_0.\mathrm{tr}(\dot{\bar{\bar{\sigma}}}(x,y,t)) && (2.14)\\ &= -2\pi.f.\alpha.T_0.\mathrm{tr}(\bar{\bar{\sigma}}_a(x,y)).\cos(2\pi ft) && (2.15)\\ \Rightarrow s_{the}(x,y,t) &= 2\pi.f.\alpha.T_0.\mathrm{tr}(\bar{\bar{\sigma}}_a(x,y)).\sin(2\pi ft - \frac{\pi}{2}). && (2.16) \end{aligned}$$

The transition from Equation (2.14) to Equation (2.15) is done by the derivation over time of the stress tensor response. It can therefore be seen that the mean stress disappears after this time-derivation since the applied mean stress is constant over time. As a consequence, it is important to note that a constant applied mean stress has no effect on the thermoelastic source.

In a more generic format, Equation (2.16) of the thermoelastic source can finally be written as:

$$s_{the}(x,y,t) = s^a_{the}(x,y).\sin(2\pi ft - \frac{\pi}{2}), \tag{2.17}$$

with:

$$s^a_{the}(x,y) = 2\pi f.\alpha.T_0.\mathrm{tr}(\bar{\bar{\sigma}}_a(x,y)). \tag{2.18}$$

Thus, by computing the trace of the stress amplitude response, $\mathrm{tr}(\bar{\bar{\sigma}}_a)$, due to the mechanical loading applied to the CCT plate, the field of the thermoelastic source amplitude, s^a_{the}, can be computed. FEA is used for this purpose.

An example of loading conditions is considered here in order to highlight the

numerical calculations. It concerns the conditions of a real loading applied during fatigue crack growth tests which allowed to estimate the heat source q, namely: a crack length $a = 31.3mm$, a loading frequency $f = 98.6Hz$, an applied SIF range $\Delta K_I = 26MPa.\sqrt{m}$, which is equivalent to an applied normal stress amplitude $\frac{\Delta\sigma}{2} = 44.6MPa$ according to Equation 1.4, and a reference temperature $T_0 = 20°C$.

Figure 2.6 illustrates the applied loading and the boundary conditions of symmetries considered in the FEA.

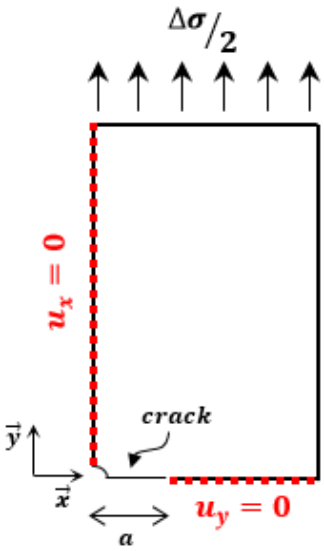

Figure 2.6: Schematic sketch showing the boundary conditions of symmetries and the load applied to the quarter model of the CCT specimen.

It should be noted that the FEA is done within the scope of the linear elasticity by considering a homogeneous isotropic material behavior as well as a stationary crack.

Figure 2.7 depicts the calculation of the trace of the stress tensor amplitude, $\mathrm{tr}(\bar{\bar{\sigma}}_a)$, computed in the quarter model of the CCT specimen. On the left of this figure, a zoom near the crack tip shows the field map of $\mathrm{tr}(\bar{\bar{\sigma}}_a)$. On the right, the evolution of $\mathrm{tr}(\bar{\bar{\sigma}}_a)$ along the cracked axis (x axis of Figure 2.6) is plotted.

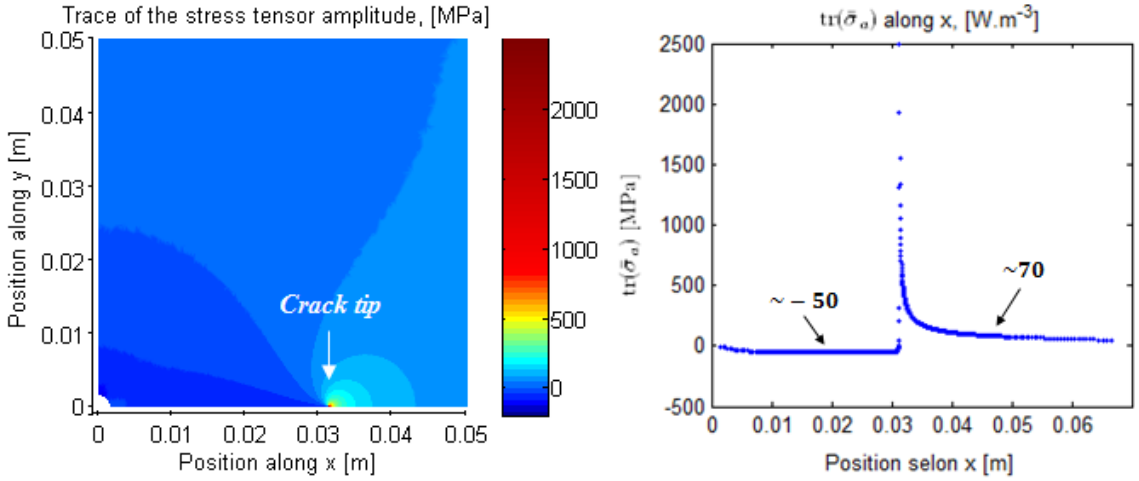

Figure 2.7: Trace field of the stress tensor amplitude, $\mathrm{tr}(\bar{\bar{\sigma}}_a)$, computed with the loading configuration: $a = 31.3mm$, and $\Delta K_I = 26MPa.\sqrt{m}$.

Therefore, from the trace of the stress tensor amplitude, $\mathrm{tr}(\bar{\bar{\sigma}}_a)$, the amplitude of the thermoelastic source, s^a_{the}, is computed according to Equation (2.18). Figure 2.8 illustrates the field map of the thermoelastic source amplitude as well as its evolution along x axis.

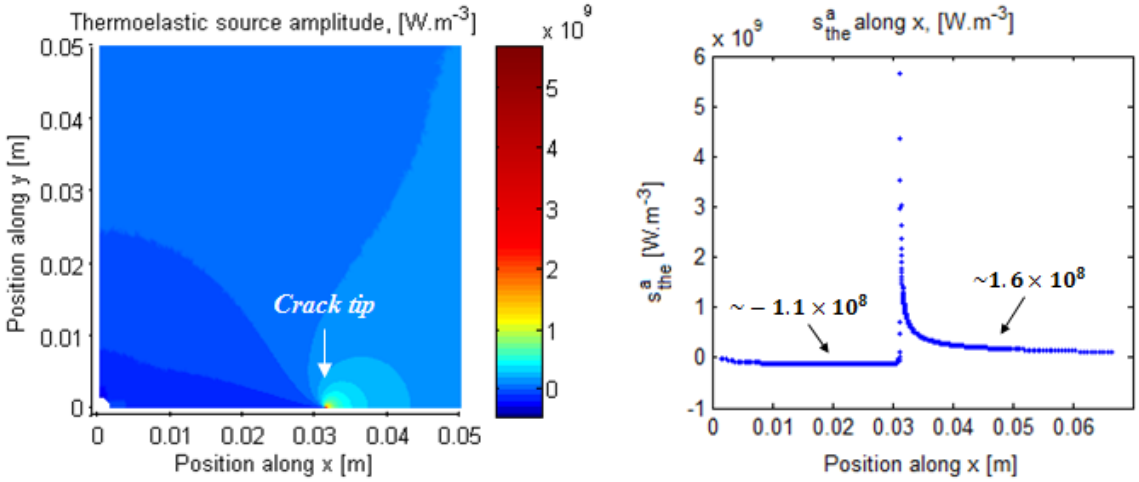

Figure 2.8: Field of the thermoelastic source amplitude, s^a_{the}, computed with the loading configuration: $a = 31.3mm$, $f = 98.6Hz$, $\Delta K_I = 26MPa.\sqrt{m}$, and $T_0 = 20°C$.

As it can be observed in Figure 2.8, the thermoelastic source amplitude, s^a_{the}, is strongly heterogeneous, and reaches a peak at the crack tip. This originates from the singularity of the trace of the stress tensor amplitude response occurring in the

same region (Figure 2.7) since the crack-stress fields are singular at the crack tip in linear-elasticity.

Thus, the thermoelastic source is fully defined. It should be noted that it has a phase shift of $\frac{\pi}{2}$ with respect to the mechanical response in the material (Equation (2.17)).

Now, in order to compute the resulting thermoelastic temperature field, a thermal problem needs to be defined. First, it is assumed that the computed two-dimensional thermoelastic source is representative of what happens throughout the CCT specimen thickness since it results from the stress tensor which is calculated under the assumption of plane stresses. In addition, the resulting thermoelastic temperature field is also supposed to be homogeneous over the thickness. This last assumption can be verified by calculating the Biot number which has to be small compared with unity. Indeed, the Biot number is defined by $B_i = \frac{h.l_c}{k}$, where h is the convection coefficient, l_c is a characteristic length taken equal to the CCT specimen thickness, and k is the material thermal conductivity. By considering the following values: $h = 10W.m^{-2}.K^{-1}$ (typical value for natural convection in air), $l_c = 4mm$ and $k = 52W.m^{-1}.K^{-1}$, the Biot number is then $B_i = 7.7 \times 10^{-4} << 1$. It can therefore be considered that the temperature is homogeneous over the plate thickness.

Having considered these assumptions, the thermal problem enabling to calculate the thermoelastic temperature can be modeled by the following two-dimensional heat diffusion problem:

$$\begin{cases} \rho.c.\dot{\theta}_{the} - k.(\frac{\partial^2\theta_{the}}{\partial x^2} + \frac{\partial^2\theta_{the}}{\partial y^2}) + 2\frac{h}{e}.\theta_{the} & = s_{the}(x,y,t), \\ \theta_{the}(x,y,t=0) & = 0 \\ k.\frac{\partial\theta_{the}}{\partial x}|_{x=\pm W} & = h.\theta_{the}(x=\pm W,y,t) \\ k.\frac{\partial\theta_{the}}{\partial y}|_{y=\pm L} & = h.\theta_{the}(x,y=\pm L,t) \end{cases} \tag{2.19}$$

where $\theta_{the} = T_{the} - T_0$ is the thermoelastic temperature variation, T_0 is the initial condition supposed to be homogeneous in the specimen and taken equal to the surrounding temperature ($T_0 = 20°C$). The left-hand term is obtained by averaging, over the CCT plate thickness, the temperature in the left-hand term of the volume heat diffusion equation (Equation (2.4)). The resulting term, $2\frac{h}{e}.\theta_{the}$, represents the heat exchange by convection with air which occurs on the upper and lower faces of the CCT specimen ([Chrysochoos and Louche, 2000]). Besides, the material density, ρ, the specific heat, c, and the thermal conductivity coefficient, k, are material constants independent from the internal state. Natural convection

in air is considered as a thermal boundary condition applied around the specimen (with $h = 10W.m^{-2}.K^{-1}$). Figure 2.9 illustrates the boundary conditions considered in the quarter model of the CCT specimen for solving the thermal problem.

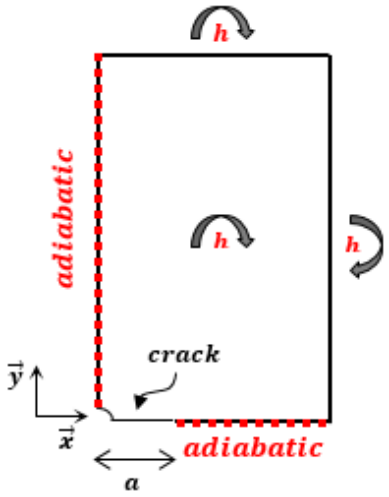

Figure 2.9: Schematic sketch showing the boundary conditions of the thermal problem.

Since the thermoelasic source is sinusoidal (Equation (2.17)), the solution of the heat diffusion equation (2.19) is also sinusoidal. Then, θ_{the} can be written as:

$$\theta_{the}(x, y, t) = \theta^a_{the}(x, y).\sin(2\pi ft + \varphi(x, y)) \tag{2.20}$$

where θ^a_{the} is the amplitude of the thermoelastic temperature variation field and φ denotes the phase shift between the thermoelastic temperature and the stress response resulting from the applied mechanical loading. The computation of the amplitude, θ^a_{the}, and the phase, φ, is carried out by using complex numbers technique for representing sinusoidal functions. This technique enabled to rearrange Equation (2.19) in an easier format simplifying its resolution by FEA.

Furthermore, the magnitude of φ should be constant unless adiabatic conditions are not met. This can be shown in Figure 2.10 where the phase shift is computed and plotted along x axis. It can be observed that φ changes at the crack tip because of important heat losses due to conduction and convection occurring in the same region.

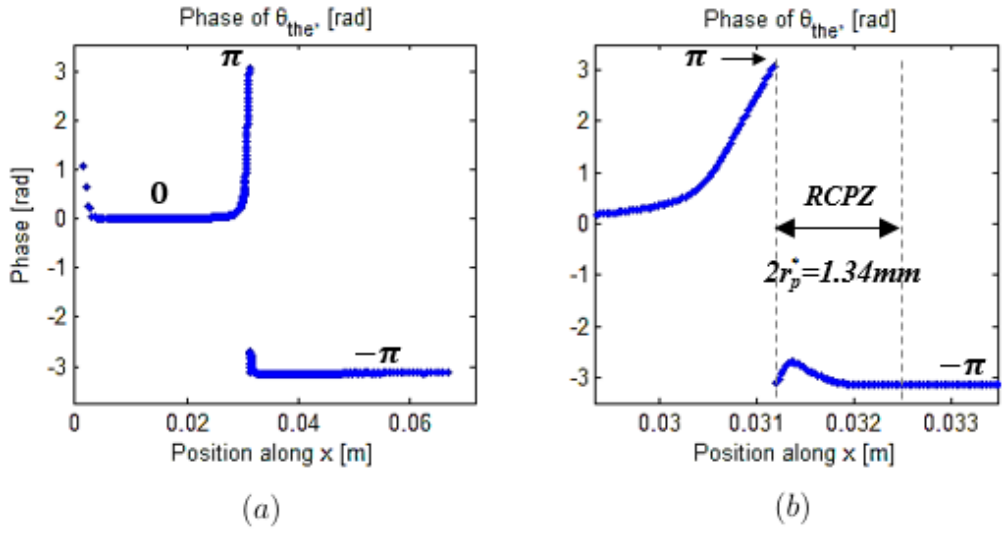

Figure 2.10: (a) Evolution of φ along x axis. (b) Zoom near the crack tip region.

Figure 2.11 below shows the field of the thermoelastic temperature amplitude, θ^a_{the}, as well as its evolution along x axis. It can be seen that θ^a_{the} is also singular at the crack tip, which is a result of the singularity of the thermoelastic source amplitude (Figure 2.8).

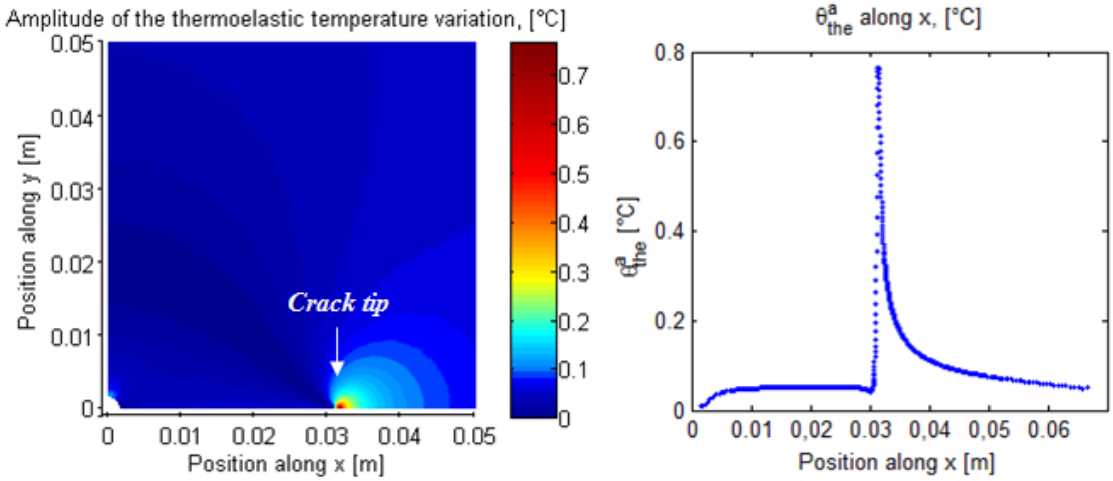

Figure 2.11: Amplitude of the thermoelastic temperature variation, θ^a_{the}, computed with the loading configuration: $a = 31.3mm$, $f = 98.6Hz$, $\Delta K_I = 26MPa.\sqrt{m}$, and $T_0 = 20°C$.

Having presented the numerical method of computing the thermoelastic source and its resulting temperature field, the next section presents the experimental method of estimating the intrinsic dissipation due to microplasticity, d_1, and its associated

temperature field in the CCT plate.

2.4.2 The intrinsic dissipation due to microplasticity

As explained before in Section §2.2, the intrinsic dissipation due to microplasticity, d_1, is linked to the amplitude of the normal stress applied to a smooth uncracked specimen, through the self-heating curve. In the case of this problem which deals with cracked specimens, the applied normal stress amplitude is not homogeneous in the material because the stress state near the crack tip is heterogeneous and multiaxial. Additionally, the intrinsic dissipation, d_1, is due to microplasticity. Having considered these two conditions, it is assumed that, in this case, the intrinsic dissipation, d_1, is linked to the Von Mises equivalent stress and not to the amplitude of the normal stress. Thus, by computing the field of the Von Mises equivalent stress, the self-heating curve can be used to estimate the intrinsic dissipation, d_1, in each point (elementary volume) of the CCT specimen. Hereinafter, the emphasis is first made on the method used for establishing the self-heating curve as a material intrinsic property.

In order to obtain the C40-steel self-heating curve, self-heating fatigue tests are carried out. They consist in applying load block series of cycles to a smooth uncracked specimen at room temperature with a constant normal stress amplitude, $\frac{\Delta\sigma}{2}$, and a constant load ratio, $R = \frac{\sigma_{min}}{\sigma_{max}}$, as illustrated in Figure 2.12.

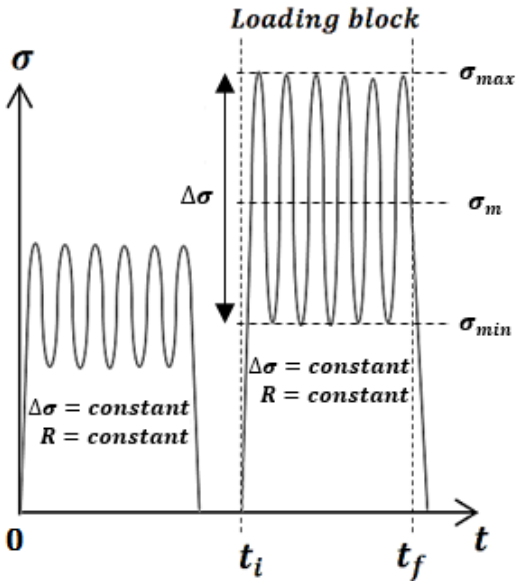

Figure 2.12: A schematic curve defining an applied loading block.

The fatigue machine used in this work is a resonant testing machine (or Vibrophore, as shown in Figure 2.13) with a load cell of $\pm 150kN$. It has mechanical grips fixing the specimen at the extremities. This is an advantage compared with hydraulic grips used in servohydraulic testing machines which heat up because of pressurized oil and may generate additional heating in the specimen during cyclic loading. Therefore, by the use of mechanical grips, heating of the griped regions of the specimen is neglected. It should also be mentioned that the central gauge zone of the specimen is far enough from the gripping system of the vibrophore. Moreover, in Figure 2.13, the use of a temperature control sample enabled to measure the reference temperature, T_0.

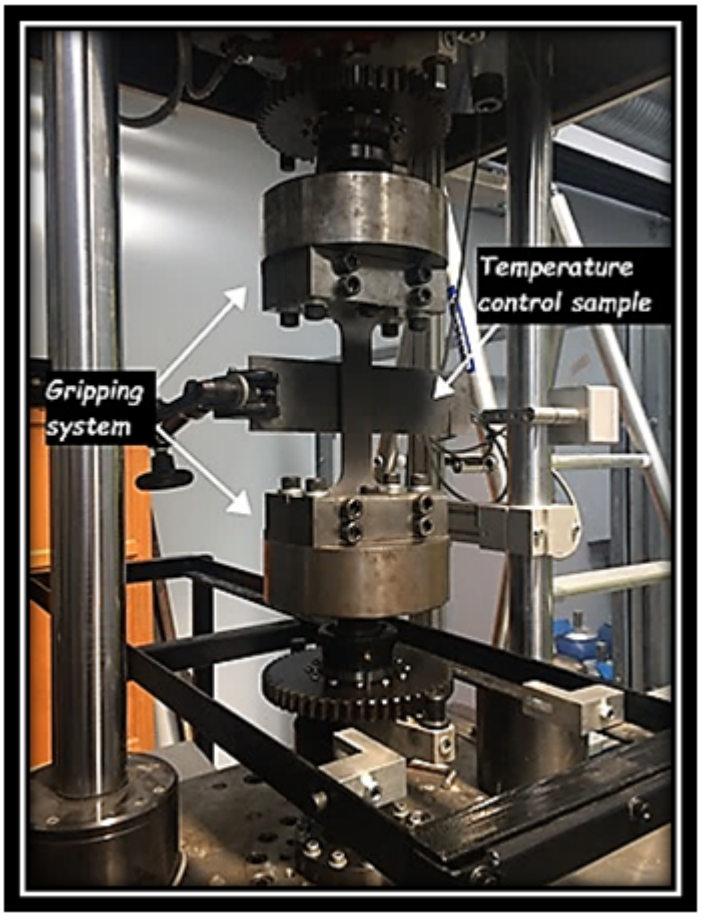

Figure 2.13: Fatigue device used in this work.

The geometry of the smooth uncracked specimens, made of C40-steel, has been designed to optimize the loading capacity of the vibrophore. It is based on a 'dog-bone' shape to get a uniform testing area enabling to sufficiently reach high stress

levels. This enables to prevent failure in the gripped portion of the specimen. Figure 2.14 shows the geometry of the specimens used during self-heating fatigue tests.

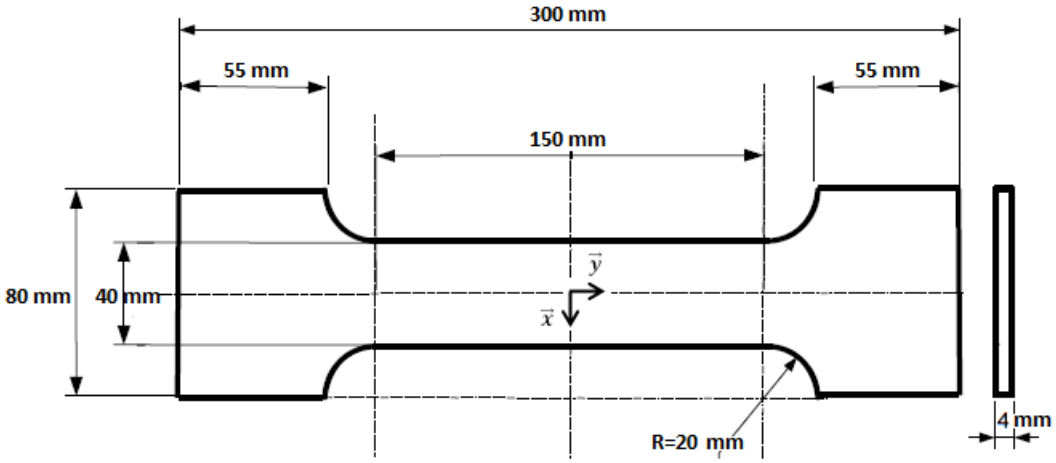

Figure 2.14: Geometry of the unnotched specimens made of C40 steel and used during self-heating fatigue tests.

During these tests, an infrared camera measures and records the temperature evolution on the specimen surface. The camera model used in this experimental investigation is FLIR SC7000 MWR. The measuring range of the camera has been chosen between $5°C$ and $300°C$, and the frequency acquisition and the integration time are respectively $5Hz$ and $600\mu s$. In order to enhance the temperature measurements, the surface of the specimen was covered by a thin layer of mat black paint used as a coating to increase the emissivity of the material surface and avoid reflections from the environment. Moreover, during the tests, the lens axis of the camera is kept fixed and perpendicular to the specimen surface. The infrared camera image resolution has been configured on 320×256 pixels ($1mm \approx 5px$) in order to observe the whole heating central gauge area.

Regarding experimental conditions, the applied load block series are performed in sinusoidal load-control with loading frequencies $83 \leq f \leq 94Hz$, at a room temperature around $20°C$. Table 2.3 presents the conditions of the load blocks applied during self-heating fatigue tests.

$Test\ ref.$	R	f (Hz)	Δt (s)	N $(cycles)$	σ_{max} (MPa)	σ_{min} (MPa)	$\frac{\Delta\sigma}{2}$ (MPa)	σ_m (MPa)
$S010$	0.1	93	215	19995	44.4	4.4	20	24.4
$S011$	0.1	93	206.4	19195	88.8	8.8	40	48.8
$S012$	0.1	92	2608.7	240000	133.3	13.3	60	73.3
$S013$	0.1	92	3728.26	343000	177.7	17.7	80	97.7
$S014$	0.1	91	3219.8	293000	200	20	90	110
$S015$	0.1	91	3483.5	317000	222.2	22.2	100	122.2
$S016$	0.1	90	3133.3	282000	244.4	24.4	110	134.4
$S017$	0.1	89	1977.5	176000	266.6	26.6	120	146.6
$S018$	0.1	89	2337	208000	288.8	28.8	130	158.8
$S019$	0.1	87	3448.3	300000	311.1	31.1	140	171.1
$S040$	0.4	93	2613	243000	66.6	26.6	20	46.6
$S041$	0.4	93	1125.8	104700	133.3	53.3	40	93.3
$S042$	0.4	93	860.2	80000	200	80	60	140
$S043$	0.4	92	934.8	86000	233.3	93.3	70	163.3
$S044$	0.4	92	1195.6	110000	266.6	106.6	80	186.6
$S045$	0.4	92	1608.7	148000	300	120	90	210
$S046$	0.4	92	2750	253000	316.6	126.6	95	221.66
$S047$	0.4	92	2478.2	228000	333.3	133.3	100	233.3
$S048$	0.4	91.5	1063.4	97300	366.6	146.6	110	256.6
$S070$	0.7	93	2236.5	208000	133.3	93.3	20	113.3
$S071$	0.7	94	638.3	60000	200	140	30	170
$S072$	0.7	93.6	1068.4	100000	233.3	163.3	35	198.3
$S073$	0.7	93	859.1	79900	266.6	186.6	40	226.6
$S074$	0.7	93	860.2	80000	300	210	45	255
$S075$	0.7	93	1258	117000	333.3	233.3	50	283.3
$S076$	0.7	92.3	1083.4	100000	366	256	55	311
$S077$	0.7	90	1777.8	160000	400	280	60	340
$S078$	0.7	88.7	958.3	85000	433.3	303.3	65	368.3
$S079$	0.7	87.7	1368.3	120000	466.6	326.6	70	396.6
$S0710$	0.7	87	1310.3	114000	500	350	75	425
$S0711$	0.7	85.6	1261.7	108000	533.3	373.3	80	453.3
$S0712$	0.7	83	576	47808	566.6	396.6	85	481.6

Table 2.3: Conditions of applied loading per block during self-heating fatigue tests.

Determining the intrinsic dissipation, d_1, directly from the temperature field measured by the infrared camera on the specimen surface, is an ill-posed inverse problem that is complicated, nay impossible, to solve without information on the heat source distribution ([Capatina and Stavre, 2000]). However, for thin-flat specimens, several options may be proposed to simplify the problem.

Let T_d be the temperature measured by the infrared camera on the reduced-surface of the smooth uncracked specimen during self-heating fatigue tests. It is generated by the intrinsic dissipation effect and is assumed to be uniformly distributed in the reduced-area of the specimen because the material is homogeneous and the stress too. The link between T_d and d_1 is written according to the following heat-diffusion equation:

$$\rho.c.\frac{\partial\theta_d}{\partial t} - k.(\frac{\partial^2\theta_d}{\partial x^2} + \frac{\partial^2\theta_d}{\partial y^2}) + 2\frac{h}{e}.\theta_d = d_1, \tag{2.21}$$

established within the same assumptions as those considered to write the thermal problem with the thermoelastic source presented in the previous section. The quantity, θ_d, denotes, $T_d - T_0$, and is the temperature variation due to the intrinsic dissipation, d_1, in the smooth uncracked specimen. In Equation (2.21), d_1 is an averaged volume power over one loading cycle.

According to [Chrysochoos et al., 2012], like stress and strain fields, it may be supposed that, before localization onset, the distribution of the intrinsic dissipation is uniform at any time within the specimen gauge part. This is consistent with a classical view of homogeneous uniaxial tests. In such cases, the spectral solution of the heat-diffusion equation (2.21) can be analytically determined using eigenfunctions of the Laplacian operator $\left(\frac{\partial^2\theta_d}{\partial x^2} + \frac{\partial^2\theta_d}{\partial y^2}\right)$. For symmetric linear boundary conditions and initial conditions corresponding to uniform temperature fields, the spectral solution can then be well approximated by only considering the first eigenfunction. Then, the heat-diffusion equation (2.21) becomes an ordinary differential equation and can be written as ([Chrysochoos and Louche, 2000]):

$$\frac{\partial\theta_d}{\partial t} + \frac{\theta_d}{\tau} = \frac{d_1}{\rho.c} \tag{2.22}$$

where θ_d is now the temperature variation measured at the center of the smooth uncracked specimen gauge part, and τ is a time constant characterizing local heat losses. Practically, θ_d identifies the mean temperature, of a small centered area, measured by the infrared camera in the reduced-surface of the smooth uncracked specimen. To avoid confusion, this mean temperature is hereinafter denoted by $\bar{\theta}_d$.

As mentioned before in Figure 2.1 at the end of Section §2.1.1, during each applied loading block of self-heating fatigue tests, the intrinsic dissipation, d_1, can be assumed constant over time. It can then be quantified from Equation (2.22) in the stabilized regime of temperature. As a result, d_1 is estimated as follows:

$$d_1 = \frac{\rho.c}{\tau}.\bar{\theta}_d^{sta}, \tag{2.23}$$

where $\bar{\theta}_d^{sta}$ is identified as the mean temperature variation, measured in the stabilized regime, of a small centered area in the reduced-surface of the smooth uncracked specimen.

Figure 2.15 shows an example of the evolution of the mean temperature $\bar{\theta}_d$ over time, experimentally measured by the infrared camera under the experimental conditions of the self-heating fatigue test referenced by $S019$ in Table 2.3. It is spatially averaged over the blue area with a size of $15 \times 10mm$ (Figure 2.15). For this example, $\tau = 285s$ and $\bar{\theta}_d^{sta} = 14.7°C$. Therefore, according to Equation (2.23), d_1 is estimated to be equal to $179.56kWm^{-3} \pm 0.855kWm^{-3}$. The uncertainty on this estimation comes from the thermal noise of the camera ($0.07°C$). However, this uncertainty remains very small compared with the value of d_1.

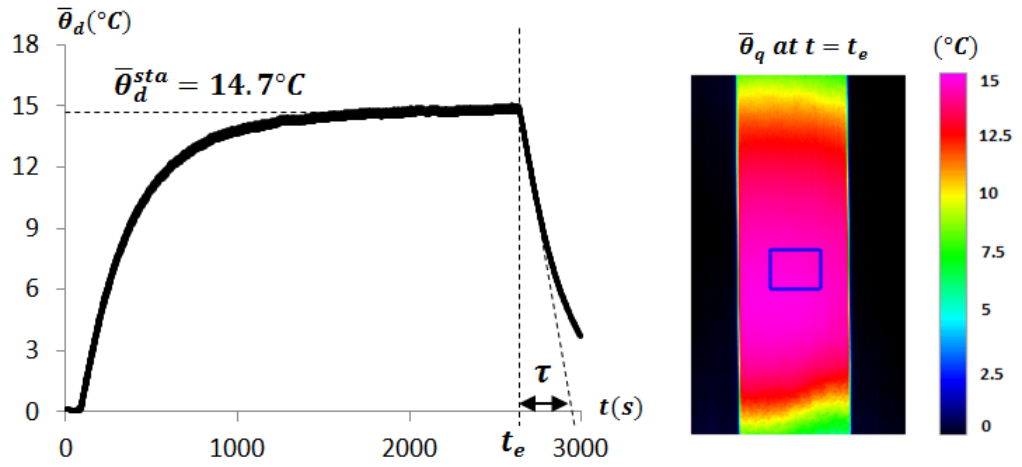

Figure 2.15: Example of C40 steel self-heating measurement under the loading conditions of the self-heating fatigue test $S019$: $\frac{\Delta\sigma}{2} = 140MPa$, $f = 87Hz$, $R = 0.1$.

With the same method, the intrinsic dissipation, d_1, is estimated for all the applied self-heating fatigue tests, referenced by $S0XY$ and listed in Table 2.3, under three applied load ratios: $R = 0.1$, $R = 0.4$ and $R = 0.7$. This enabled to plot

the self-heating curves of C40-steel, depicted in Figure 2.16, which show a non-linear relationship between the intrinsic dissipation, d_1, and the applied normal stress amplitude, $\frac{\Delta\sigma}{2}$. In these self-heating curves, each point corresponds to a configuration of applied loading blocks $S0XY$.

It must be pointed out that the points plotted in the self-heating curves are assessed at $f = 100Hz$ by using the linear dependence between the intrinsic dissipation, d_1, and the loading frequency, f. In other words, if d_1 is first assessed with a loading frequency f^a, then with a loading frequency f^b, d_1 must be multiplied by f^b/f^a, [Berthel et al., 2007]. This has been done since the real loading frequency is not exactly the same at each stress amplitude, and that because of the change in dissipation (specimen self-heating).

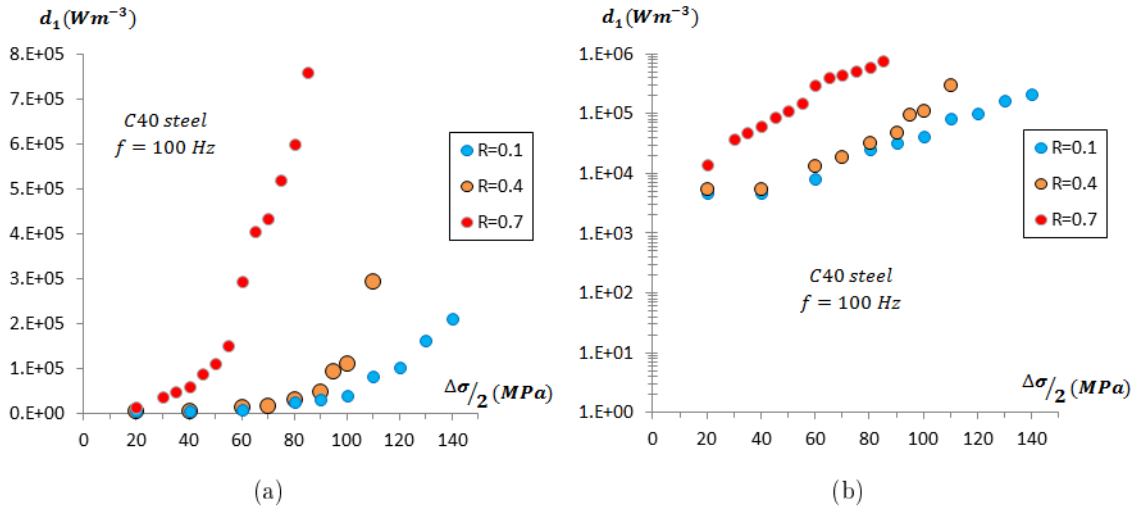

Figure 2.16: Self-heating curves of C40 steel plotted in: (a) linear scale, and (b) logarithmic scale.

From Figure 2.16, it can be seen that for a fixed stress amplitude, the higher the R-ratio, the higher the intrinsic dissipation d_1.

Thus, for a given load ratio R and a stress amplitude $\frac{\Delta\sigma}{2}$, the intrinsic dissipation d_1 can be identified from the corresponding self-heating curve.

As said earlier in this section, estimating the intrinsic dissipation in a cracked material is done through the calculation of the Von Mises equivalent stress. For this purpose, the two-dimensional quarter model of the CCT specimen as well as its boundary conditions, presented in the previous section for calculating the thermoelastic source, are considered here for computing the field of the Von Mises equivalent stress resulting from an applied normal stress amplitude.

The Von Mises equivalent stress, denoted by σ_{eq}, is defined as follows:

$$\sigma_{eq}(x,y) = \sqrt{\frac{3}{2}.\bar{\bar{\sigma}}_{d,a} : \bar{\bar{\sigma}}_{d,a}(x,y)}, \tag{2.24}$$

where $\bar{\bar{\sigma}}_{d,a}(x,y)$ is the deviatoric part of the stress tensor defined by:

$$\bar{\bar{\sigma}}_{d,a}(x,y) = \bar{\bar{\sigma}}_a(x,y) - \frac{1}{3}.\mathrm{Tr}(\bar{\bar{\sigma}}_a(x,y)).\bar{\bar{1}}, \tag{2.25}$$

where $\bar{\bar{\sigma}}_a$ is the amplitude of the stress tensor response in the cracked material subjected to a normal stress amplitude $\frac{\Delta\sigma}{2}$.

The example of loading configuration considered in the previous section is reused here to highlight the numerical calculation by FEA of the field of the Von Mises equivalent stress. It concerns the quarter model of the CCT specimen with a crack length $a = 31.3mm$, subjected to an applied SIF range $\Delta K_I = 26MPa.\sqrt{m}$ equivalent to an applied normal stress amplitude $\frac{\Delta\sigma}{2} = 44.6MPa$ at its upper edge, and a load ratio $R = 0.1$. Figure 2.17 depicts the resulting field of the Von Mises equivalent stress.

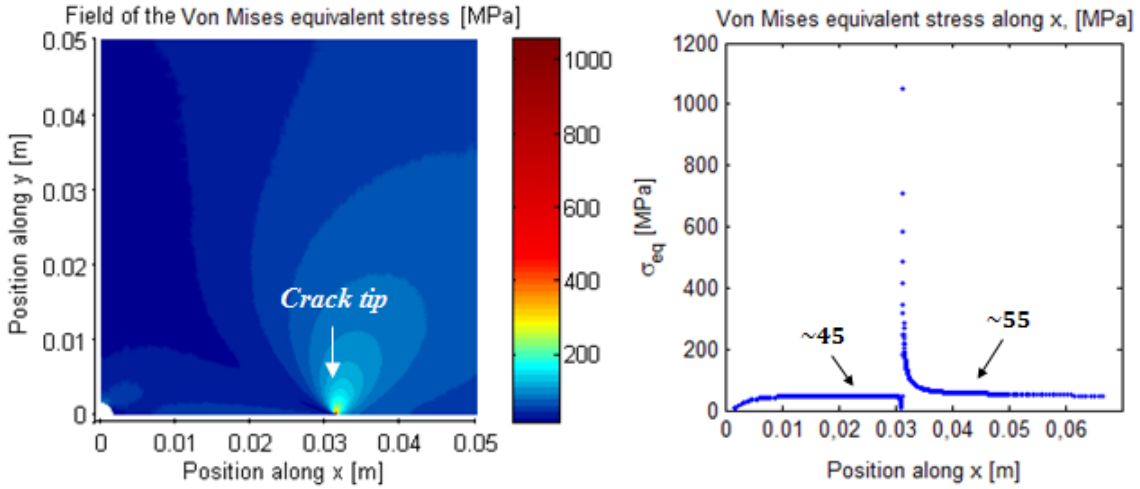

Figure 2.17: Amplitude of the Von Mises equivalent stress, σ_{eq}, computed in the CCT specimen with $a = 31.3mm$, under $\Delta K_I = 26MPa.\sqrt{m}$ (*i.e.* $\frac{\Delta\sigma}{2} = 44.6MPa$), and $R = 0.1$.

It can be seen in Figure 2.17 that the Von Mises equivalent stress field is singular at the crack tip, but it should be noted that this singularity does not have a consequence on the intrinsic dissipation due to microplasticity since it is estimated outside the RCPZ where it is supposed to have a major role. Indeed, in the RCPZ the ma-

jor role is supposed to be played by cyclic plasticity. In this calculation model, the RCPZ is defined with the criterion $\sigma_{eq} \geq \sigma_y^{cyc.}$, where $\sigma_y^{cyc.} = 200MPa$ is the cyclic yield stress of C40-steel. Close to the RCPZ, the values of the computed Von Mises equivalent stress are higher than the values of the stress amplitude plotted in the self-heating curves (Figure 2.16). It should be known that during self-heating fatigue tests, it was not possible to apply a stress amplitude higher than that plotted in Figure 2.16 because of the problem of sliding, occurring at high applied loads, between the specimen and the grips of the fatigue machine. That is why, the self-heating curves are extrapolated till $\frac{\Delta\sigma}{2} = 200MPa$.

Figures 2.18, 2.19, and 2.20, below, show the polynomial extrapolation of the three self-heating curves separately plotted, for the three applied load ratios, $R = 0.1$, $R = 0.4$, and $R = 0.7$, respectively. It can be seen that these extrapolations remain rough and can be used as first approximations to provide an order of magnitude estimate of the intrinsic dissipation due to microplasticity, d_1, close to the RCPZ.

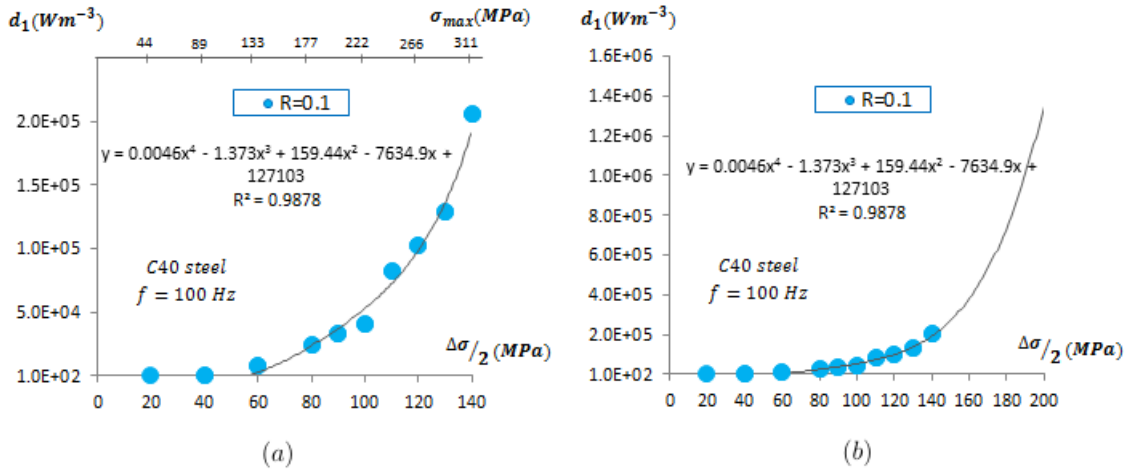

Figure 2.18: (a) Experimental self-heating curve at $R = 0.1$, (b) extrapolation of the self-heating curve till $\frac{\Delta\sigma}{2} = 200MPa$.

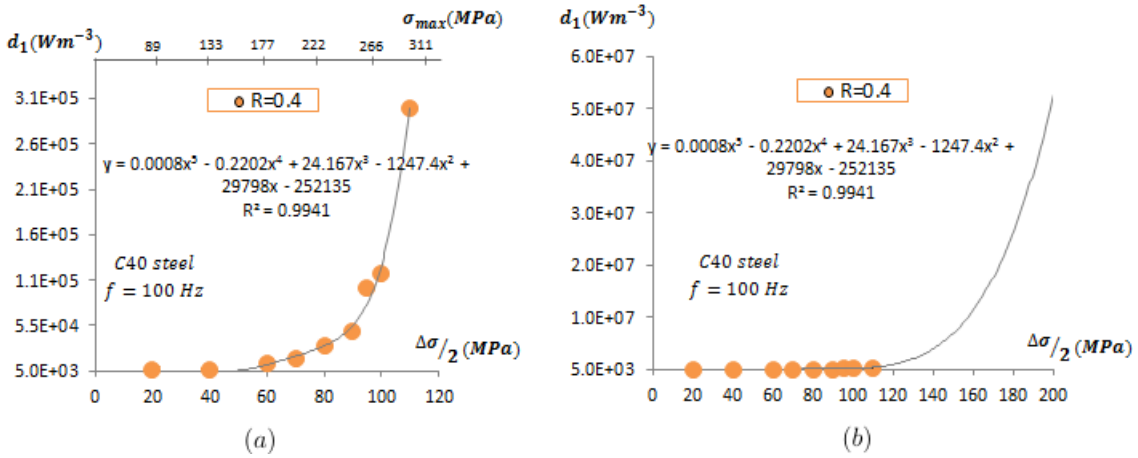

Figure 2.19: (a) Experimental self-heating curve at $R = 0.4$, (b) extrapolation of the self-heating curve till $\frac{\Delta\sigma}{2} = 200MPa$.

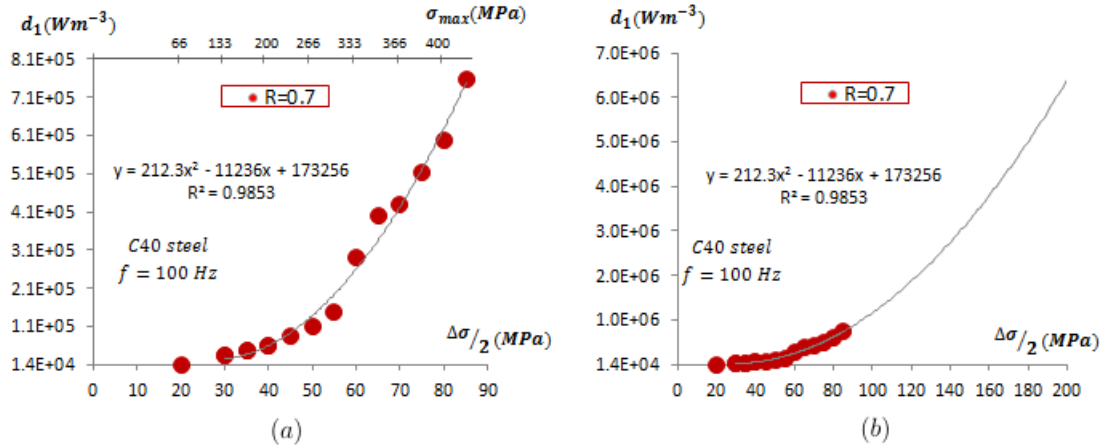

Figure 2.20: (a) Experimental self-heating curve at $R = 0.7$, (b) extrapolation of the self-heating curve till $\frac{\Delta\sigma}{2} = 200MPa$.

Therefore, these self-heating curves can be used in order to estimate the field of the intrinsic dissipation due to microplasticity in the CCT specimen. Indeed, for each point in the CCT specimen, outside the RCPZ, the value of the computed Von Mises equivalent stress (Figure 2.17) is read on the self-heating curve (on the axis of stress amplitudes), and thus, the corresponding value of the intrinsic dissipation is estimated.

It must be pointed out that the load ratio near the crack tip of a cracked material is not the same as the applied one. Indeed, by considering for example an elastic perfectly plastic material, let $\sigma_y^{cyc.}$ be the cyclic yield stress of the material, according to the cyclic plasticity behavior explained by [Rice, 1967] and previously presented in

Figure 1.7 (Section §1.1 in Chapter I), the load ratio inside the RCPZ is: $R = \frac{\sigma_{min}}{\sigma_{max}} = \frac{-\sigma_y^{cyc.}}{\sigma_y^{cyc.}} = -1$ no matter what the applied R-ratio is. Therefore, for an elastic-plastic material, the R-ratio in the region ahead of the crack tip may differ from the applied one. However, since the conditions of the LEFM are fulfilled, in particular the small scale yielding condition, the R-ratio outside the RCPZ can be assumed as same as the applied load ratio. Thus, the intrinsic dissipation due to microplasticity, d_1, can be estimated outside the RCPZ with a constant load ratio equal to the applied one.

For the example of loading configuration considered before, let $R = 0.1$ be the applied load ratio and $f = 100Hz$ be the loading frequency. Figure 2.21 depicts the field of the intrinsic dissipation, d_1, in the quarter model of the CCT specimen.

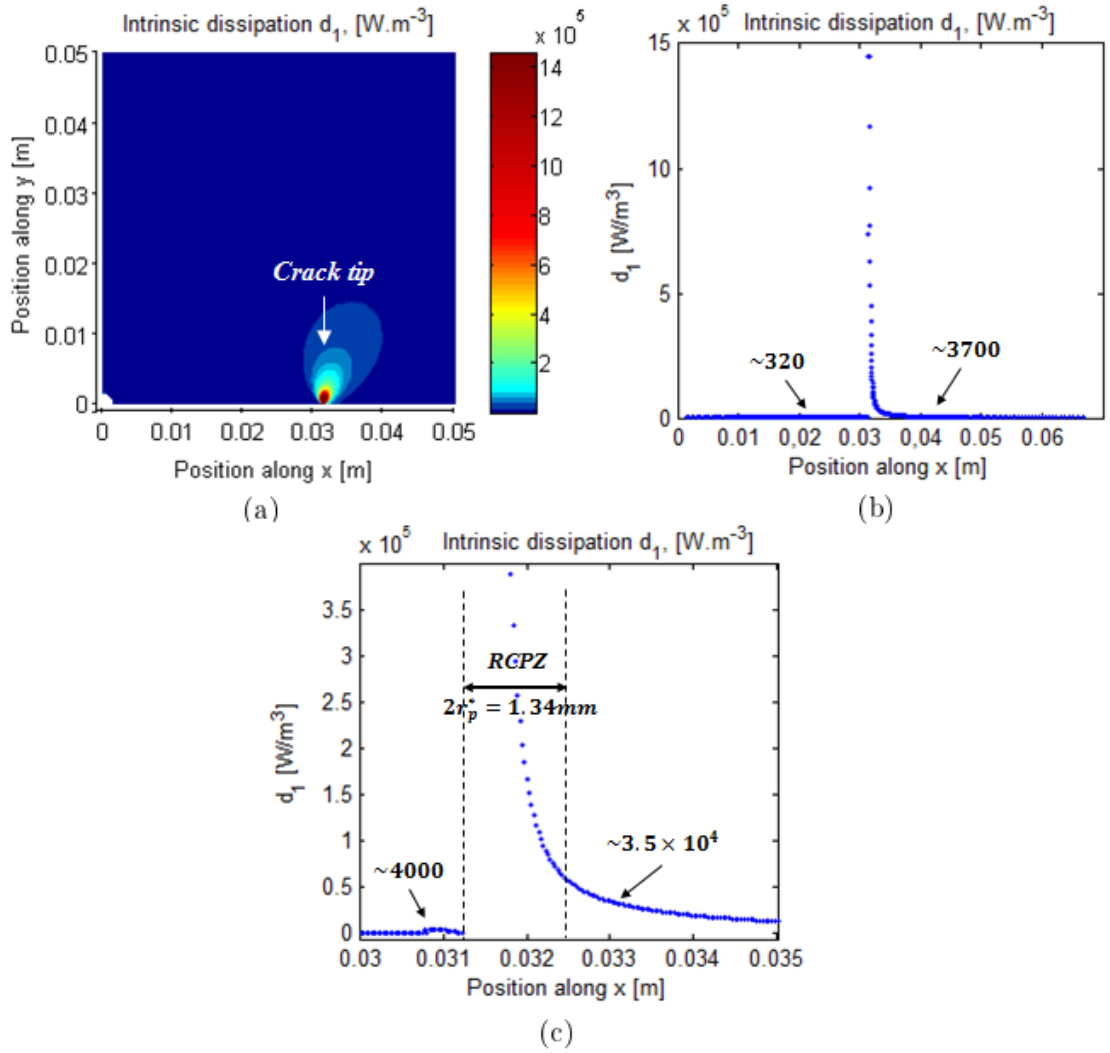

Figure 2.21: Field of the intrinsic dissipation, d_1, with the loading configuration $a = 31.3mm$, $\Delta K_I = 26MPa.\sqrt{m}$, $R = 0.1$, and $f = 100Hz$. (a) Zoom near the crack tip region, (b) evolution of d_1 along x axis, and (c) zoom near the RCPZ.

It should be noted that the estimation of d_1 is assumed to be valid outside the RCPZ modeled by a disc shape with a diameter, $2r_p^* = 1.34mm$ in this loading case, according to Irwin's model (Equation (1.9) in Chapter I). Actually, it is the same model used to represent the RCPZ in the quantification of the two other heat sources, s_{the} and q, and this also simplifies the comparison of the thermal effects generated by the three heat sources.

Now, in order to compute the temperature variation field, θ_d, generated in the CCT specimen by the effect of the intrinsic dissipation due to microplasticity, the associated thermal problem (Equation (2.21)) is solved in transient regime by FEA with the same assumptions and boundary conditions used to write the thermal problem associated with the thermoelastic source (*cf.* previous section).

Within the example of loading configuration considered in the numerical calculations above, let $\Delta t = 258.4s$ be the duration of the cyclic loading. *It actually corresponds to a real duration of a fatigue crack growth test carried out for estimating the heat source q.* Figure 2.22, depicts the temperature variation field, θ_d, computed at the end of cyclic loading (at $t = 258.4s$).

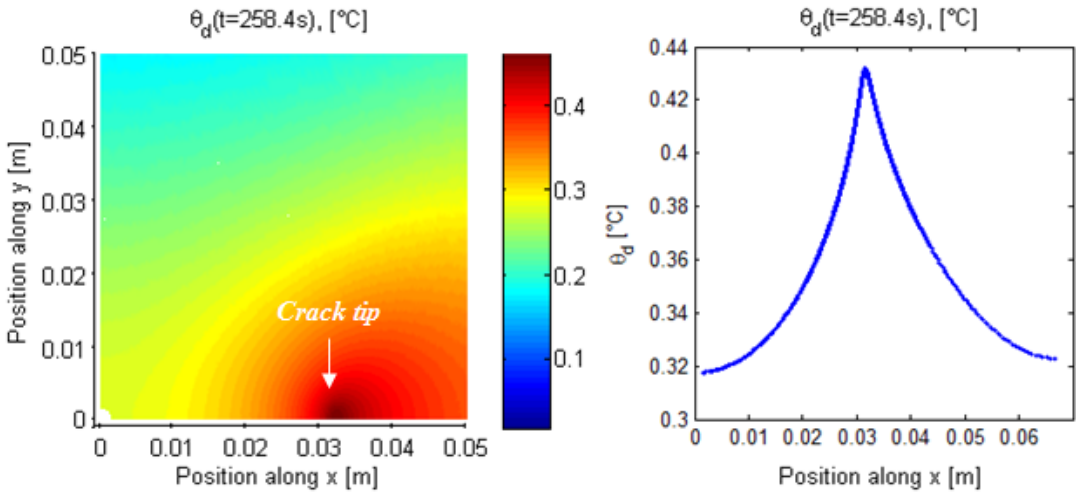

Figure 2.22: Field of the temperature variation, θ_d, generated by the intrinsic dissipation, d_1, at $t = 258.4$ of the fatigue test with the loading configuration: $a = 31.3mm$, $\Delta K_I = 26MPa.\sqrt{m}$, $R = 0.1$, and $f = 100Hz$.

In the following, the estimation of the cyclic plasticity dissipated into heat in the RCPZ, q, as well as the computation of its associated temperature field are discussed.

2.4.3 The cyclic plasticity dissipated into heat in the RCPZ

The cyclic plasticity dissipated into heat in the RCPZ, q, is estimated by using the method proposed by [Ranc et al., 2014]. It is based on infrared measurements of the temperature field generated around the crack tip during fatigue crack growth tests carried out with the CCT specimen previously illustrated in Figure 2.4. The same fatigue testing machine (vibrophore) and infrared camera, presented in the previous section, are used in this experimental investigation. It should be known that the fatigue crack growth tests were carried out in this work within the framework of the LEFM, that is why the following conditions were considered during the fatigue crack growth tests:

- The RCPZ is modeled by a disc whose radius, r_p^*, is estimated under the plane stress hypothesis (*cf.* Equation (1.9) in Chapter I). During the tests, r_p^* should be small compared with the crack ligament size.
- The amplitude of the nominal applied stress over the crack ligament does not exceed the cyclic yield stress of the material, $\sigma_y^{cyc} = 200MPa$.
- The applied SIF range, ΔK_I, is assumed to be constant during an applied fatigue load block. Actually, the initial applied SIF range, ΔK_{I_i}, changes as the fatigue crack propagates, and the duration of each applied fatigue load block is defined so that the final applied SIF range, ΔK_{I_f}, does not exceed 7% of ΔK_{I_i}. With this criterion ([ASTM-E647, 2013]), it can be assumed that ΔK_I remains constant during one applied fatigue load block.
- To apply a new load block, the applied maximum SIF, $K_{I_{max}}$, must be greater than the SIF range ΔK_{I_f} applied in the last block. This enables to avoid an underload effect on the fatigue crack.
- At the end of an applied fatigue load block, a new RCPZ must be created. In other words, the crack must be propagated outside the RCPZ created during the last block so that the cyclic plasticity dissipated into heat, q, generated during the current load block, would not be affected by that of the previous load block.

It should be noted that the CCT specimens were pre-cracked under load-controlled cyclic loading with a load ratio R close to zero ($R = 0.01$) in order to initiate a natural fatigue crack of about $2mm$ at the tips of the initial central notch. Moreover, a high resolution optical camera was used to measure the initial and final lengths

of the crack, a_i and a_f, respectively. The lengths of the two cracks propagating from the central notch of the CCT specimen are close (the maximum difference is less than $0.5mm$), thus only one crack side is observed during this experimental investigation. It should be mentioned that during fatigue testing, one side of the CCT specimen is facing the optical camera, and the other side is facing the infrared camera.

In Table 2.4, all the fatigue crack growth tests carried out in this work are presented. The crack size, a, denotes the half-length measured from the center of the hole of the CCT specimen (as illustrated before in Figure 2.4).

$Test$ $ref.$	R	f (Hz)	Δt (s)	a_i (mm)	ΔK_i $(MPa.\sqrt{m})$	a_f (mm)	ΔK_f $(MPa.\sqrt{m})$	$\frac{\Delta K_f - \Delta K_i}{\Delta K_i}$ $(\%)$	$2r_p^*$ (mm)
$T011$	0.1	100.1	974	14.8	13	16.8	13.85	6.5	0.32
$T012$	0.1	100	405	16.8	16	18.4	16.7	4.3	0.50
$T013$	0.1	99.5	211	18.4	20	20.8	21.3	6.5	0.79
$T014$	0.1	99	313	23.8	23	27.1	24.5	6.5	1.05
$T015$	0.1	98.6	258.4	27.1	26	31.3	28	7.3	1.34
$F016$	0.1	98.2	169	29.8	30	35.8	32	6.6	1.79
$F017$	0.1	97.7	184.2	35.8	32	41	34.2	6.8	2.02
$F018$	0.1	97	179.3	41	34	47.4	36.5	7.3	2.28
$T041$	0.4	99.6	261	21.2	13	22.6	13.4	3	0.32
$T042$	0.4	99.4	523.1	22.6	16	25.7	17	6.2	0.50
$F043$	0.4	98.7	344.4	25.7	20	29.3	21.3	6.5	0.79
$F044$	0.4	98.4	170.6	29.3	23	31.3	23.7	3	1.05
$F045$	0.4	97.6	237.6	31.3	26	36	27.8	6.9	1.34
$F046$	0.4	97	82.4	36	30	41.8	32.3	7.6	1.79
$T061$	0.6	98.4	614.5	17.7	13	19.3	13.5	3.8	0.32
$F062$	0.6	98	673.4	19.3	14.5	22.7	15.7	8.2	0.40
$F063$	0.6	97.7	563.9	22.7	16	26.1	17.1	6.8	0.50

Table 2.4: Applied loading conditions per block during fatigue crack growth tests.

The tests referenced by $T0XY$ in Table 2.4 satisfy the conditions of the LEFM presented above, while the tests referenced by $F0XY$ do not verify the small scale yielding condition as the crack ligament yields during these tests. The infrared data resulting from the tests $F0XY$ are not used in the calculations presented later in this thesis.

Before explaining the way the heat source, q, is estimated, it is important to present the following assumptions considered for this aim:

- The cyclic plasticity, resulting from the cyclic plastic strain occurring in the RCPZ, is mostly converted into heat. About 90% of the plastic energy is dissipated into heat for metals according to [Farren and Taylor, 1925] and [Taylor and Quinney, 1934]. Moreover, it is positive and assumed to be constant during one applied load block.

- During fatigue crack growth tests, between the beginning and the end of one applied load block, the loading frequency changes of about $0.5Hz$. It is assumed that this change in the loading frequency is negligible and has no effect on the heat source q during one applied load block.

- In the numerical calculations presented afterward, the distribution of the heat source q in the RCPZ is modeled by a spot positioned at the center of the RCPZ. This assumption was verified in [Ranc et al., 2011] where a two-dimensional calculation is presented to compare the temperature variation fields generated by: (i) a spot heat source centered in the RCPZ, and (ii) a uniformly distributed heat source in the RCPZ with a disc shape. They found that outside the plastic zone, the temperatures computed with these two assumptions are very close: for the size of the RCPZ, $2r_p^* = 4\mu m$, the relative difference is about 0.03%. But inside the RCPZ the temperature can be very differently distributed. Therefore, since this work is focused on the effect of the temperature gradient on the stress state outside the RCPZ in order to calculate its consequence on the SIF, the assumption of a spot heat source, q, is considered.

- During the applied load blocks of fatigue crack growth tests, the heat source q is assumed to be stationary for solving the thermal problem in the following. That can be verified by calculating the Peclet number which compares the characteristic time of the crack growth rate with the characteristic time of thermal diffusion. The Peclet number is defined as : $Pe = \frac{L.v}{D}$ with L is a characteristic length of the crack, v is the crack growth rate and D is the thermal diffusivity. For the typical values measured during fatigue crack growth tests: $L = 20mm$ and $v = 0.01mm.s^{-1}$, and for the typical value of the thermal diffusivity in medium carbon steels: $D = 1.5 \times 10^{-5} m^2.s^{-1}$, the Peclet number value is $Pe = 2 \times 10^{-3}$, which is very small compared with unity. As a result, the crack front moving is slow and the heat source q has enough time

to diffuse during one applied load block. The heat source q could therefore be considered as stationary.

Within the scope of these assumptions and by using the two-dimensional model of the thermal problem written in Section §2.4.1, the temperature variation field, θ_q, related to the heat source q must conform to the following heat-diffusion equation:

$$\rho.c.\dot{\theta}_q - k.(\frac{\partial^2\theta_q}{\partial x^2} + \frac{\partial^2\theta_q}{\partial y^2}) + 2\frac{h}{e}.\theta_q = q.\delta(0), \tag{2.26}$$

with the same thermal boundary conditions as those presented in the thermal problem with the thermoelastic source in Section §2.4.1.

In this equation, q represents the dissipated power per unit length of the crack front. By using the linearity of this equation, the heat source q can be estimated as follows:

$$q = \frac{\Delta\bar{\theta}_q^{exp}(t_f)}{\Delta\bar{\theta}_{q_1}(t_f - t_i)}q_1, \tag{2.27}$$

where q_1 is the unit heat source ($q_1 = 1W.m^{-1}$), $\Delta\bar{\theta}_q^{exp}(t_f)$ is the total increase, between the beginning and the end of cyclic loading, of the temperature variation θ_q^{exp} measured by the infrared camera and spatially averaged over a small area named Area A ($1.6 \times 1.6mm$) located ahead of the crack tip as depicted in Figure 2.23.

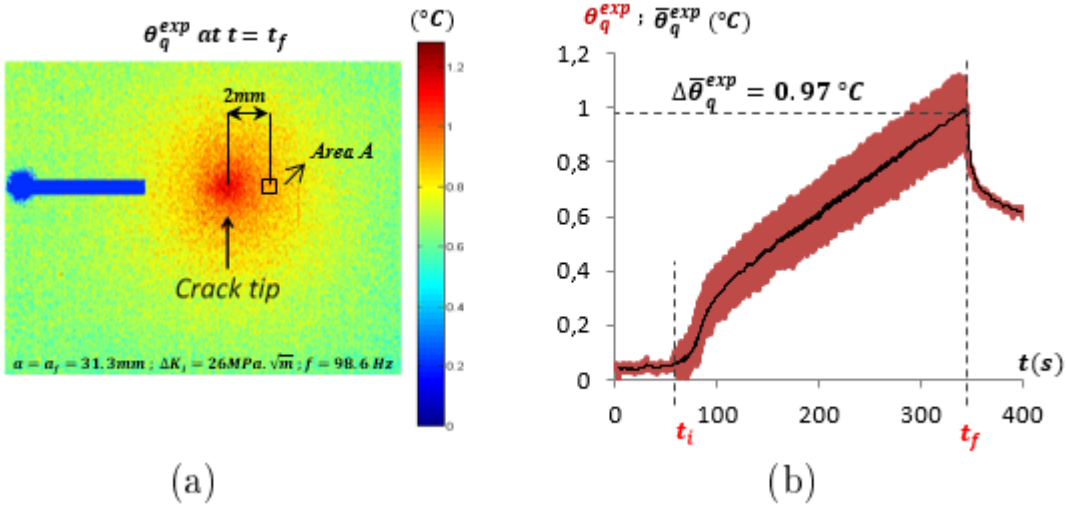

Figure 2.23: (a) Infrared measurement of θ_q^{exp} at the end of the applied load block of fatigue test $T015$. (b) Evolution of θ_q^{exp} and $\bar{\theta}_q^{exp}$, spatially averaged in Area A, against time during the whole applied loading block.

It must be noted that the temperature measured in Area A is considered due only to the heat source q. Indeed, it is true that in reality the overall sources are involved in this measurement area, but since the thermoelastic coupling fluctuates over time and the intrinsic dissipation due to microplasticity generates a small thermal effect, it is reasonable to relate the temperature increase measured near the crack tip, to the cyclic plasticity dissipated into heat in the RCPZ, q.

In Equation (2.27), $\Delta\bar{\theta}_{q_1}(t_f - t_i)$ is the total increase of the temperature variation calculated by FEA (Equation (2.26)) and spatially averaged in the finite element mesh over the same Area A, for $q = 1W.m^{-1}$, and at $t = t_f - t_i$ which is the duration of the applied load block between the initial and the final time of cyclic loading, t_i and t_f, respectively.

The temperature field mapping plotted on the left of Figure 2.23 corresponds to the end of the applied load block ($t = t_f$). As it can be observed, a heterogeneous temperature field is generated around the crack tip. It is assumed that this heterogeneous temperature field is due to the heat generated by the dissipation of cyclic plasticity in the RCPZ. The temperature oscillations appearing in the red curve plotted on the right in Figure 2.23 are due to the thermoelastic effect. The average temperature variation, $\bar{\theta}_q^{exp}$, is due to the cyclic plastic dissipation into heat, q, and is plotted by averaging the oscillating curve over a time series of $20s$. For this example of applied load block: $t_f - t_i = 258.4s$, $\Delta\bar{\theta}_q^{exp}(t_f) = 0.97°C$, and $\Delta\bar{\theta}_{q_1}(t_f - t_i) = 0.015°C$. Thus, $q = 64.6W.m^{-1} = 0.65J.m^{-1}.cycle^{-1}$, according to Equation (2.27).

As it can be seen, the estimation of the heat source, q, depends on the infrared measurements and may depend on the zone of measurements Area A. In the following, the effect of the thermal noise coming from the infrared camera as well as the effect of the position and size of the zone of measurements on the estimation of the heat source q are checked.

- **Effect of the thermal noise of the infrared camera**

To quantify the thermal noise of the infrared camera, let $\hat{\theta}(t_0)$ be the temperature variation averaged over Area A at $t = t_0$ where t_0 is an arbitrary time chosen before starting cyclic loading ($t_0 < t_i$). The standard deviation associated with the infrared measurements can be defined as:

$$\delta_{IR} = \sqrt{\frac{\sum_j \left(\theta_j(t_0) - \hat{\theta}(t_0)\right)^2}{n}}, \tag{2.28}$$

where j is the index of pixels in Area A, n is the total number of pixels in Area

A, and $\theta_j(t_0)$ is the temperature variation measured at the pixel j at $t = t_0$. For the example of infrared measurements given above in Figure 2.23, $\delta_{IR} = 0.069°C$. The effect on the estimation of q is quantified by calculating the associated standard deviation:

$$\delta_q = \frac{\delta_{IR}}{\Delta\bar{\theta}_{q_1}(t_f t_i)} q_1, \tag{2.29}$$

which leads to $\delta_q = 0.046 J.m^{-1}.cycle^{-1}$. It is very small compared with the value of the cyclic plastic dissipation into heat q ($q = 0.65 J.m^{-1}.cycle^{-1}$). Therefore, the effect of the infrared camera noise on the estimation of the heat source q can be neglected.

- **Effect of the size and the position of the measurement area**

As said above, the infrared measurements are spatially averaged over a small area ahead of the crack tip. The position of this area is roughly chosen outside the RCPZ because the calculation of $\Delta\bar{\theta}_{q_1}$ is assumed to be correct outside the RCPZ since the associated FEA is singular inside (problem of a spot heat source). For this purpose, the measurement area is placed ahead of the crack tip at a distance greater than the RCPZ size, but as close as possible in order to detect the temperature increase generated by the heat source q.

In order to check the sensitivity related to the location and the size of this measurement area, three area configurations are studied. Let Area A0 be the reference area positioned at $4mm$ from the crack tip with a size of $1.6 \times 1.6mm$. Let Area A1 be the double in size of Area A0, that being $3.2 \times 3.2mm$, positioned as same as Area A0, and finally let Area A2 be the same in size as Area A0, but positioned at a lower distance of $2mm$ from the crack-tip. For instance, under the conditions of the applied load block $T013$ ($a = 20.8mm$, $\Delta K_I = 20MPa.\sqrt{m}$, $R = 0.1$, and $f = 99.5Hz$), the heat sources q estimated from the infrared measurements in these three areas, with the same method presented above, are reported in the following table:

Area ref.	$\Delta\bar{\theta}_q^{exp}(°C)$	$\Delta\bar{\theta}_{q1}(°C)$	$q(J.m^{-1}.cycle^{-1})$
A0	0.39	0.012	0.326
A1	0.40	0.012	0.335
A2	0.45	0.014	0.323

Table 2.5: Effect of the infrared measurement area on the estimation of the heat source q.

As it can be seen, the quantification of the heat source q obtained with the three areas A0, A1, and A2, are very close. Therefore, for all of the fatigue crack growth tests $T0XY$ satisfying the conditions of the LEFM, the estimation of the heat source q is done with the same dimensions and location of the zone of measurements 'Area A' previously defined in Figure 2.23.

The results of the estimation of the heat source q for all the fatigue crack growth tests $T0XY$ are summarized in Table 2.6, where δ_q is the associated standard deviation originating from the infrared camera noise (Equation (2.29)).

Test ref.	R	ΔK_{I_i} $(MPa.\sqrt{m})$	f (Hz)	q $(W.m^{-1})$	q $(J.m^{-1}.cycle^{-1})$	δ_q $(J.m^{-1}.cycle^{-1})$
T011	0.1	13	100.1	23.023	0.23	0.035
T012	0.1	16	100	17	0.17	0.042
T013	0.1	20	99.5	31.84	0.32	0.044
T014	0.1	23	99	42.57	0.43	0.044
T015	0.1	26	98.6	64.09	0.65	0.039
T041	0.4	13	99.6	22.908	0.23	0.054
T042	0.4	16	99.4	26.838	0.27	0.041
T061	0.6	13	98.4	24.6	0.25	0.035

Table 2.6: Estimation of the heat source, q, generated during applied load blocks of fatigue crack growth tests $T0XY$ (*cf.* Table 2.4), and its associated standard deviation, δq $(q \pm \delta q)$.

In order to highlight the variation of the cyclic plastic dissipation into heat, q, in relation with the applied load controlled by the SIF range, ΔK_I, the curve of Figure 2.24 plots the evolution of the estimated heat sources, q, against the applied SIF ranges, ΔK_{I_i}, for the three load ratios applied in this experimental investigation.

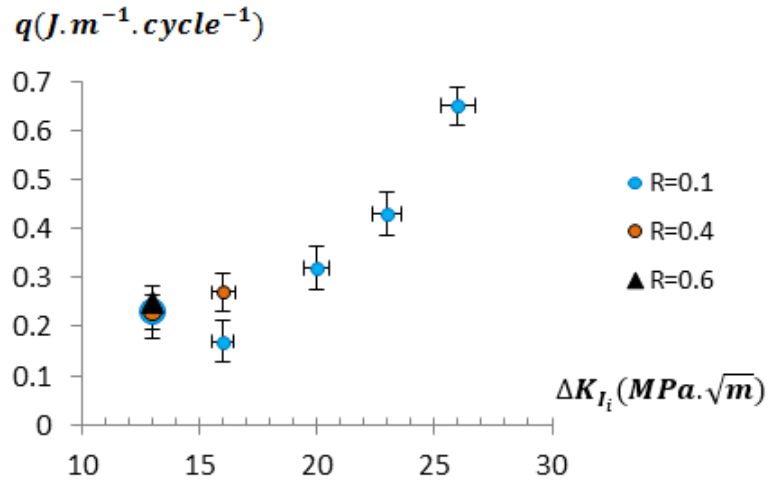

Figure 2.24: Evolution of the cyclic plastic dissipation into heat, q, against the applied SIF range ΔK_{I_i} and load ratio R.

It can be observed that for the applied SIF range $\Delta K_{I_i} = 13MPa.\sqrt{m}$, the three values of the heat sources q, obtained for the three applied R-ratios, coincide very closely. For $R = 0.1$ and $\Delta K_{I_i} \in [16, 26]$, the values of the heat source q increase and are almost lined up. However, the value of the heat source q at $\Delta K_{I_i} = 13MPa.\sqrt{m}$ seems startling and isolated, this may come from the effect of fracture behavior since the value of the corresponding applied ΔK_{I_i} is close to the threshold value ΔK_{th} (around $10MPa.\sqrt{m}$ for mild steels, [Farahmand and Nikbin, 2008]). Therefore, a change of the fracture mode may occur and affect the heat produced at the crack tip. Moreover, it is known that at near-threshold SIF there is a strong influence of microstructure which can be related to the change of the fracture mode, [Ritchie, 1979], this may therefore produce an extra self-heating due to microplasticity which would be converted into heat and then produce an additional heating to that resulting from the crack tip cyclic plasticity, hence the slight high value of q at $\Delta K_{I_i} = 13MPa.\sqrt{m}$ compared with that estimated at $\Delta K_{I_i} = 16MPa.\sqrt{m}$. Another question may raise upon this point concerns the crack length during this fatigue crack growth test (test $T011$ with $\Delta K_{I_i} = 13MPa.\sqrt{m}$) which is short since this test corresponds to the configuration when the initial crack just emanates from the central notch of the CCT specimen, so maybe the crack is still not long enough and that may affect the cyclic plastic dissipation into heat in the RCPZ.

For $\Delta K_{I_i} \in [16, 26MPa.\sqrt{m}]$ and $R = 0.1$, Figure 2.25 shows that the empirical data of the heat source q depending on the applied ΔK_{I_i} fit the following fourth power law: $q = 1E^{-6}.\Delta K_I^4 + 0.105$ with a correlation coefficient of 0.998. This agrees with the results found in the literature assuming that in the regime of the Paris law,

for many metallic materials, the plastic work spent during each cycle in the RCPZ has a ΔK^4 dependence ([Pippan and Stüwe, 1983] and [Klingbeil, 2003]).

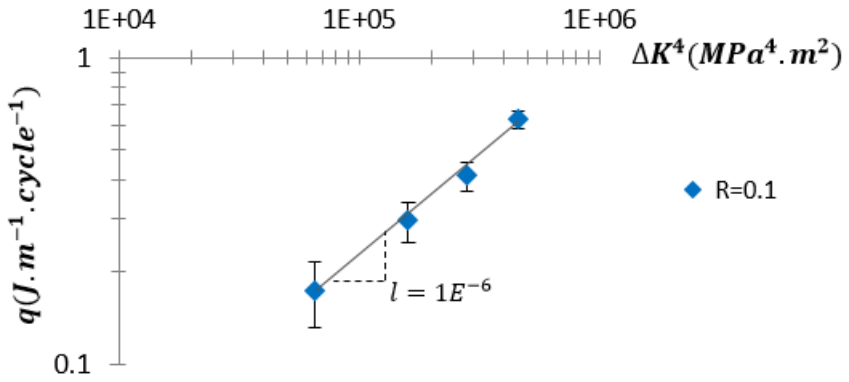

Figure 2.25: Cyclic plastic dissipation q vs. $\Delta K_{I_i}^4$ for $R = 0.1$ with C40 steel.

The estimated heat sources q at $R = 0.4$ and $R = 0.6$ are not enough numerous to investigate the ΔK_I^4 dependence at such load ratios. Actually, above the values of ΔK_{I_i} plotted in Figure 2.24, the small scale yielding condition is not fulfilled as the entire crack ligament of the CCT specimen yields. Thus, the hypothesis of the LEFM are no longer valid to define an elastic solution of the SIF range, ΔK_I.

After estimating the heat source q, the associated temperature variation field, θ_q, can be computed by FEA. In fact, the temperature variation field, θ_q^{exp}, measured by the infrared camera is not accurate enough in the vicinity of the crack tip, because the size of one pixel (about $200\mu m$) is barely close to the size of the RCPZ (*cf.* Table 2.4), particularly when the applied SIF range is low.

For this reason, the two-dimensional model of the thermal problem associated with the heat source q (Equation (2.26)) is numerically solved in transient regime by FEA. The temperature variation field, θ_q, is then computed according to the experimentally estimated heat source q.

For instance, by considering the loading configuration used in the two previous sections to compute the temperature variation fields, θ_{the}, and θ_d, namely: $a = 31.3mm$, $\Delta K_I = 26MPa.\sqrt{m}$, $R = 0.1$, and $f = 98.6Hz$, which actually corresponds to the configuration of the applied load block referenced by $T015$ (Table 2.4), the temperature variation field, θ_q, is computed with the associated dissipated power per unit length of the crack front, $q = 64.6W.m^{-1}$. Figure 2.26 depicts the distribution of the temperature variation field, θ_q, computed at $t = 258.4s$ which is

the time of the end of cyclic loading.

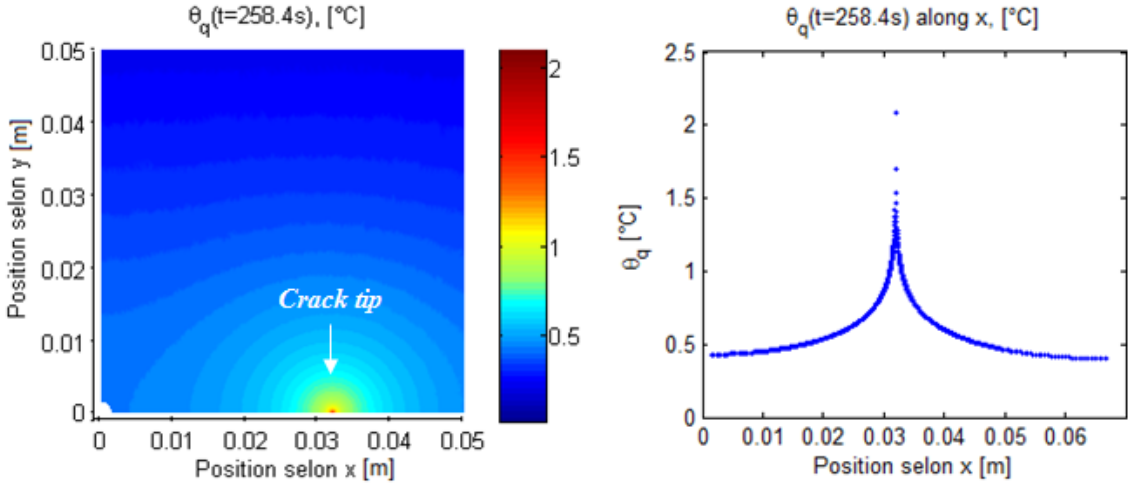

Figure 2.26: Field of the temperature variation, θ_q, generated by the heat source, $q = 64.6W.m^{-1}$, and computed at $t = 258.4s$ of the fatigue test $T015$: $a = 31.3mm$, $\Delta K_I = 26MPa.\sqrt{m}$, $R = 0.1$, and $f = 98.6Hz$.

In Figure 2.26, the peak of the temperature variation, θ_q, is reached at the crack tip region because of singularity due to the spot heat source q applied at the center of the disc modeling the RCPZ. Moreover, the computed values of θ_q are in a good agreement with the experimental measurements of θ_q^{exp} previously shown in Figure 2.23. This can be seen in Figure 2.27 which plots the two temperature variations, θ_q (the numerical solution), and θ_q^{exp} (obtained with infrared measurements), over the x axis. It can then be concluded that the computed θ_q does give a good approximation of what locally happens around the RCPZ.

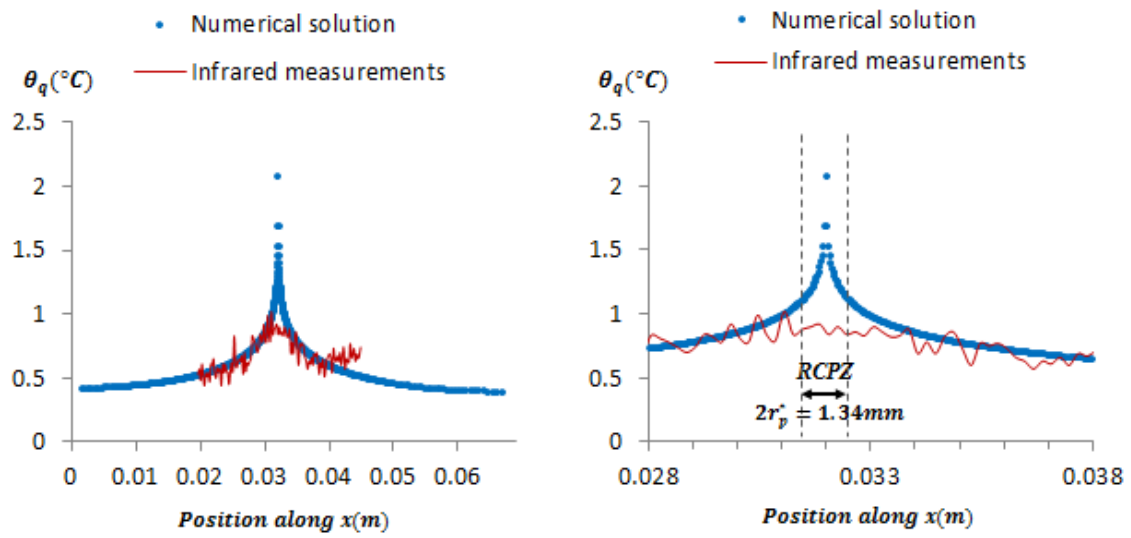

Figure 2.27: Evolution of the computed temperature variation, θ_q, and the measured temperature variation, θ_q^{exp}, along x axis.

2.5 Conclusion of Chapter II

By way of conclusion of this chapter, the three types of heat sources, generated in a thin-flat CCT specimen and subjected to cyclic loading, are characterized based on continuum thermodynamics, then the methodology for identifying each heat source is presented. Their resulting temperature fields are separately computed by solving a two-dimensional model of the heat diffusion problem. The linearity of the heat diffusion equation is used for this purpose.

In the finite element calculations presented in this chapter, the same applied loading configuration is considered: a quarter model of the CCT specimen made of C40 steel with a crack-length of $a = 31.3mm$, subjected to an applied SIF range $\Delta K_I = 26MPa.\sqrt{m}$, with a load ratio $R = 0.1$ and a loading frequency $f = 98.6Hz$. This configuration was considered to highlight the calculation methodology which remains the same for all the applied loading of fatigue crack growth tests fulfilling the conditions of the LEFM.

The thermoelastic source is numerically computed within the classical framework of linear thermoelasticity. The resulting thermoelastic temperature amplitude is singular at the crack tip, and this comes from the singularity of the linear-elastic model used to solve the thermoelastic source amplitude.

The intrinsic dissipation is estimated in the CCT specimen outside the RCPZ by first computing the Von Mises equivalent stress field and then using the self-heating

curve associated with the applied load. One drawback of this method is that of rough extrapolation of the self-heating curve in order to reach the amplitude of the Von Mises equivalent stress near the RCPZ region. A solution can be proposed here as a prospect to correct this problem, that of optimizing the geometry of the smooth uncracked specimens, used during self-heating fatigue tests, in order to reach higher applied stress amplitudes without the problem of sliding in the portions gripped with the vibrophore.

The cyclic plasticity dissipated into heat in the RCPZ is estimated from infrared measurements recorded during fatigue crack growth tests conducted at loading frequencies $f \approx 100Hz$. The obtained results agree with a known result found in the literature ([Pippan and Stüwe, 1984] and [Klingbeil, 2003]), that of the fourth power law linking the cyclic plastic dissipation into heat to the applied SIF range. For the resulting computed temperature variation field, it is singular because the model of heat diffusion equation uses a spot heat source. It should be noted that the problem of singularity has not a major consequence since the focus afterward is on the SIF elastic solution calculated outside the zone of singularity (the RCPZ).

Furthermore, as it can be seen in Figure 2.28, even low, the temperature variation field, θ_d, has the same order of magnitude as the temperature variation field, θ_q, assumed generated by the heat source, q. One could notice that during the quantification of the heat source q, the temperature variation field, θ_d, should have been substracted from the temperature variaton measured near the crack tip in order to properly obtain the temperature field associated with only the heat source, q. But it should be reminded that the extrapolation of the heat source, d_1, was rough, and so does its associated temperature field, θ_d. That is why and for simplification, in the following the temperature variation field, θ_q, is considered due to only the heat source, q.

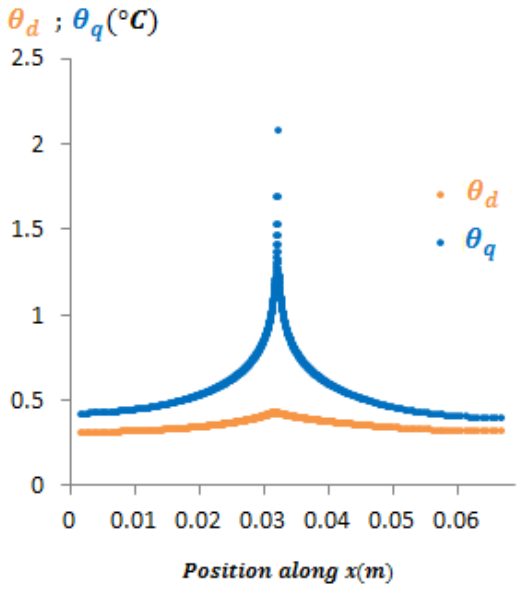

Figure 2.28: Evolution of the temperature variation, $\theta_q(t = 258.4s)$, and the temperature variation, $\theta_d(t = 258.4s)$, along x axis, with the loading configuration: $a = 31.3mm$, $\Delta K_I = 26MPa.\sqrt{m}$, $R = 0.1$, and $f = 98.6Hz$.

Chapter 3

Thermomechanical analysis - Effects of the heat sources on the SIF

Contents

Dans ce troisième chapitre, les effets thermiques quantifiés au deuxième chapitre sont pris en compte dans le calcul du champ des contraintes permettant de calculer le facteur d'intensité des contraintes. Pour ce faire, une décomposition du problème général est proposée dans le cadre de l'hypothèse de linéarité issue de la mécanique élastique linéaire de la rupture. Cette décomposition permet de mettre en évidence la partie mécanique du problème, associée à la sollicitation mécanique cyclique, et sa partie thermomécanique reliant les effets thermiques et leurs champs de contraintes associés.

L'objectif est de résoudre la partie thermomécanique du problème qui permet de calculer la correction thermique du facteur d'intensité des contraintes due à chaque source de chaleur. Avant de présenter ces calculs, la technique utilisée dans ce travail pour calculer le facteur d'intensité des contraintes est expliquée au début du chapitre. Ensuite, la méthodologie détaillant la démarche et les hypothèses nécessaires à la résolution de ce problème est présentée. Les résultats du calcul thermomécanique des contraintes viennent par la suite.

Après avoir résolu le problème thermomécanique, l'effet de chaque source de chaleur, sur le facteur d'intensité des contraintes, est quantifié. L'effet global des trois sources est aussi évalué. De plus, les effets de chaque source de chaleur sur les paramètres de fatigue (l'étendu du facteur d'intensité des contraintes, ses valeurs minimale et maximale ainsi que leur rapport) sont calculés.

A la fin du chapitre, une attention particulière est portée sur l'effet associé à la source de dissipation plastique cyclique en pointe de fissure. Son effet sur la vitesse de propagation de la fissure est calculé.

The third chapter deals with a thermomechanical analysis taking into account the temperature fields computed in the previous chapter, and enabling to compute the stress field leading to calculate the stress intensity factor. For this purpose, the main problem is decomposed, within the hypothesis of the linear elastic fracture mechanics, into two problems, the first one is purely mechanical and related to the mechanical cyclic loading, and the second one is thermomechanical and related to the thermal effects and their associated stresses.

The aim is to solve the thermomechanical part of the problem which enables to compute the thermal correction of the stress intensity factor associated with each thermal effect. Before delving into the results, the technique used in this work to calculate the stress intensity factor is first presented. Afterward, the methodology detailing the approach and the assumptions used to solve the problem is explained and followed by the results of the thermomechanical calculation.

The thermal effect, on the stress intensity factor, of each heat source is quantified. The overall effect of the three heat sources is computed as well. In addition, the effects of the heat sources on the stress intensity factor range, its minimum and maximum values as well as their ratio, are computed.

At the end of this chapter, a special attention is paid to the effect resulting from the cyclic plasticity dissipated into heat at the crack tip. Its effect on the fatigue crack growth rate is calculated.

3.1 Techniques to solve the SIF solution in crack problems involving thermal stresses

It is well established that one of the most effective methods for analyzing cracked structures is the finite element method ([Chan et al., 1970] and [Wilson, 1972]). Indeed, once a finite element solution is obtained, the value of the SIF can be extracted from it. While there are many ways of doing this, one of the sturdiest methods involves the use of the J integral ([Rice, 1968]). This integral is calculated from the finite element solution over any arbitrary path surrounding the crack tip, and from this calculated value, the crack tip SIF can be determined.

In the case of a cracked structure, the J integral for a linear-elastic isotropic material is defined as ([Rice, 1968]):

$$J = \int_{\Gamma} \left(w \mathrm{d}y - \xi_i \frac{\partial u_i}{\partial x} \mathrm{d}s \right), \tag{3.1}$$

where Γ denotes a closed path around the crack tip (Figure 3.1), s is distance along the path, $w = w(x, y) = \int_{\varepsilon} \sigma_{ij} \mathrm{d}\varepsilon_{ij}$ is the strain energy density, $\xi_i = \sigma_{ij} n_i$ and u_i are components of the stress vector and displacement vector, respectively. Moreover, it is assumed that no singularities are enclosed by the path Γ.

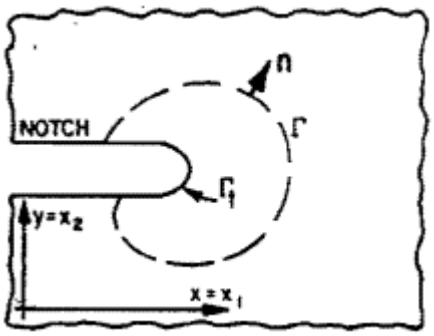

Figure 3.1: Notch in plane deformation field with contour integral Γ, [Rice, 1968].

To prove path independent, [Rice, 1968] transformed the line integral (3.1) into an area integral by using the Green-Gauss theorem:

$$J = \int_{a_0} \left[\frac{\partial w}{\partial x} - \frac{\partial}{\partial x_j} (\sigma_{ij} \frac{\partial u_i}{\partial x}) \right] \mathrm{d}x \mathrm{d}y, \tag{3.2}$$

where a_0 is the area enclosed by the path Γ (Figure 3.1), x_j is for $x_1 = x$ and $x_2 = y$.

By differentiating the strain energy density w,

$$\frac{\partial w}{\partial x} = \frac{\partial w}{\partial \varepsilon_{ij}} . \frac{\partial \varepsilon_{ij}}{\partial x} = \sigma_{ij} \frac{\partial \varepsilon_{ij}}{\partial x} \tag{3.3}$$

$$= \frac{1}{2} \sigma_{ij} \left[\frac{\partial}{\partial x} (\frac{\partial u_i}{\partial x_j}) + \frac{\partial}{\partial x} (\frac{\partial u_j}{\partial x_i}) \right] \tag{3.4}$$

$$= \sigma_{ij} \frac{\partial}{\partial x_j} (\frac{\partial u_i}{\partial x}) \quad (\text{since } \sigma_{ij} = \sigma_{ji}) \tag{3.5}$$

$$= \frac{\partial}{\partial x_j} (\sigma_{ij} \frac{\partial u_i}{\partial x}) \quad (\text{since } \frac{\sigma_{ij}}{x_j} = 0). \tag{3.6}$$

Thus, the integral of Equation (3.2) vanishes identically, and therefore $J = 0$ for any closed path Γ.

From this property of the J integral, the magnitude of the crack tip SIF can be determined by calculating the integral over any path surrounding the crack tip. Considering the closed path $(\Gamma_1 + s_1 + \Gamma_2 + s_2)$ shown in Figure 3.2, it follows that:

$$\int_{\Gamma_1} \square + \int_{s_1} \square + \int_{\Gamma_2} \square + \int_{s_2} \square = 0, \tag{3.7}$$

with $\square = W dy - \xi_i \frac{\partial u_i}{\partial x} \mathrm{d}s$.

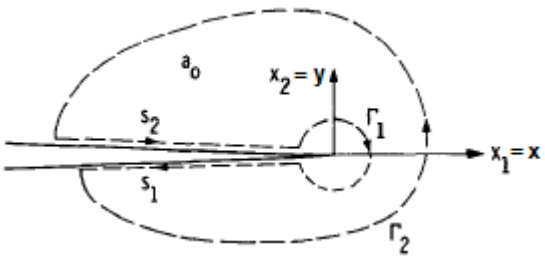

Figure 3.2: Contours for calculating the SIF from the J-line integral, [Wilson and Yu, 1979].

The path Γ_2 is considered to be arbitrary, but the path Γ_1 is chosen circular with radius r_1 about the crack tip where r_1 tends to 0. In the region through which the path Γ_1 passes, the stresses and displacements can be expressed in the form of the classical crack tip equations previously presented in Chapter I (Equations (1.1) and (1.2)) where the magnitude is dependent on the mode I SIF. Thus, the line integration over the path Γ_1, for plane stress condition for instance, results in $\frac{K_I^2}{E}$ under the condition of small scale yielding, [Rice, 1968]. Using this relation and rearranging Equation (3.7) leads to:

$$\frac{K_I^2}{E} = J_{\Gamma_2} - \int_{s_1+s_2} \xi_i \frac{\partial u_i}{\partial x} \mathrm{d}s, \tag{3.8}$$

where J_{Γ_2} represents the value of the J integral over the path Γ_2. Moreover, the fact that $dy = 0$ on s_1 and s_2 is used to obtain Equation (3.8).

As a result, the SIF can be calculated by evaluating the J integral over any path Γ_2 which surrounds the crack tip, by assuming that the tractions ξ_i are null on the crack surfaces between the points where the path Γ_2 meets the crack surfaces and the crack tip. If these tractions are not null, then the right hand integral in Equation (3.8) must be calculated.

Now in the case of thermal stresses generated by thermal expansion due to a temperature variation θ, by assuming the hypothesis of plane stresses and linear-elastic thermoelasticity, along [Rice, 1968]'s development (Equations (3.2) to (3.6)), the J integral is written in this case as ([Wilson and Yu, 1979]):

$$J = \frac{E\alpha}{1-\nu} \int_{a_0} \left[\theta \frac{\partial}{\partial x}(\varepsilon_{ii}) - \frac{1}{2} \frac{\partial}{\partial x}(\theta \varepsilon_{ii}) \right] \mathrm{d}x\mathrm{d}y, \tag{3.9}$$

which is not null because $\theta \frac{\partial}{\partial x}(\varepsilon_{ii}) \neq \frac{1}{2} \frac{\partial}{\partial x}(\theta \varepsilon_{ii})$. Therefore, the value of the J integral over a closed path in the case of thermal stresses is not zero, which leads to conclude that for such problems, the elastic crack tip SIF cannot be directly assessed from the J integral calculation over a path surrounding the crack tip. In fact, a correction of the J integral technique is needed when thermal stresses are present, and this can be done by developing the integrand of Equation (3.9) in order to obtain an alternate formulation satisfying the J-line properties. Such a procedure is unfortunately complicated to implement, but several options may be proposed as simple alternative solutions.

Indeed, beyond what is proposed in the literature to overcome the problem of the J integral in thermal stress crack problems, other integral techniques can be used, namely, the weight function technique ([Bueckner, 1971]) and the Green's functions technique ([Cartwright and Rooke, 1980]). The second one was proven to be simply applicable and gives direct SIF solutions for problems with random complex load configurations.

This integral technique is based on the use of Green's functions, first postulated by Green in 1828 ([Green, 1828]), and defined as the response of a system to a standard input which is usually in the form of an impulse. The important property of these functions is that, when suitably defined, they contain all the essential in-

formation about the system. They can thus be used to obtain the response of the system to any input by considering it as being composed of large numbers of small impulses. The total response is the sum of all the individual responses due to each input impulse acting separately.

[Cartwright and Rooke, 1980] applied this concept to fracture mechanics in order to calculate the SIF for different cases of loaded cracks. Indeed, for a linear-elastic cracked body submitted to a force P acting at a point in the body, the SIF at the crack tip which arises in response to the point force may be considered as a special case of a Green's function. For the example of crack loaded with a point force P (Figure 3.3), the mode I SIF is:

$$K_I = \frac{P}{\sqrt{\pi a}} \left[\frac{a + x_0}{a - x_0}\right]^{\frac{1}{2}} = \frac{P}{\sqrt{\pi a}} G(x_0), \tag{3.10}$$

where x_0 is the distance of the point of application of the force from the centre of the crack, and $G(x_0) = \left[\frac{a+x_0}{a-x_0}\right]^{\frac{1}{2}}$ denotes the Green's function for this case.

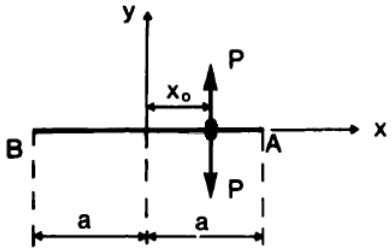

Figure 3.3: Crack loaded with a point force P, [Cartwright and Rooke, 1980].

If a pressure $p(x)$, with $-a \leq x \leq a$, acts normal to the crack faces, the SIF is given by:

$$K_I = \frac{1}{\sqrt{\pi a}} \int_{-a}^{a} p(x) G(x) \mathrm{d}x. \tag{3.11}$$

For the case of $p(x) = p$ (a constant), Equation (3.11) gives the well known result, $K_I = p\sqrt{\pi a}$, which corresponds to the case of an infinite center-cracked sheet whose crack of length, $2a$, is subjected to a constant-uniform load p.

In general, to obtain the opening mode SIF for elastic cracked bodies subjected to "arbitrary" forces, the problem can be simplified by using Bueckner's decomposition method, [Bueckner, 1958]. Bueckner's result is that the SIF for a crack in an elastic body subjected to external forces is identical to that for a similar crack, subjected to internal pressure in a similar body which has no external forces acting on it. The

internal pressure $p(x)$ acting in the crack is equal to the stress that would exist normal to the crack line along the crack site in the uncracked body subjected to external forces. This principle is illustrated in Figure 3.4.

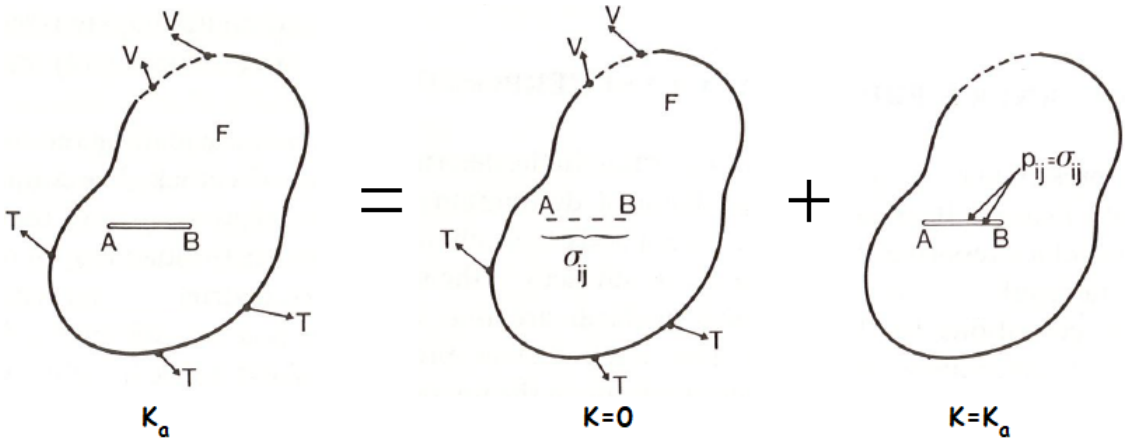

Figure 3.4: Schematic illustration of Bueckner's principle with an elastic body subjected to arbitrary forces, F, boundary tractions, T, and boundary displacements V. This figure is reproduced from [Cartwright, 1979].

Therefore, Bueckner's principle is a common and simple technique used for obtaining SIF when complex loading configurations are considered. The determination of the SIF using Green's functions usually involves the use of Bueckner's principle and always involves evaluating an integral of the form of Equation (3.11). Moreover, detailed knowledge about the type of cracked structures (structures with edge cracks, embedded cracks, or cracks emanating from holes) is required in order to use the correct Green's function since many of them are available in [Cartwright and Rooke, 1980] for example. For the crack problem studied in this work, the Green's function adapted to the problem is:

$$G(x) = \sqrt{\frac{a^2}{a^2 - x^2}}, \tag{3.12}$$

which is used in the integral of Equation (3.11). This is the integral technique used in this work in order to calculate the thermal corrections of the SIF by taking into account the effects of the computed temperature fields.

3.2 Methodology and assumptions for computing the thermal corrections of the SIF

During classical fatigue crack growth tests at room temperature, the mode I fatigue crack propagation is governed by the SIF $K_I(t)$, the SIF range ΔK_I, and the load ratio R. The applied mechanical cyclic loading generates a cyclic stress field in the CCT specimen. But, as the thermal effects take place due to the three types of heat sources, previously presented and quantified in Chapter II, the thermal expansion of the material modifies this cyclic stress field. As a result, a thermal correction of the SIF needs to be calculated as introduced before at the end of Chapter I. To highlight this thermal correction, denoted afterward by $K_{I_{temp}}(t)$, the main physical problem, where the mechanical and thermal effects are coupled, can be decomposed into two problems within the LEFM and the hypothesis assuming the absence of crack closure phenomena. This decomposition is illustrated in Figure 3.5.

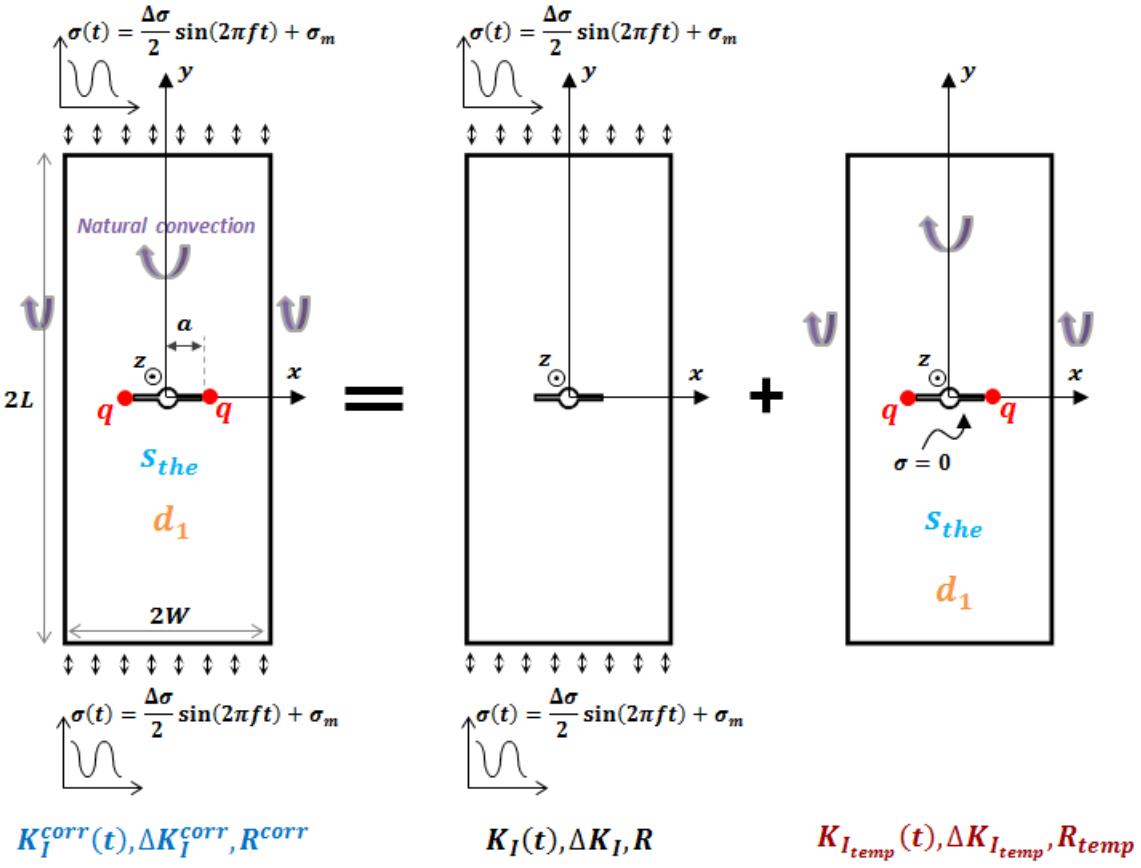

Figure 3.5: Decomposition of the main problem.

The first sub-problem of this decomposition is purely mechanical. Under the applied sinusoidal loading, the associated SIF, $K_I(t)$, can be written as:

$$K_I(t) = \frac{\Delta K_I}{2}\sin(2\pi f t) + K_I^m, \tag{3.13}$$

$$K_I^m = \frac{\Delta K_I}{2}\frac{1+R}{1-R}, \tag{3.14}$$

where f is the loading frequency, t is time, and K_I^m is the mean value of the mode I SIF $K_I(t)$.

The second sub-problem of the decomposition above is a thermomechanical problem. It is related to the thermomechanical effects due to the heat sources, s_{the}, d_1 and q. Each of the three heat sources generates a temperature variation field which contributes to the thermal expansion of the material, and consequently creates an associated thermal stress field according to the linearity assumption of the LEFM. Thus, three types of thermal stress fields induce three types of thermal corrections on the SIF: $K_{I_{temp}}^{the}$, $K_{I_{temp}}^{d}$, and $K_{I_{temp}}^{q}$, respectively associated with the effects of the heat sources s_{the}, d_1, and q.

The superposition principle of the LEFM enables to write the SIF of the main problem, K_I^{corr}, corrected by taking into account the three thermal corrections:

$$K_I^{corr}(t) = K_I(t) + K_{I_{temp}}(t), \tag{3.15}$$

$$K_{I_{temp}}(t) = K_{I_{temp}}^{the}(t) + K_{I_{temp}}^{d}(t) + K_{I_{temp}}^{q}(t). \tag{3.16}$$

The thermal correction of the SIF, $K_{I_{temp}}(t)$, is calculated by using the integral technique using Green's function presented in the previous section. As a result:

$$K_{I_{temp}}(t) = 2\sqrt{\frac{a}{\pi}}\int_0^a \frac{\sigma_{yy}(x,0,t)}{\sqrt{a^2-x^2}}\mathrm{d}x, \tag{3.17}$$

with $\sigma_{yy}(x,0,t)$ is defined as the normal stress field toward y axis generated by thermal expansion such that the condition of uncracked body is applied. That is why, the thermomechanical sub-problem on the right in Figure 3.5 is decomposed, within the LEFM and the assumption of no crack closure, into two additional sub-problems satisfying the superposition principle (Figure 3.6). For simplifying the notation, $\sigma_{yy}(x,0,t)$ is denoted by $\sigma_{yy}(x,t)$ in the following.

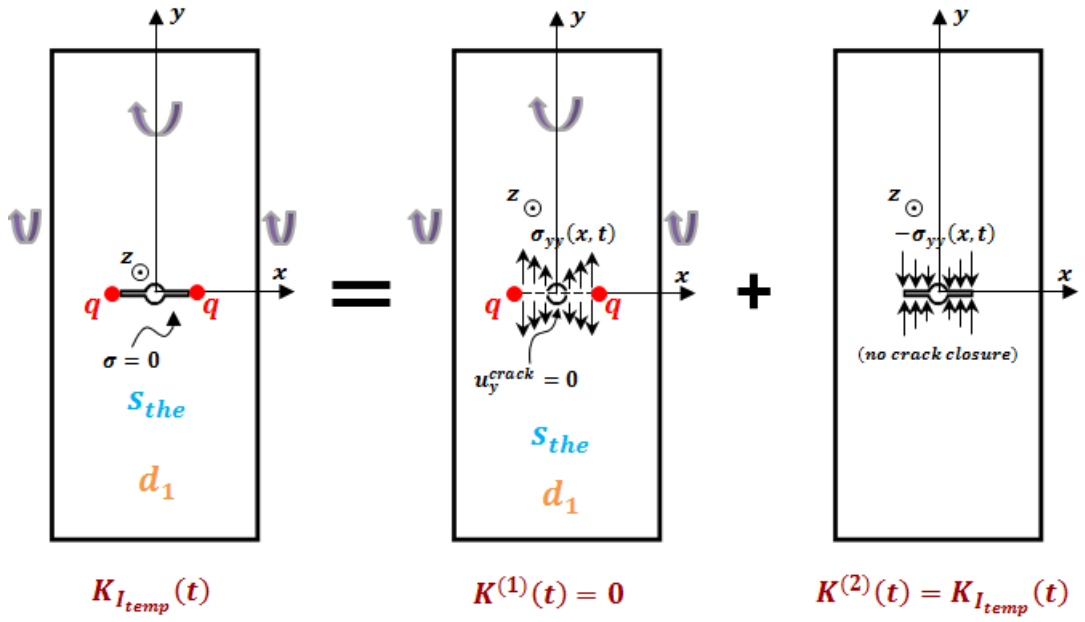

Figure 3.6: Decomposition of the thermomechanical problem.

The condition of uncracked body is illustrated in the first sub-problem of Figure 3.6. Then, in order to compute, $\sigma_{yy}(x,t)$, this sub-problem is solved by FEA. The boundary condition applied over the RCPZ contour is a null radial stress as proposed by [Ranc et al., 2014]. Indeed, with alternating cyclic plasticity in the RCPZ, the mean stress tends to zero. However, it should be noted that, under the small scale yielding condition, applying this RCPZ boundary condition, or considering only elasticity in the whole domain, both give very close stress solutions and have very negligible impact on the elastic crack tip SIF.

For the sake of simplification, the RCPZ is modeled in these calculations by a disc for the three types of thermal effects, with the diameter previously given by the estimation of Irwin's model under the plane stress hypothesis (Equation (1.9), Chapter I).

As a result, $\sigma_{yy}(x,t)$ is known and the thermal correction of the SIF, $K_{I_{temp}}(t)$, can be computed according to Equation (3.17). It should be pointed out that the integrand in Equation (3.17) is defined for $x \in [0, a]$ as shown in Figure 3.7. Moreover, the factor of two outside the integral accounts for the use of a half crack model because of symmetries.

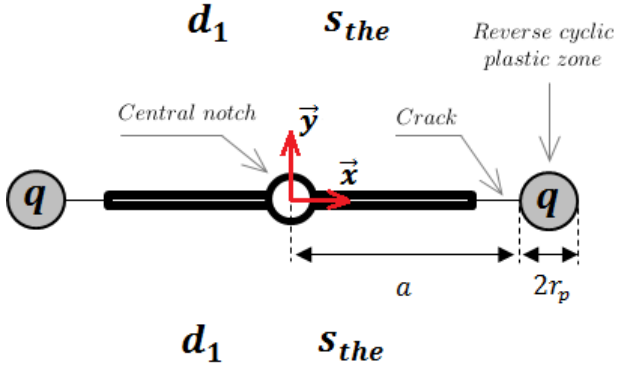

Figure 3.7: A schematic fatigue crack model showing the position of the abscissas x used in Equation (3.17).

This methodology is used to calculate the three components of the thermal correction of the SIF, $K^{the}_{I_{temp}}$, $K^{d}_{I_{temp}}$, and $K^{q}_{I_{temp}}$.

3.3 Thermomechanical problem

Solving the thermomechanical problem consists in computing, by FEA with the condition of uncracked body, the three normal stress fields, σ^{the}_{yy}, σ^{d}_{yy} and σ^{q}_{yy}, respectively generated by the thermal expansion of the material due to the temperature variation fields, θ_{the}, θ_d and θ_q. For this purpose, the first sub-problem of the decomposition of Figure 3.6 is solved by considering a two-dimensional linear, isotropic, and thermoelastic material behavior law:

$$\bar{\bar{\sigma}}(x,y,t) = \bar{\bar{\bar{\bar{C}}}} : (\bar{\bar{\varepsilon}}(x,y,t) - \bar{\bar{\varepsilon}}_{th}(x,y,t)), \tag{3.18}$$

$$\bar{\bar{\varepsilon}}_{th} = \alpha.\theta.\bar{\bar{1}}, \tag{3.19}$$

where $\bar{\bar{\varepsilon}}_{th}$ is the strain resulting from thermal expansion.

As mentioned earlier, the hypothesis of plane stress is considered. In this case, the two-dimensional linear thermoelastic behavior law is written as:

$$\begin{pmatrix} \sigma_{xx}(x,y,t) \\ \sigma_{yy}(x,y,t) \\ \tau_{xy}(x,y,t) \end{pmatrix} = \frac{E}{1-\nu^2} \begin{pmatrix} 1 & \nu & 0 \\ \nu & 1 & 0 \\ 0 & 0 & \frac{1-\nu}{2} \end{pmatrix} \begin{pmatrix} \varepsilon_{xx}(x,y,t) \\ \varepsilon_{yy}(x,y,t) \\ 2\varepsilon_{xy}(x,y,t) \end{pmatrix} - \frac{E\alpha}{1-\nu}\theta(x,y,t) \begin{pmatrix} 1 \\ 1 \\ 0 \end{pmatrix}. \tag{3.20}$$

It must be known that, besides the boundary conditions of symmetries in the two-dimensional quarter model as well as the boundary condition of a null radial stress

applied around the RCPZ, solving the first sub-problem of Figure 3.6 involves one additional boundary condition, that of considering the crack absent, which implies a null normal displacement over the crack (Figure 3.8).

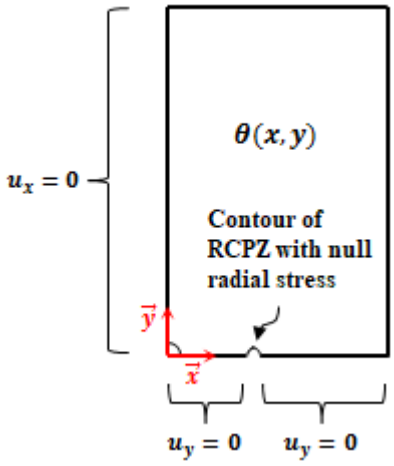

Figure 3.8: Boundary conditions to solve the thermomechanical problem.

The example of loading configuration used in the previous chapter to compute the temperature variation fields, θ_{the}, θ_d, and θ_q, is used in the following for highlighting the calculation of the stress fields, σ_{yy}^{the}, σ_{yy}^{d}, and σ_{yy}^{q}. It is a quarter model of the CCT specimen with a crack length, $a = 31.3mm$, under an applied SIF range, $\Delta K_I = 26MPa.\sqrt{m}$, which is equivalent to an applied normal stress amplitude, $\frac{\Delta\sigma}{2} = 44.6MPa$. The reference temperature is, $T_0 = 20°C$, the loading frequency is, $f = 98.6Hz$, the load ratio is, $R = 0.1$, and the fatigue test duration is, $\Delta t = 258.4s$. As a reminder, this loading configuration corresponds to the fatigue crack growth test $T015$ carried out to estimate the heat source q (*cf.* Table 2.4, Chapter II).

Furthermore, it should be noted that the calculation of the normal stress fields, σ_{yy}^{the}, σ_{yy}^{d}, and σ_{yy}^{q}, do not take into account the dynamic effect. In other words, the assumption of static calculation is considered.

The thermoelastic stress field, σ_{yy}^{the}, is sinusoidal as the thermoelastic temperature variation field, θ_{the}. Moreover, it is in phase with θ_{the} according to the classical law of linear thermoelasticity (Equation (3.20)). As a consequence, σ_{yy}^{the} is out of phase with the stress response due to mechanical loading. σ_{yy}^{the} can then be written as:

$$\sigma_{yy}^{the}(x, y, t) = \sigma_{the}^{a}(x, y).\sin(2\pi ft + \varphi(x, y)), \tag{3.21}$$

where σ_{the}^{a} denotes the amplitude of the normal stress field related to the thermoelastic effect.

Since the temperature variation fields, θ_d, and θ_q, are computed in the transient regime and determined at $t = 258.4s$ (the end of the fatigue test), the resulting stress fields σ^d_{yy} and σ^q_{yy} are also computed at $t = 258.4s$.

It should be mentioned that contrary to, σ^{the}_a, which is an amplitude since it is calculated from the thermal expansion generated by the amplitude of the thermoelastic temperature variation field, θ^a_{the}, the normal stress fields, σ^d_{yy} and σ^q_{yy}, are mean stresses generated by the thermal expansion related to the temperature variation fields, θ_d and θ_q, respectively.

Figure 3.9 plots the evolution over x axis of σ^{the}_a, $\sigma^d_{yy}(t = 258.4s)$ and $\sigma^q_{yy}(t = 258.4s)$.

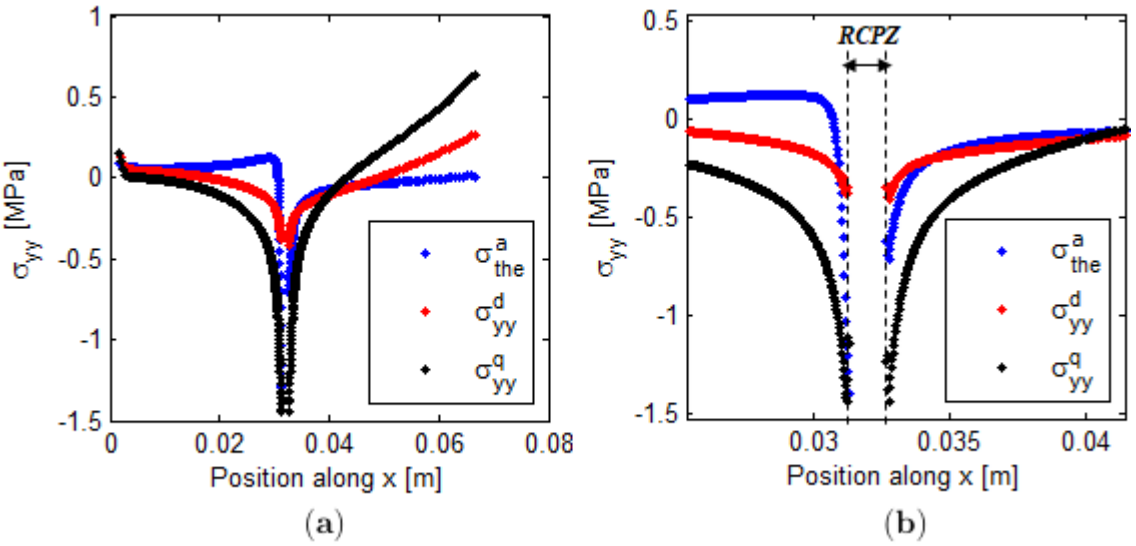

Figure 3.9: (a) Evolution of the normal stress fields, σ^{the}_a, $\sigma^d_{yy}(t = 258.4s)$, and $\sigma^q_{yy}(t = 258.4s)$, along x axis for the loading configuration: $a = 31.3mm$, $\Delta K_I = 26MPa.\sqrt{m}$, $R = 0.1$, $f = 98.6Hz$. (b) Zoom near the RCPZ.

In Figure 3.9, it can be observed that the three normal stress fields are heterogeneous and compressive near the crack tip. Moreover, near the RCPZ, the normal stress field associated with the heat source q, σ^q_{yy}, is more compressive than the normal stress field associated with the intrinsic dissipation due to microplasticity, σ^d_{yy}. This is normal because in the same region the temperature variation field, θ_q, is greater than the temperature variation field, θ_d, which means that the thermal expansion generated by the heat source, q, is the most intense.

Furthermore, the fact that the computed stress fields, σ^a_{the}, σ^d_{yy}, and σ^q_{yy}, are negative means that they contribute to reduce the mechanical stress response generated by the applied mechanical loading. Indeed, the thermoelastic stress amplitude field,

σ_a^{the}, decreases the stress response resulting from the applied stress amplitude ($\frac{\Delta\sigma}{2} = 44.6MPa$ in this example), and the mean stress fields, σ_{yy}^d and σ_{yy}^q, decrease the mean stress response due to the applied mean stress ($\sigma^m = \frac{\Delta\sigma}{2}\left(\frac{1+R}{1-R}\right) = 54.5MPa$ in this example).

3.4 Computing the thermal corrections of the SIF

Having computed the stress fields, σ_{the}^a, σ_{yy}^d, and σ_{yy}^q, the three components of the thermal correction of the SIF, $K_{I_{temp}}^{the}$, $K_{I_{temp}}^d$, and $K_{I_{temp}}^q$, are hereinafter computed.

3.4.1 Consequence of the thermoelastic source on the SIF

The thermoelastic part of the thermal correction of the SIF, $K_{I_{temp}}^{the}(t)$, is expressed according to Equation (3.17) as follows:

$$K_{I_{temp}}^{the}(t) = 2\sqrt{\frac{a}{\pi}}\int_0^a \frac{\sigma_{yy}^{the}(x,t)}{\sqrt{a^2-x^2}}\mathrm{d}x, \tag{3.22}$$

where $\sigma_{yy}^{the}(x,t)$ is defined by Equation (3.21). Since $\sigma_{yy}^{the}(x,t)$ is sinusoidal, it can be represented by the complex formula:

$$\sigma_{yy}^{the}(x,t) = \sigma_{the}^a(x).e^{j(2\pi ft+\varphi(x))}, \tag{3.23}$$

which enables to write Equation (3.22) in a complex form as follows:

$$K_{I_{temp}}^{the}(t) = 2\sqrt{\frac{a}{\pi}}\int_0^a \frac{\sigma_{the}^a(x).e^{j(2\pi ft+\varphi(x))}}{\sqrt{a^2-x^2}}\mathrm{d}x, \tag{3.24}$$

The complex equation (3.24) enables to simplify and write Equation (3.22) as a sinusoidal function defined as follows:

$$K_{I_{temp}}^{the}(t) = \frac{\Delta K_{I_{temp}}^{the}}{2}\sin(2\pi ft+\phi), \tag{3.25}$$

such that:

$$\frac{\Delta K_{I_{temp}}^{the}}{2} = 2\sqrt{\frac{a}{\pi}} \left| \int_0^a \frac{\sigma_{the}^a(x).e^{j\varphi(x)}}{\sqrt{a^2-x^2}} \mathrm{d}x \right|, \tag{3.26}$$

$$\phi = \arg\left(\int_0^a \frac{\sigma_{the}^a(x).e^{j(\varphi(x))}}{\sqrt{a^2-x^2}} \mathrm{d}x \right), \tag{3.27}$$

where $\frac{\Delta K_{I_{temp}}^{the}}{2}$ is the amplitude of $K_{I_{temp}}^{the}(t)$, and ϕ is the phase shift between $K_{I_{temp}}^{the}(t)$ and the SIF associated with the mechanical response, $K_I(t)$. Therefore, $\Delta K_{I_{temp}}^{the}$ and ϕ, are calculated from the previously computed $\sigma_{the}^a(x)$ and $\varphi(x)$. That numerically gives, $\Delta K_{I_{temp}}^{the} = 0.084 MPa.\sqrt{m}$, and $\phi = 0.013 rad$.

As a consequence, the thermoelastic coupling effect on the SIF can be expressed as follows:

$$K_I^{corr,the}(t) = K_I(t) + K_{I_{temp}}^{the}(t), \tag{3.28}$$

$$= \frac{\Delta K_I}{2}\sin(2\pi ft) + K_I^m + \frac{\Delta K_{I_{temp}}^{the}}{2}\sin(2\pi ft + \phi), \tag{3.29}$$

where $K_I^{corr,the}$ is the SIF corrected by taking into account the thermoelastic coupling effect. To simplify the sinusoidal form of Equation (3.29), the technique of complex variables is used:

$$K_I^{corr,the}(t) = \frac{\Delta K_I}{2}.e^{j(2\pi ft)} + K_I^m + \frac{\Delta K_{I_{temp}}^{the}}{2}.e^{j(2\pi ft+\phi)}, \tag{3.30}$$

$$= (\frac{\Delta K_I}{2} + \frac{\Delta K_{I_{temp}}^{the}}{2}.e^{j\phi}).e^{j(2\pi ft)} + K_I^m. \tag{3.31}$$

Equation (3.31) can then be rewritten in the real sinusoidal form as:

$$K_I^{corr,the}(t) = \frac{\Delta K_I^{corr,the}}{2}\sin(2\pi ft + \psi) + K_I^m. \tag{3.32}$$

such that :

$$\frac{\Delta K_I^{corr,the}}{2} = \left| \frac{\Delta K_I}{2} + \frac{\Delta K_{I_{temp}}^{the}}{2}.e^{j\phi} \right|, \tag{3.33}$$

$$\psi = arg\left(\frac{\Delta K_I}{2} + \frac{\Delta K_{I_{temp}}^{the}}{2}.e^{j\phi} \right), \tag{3.34}$$

which numerically gives, $\Delta K_I^{corr,the} = 26.08 MPa.\sqrt{m}$, and $\psi = 0$.

As a result, the thermoelastic effect slightly increases the SIF range of $K_I(t)$, initially $\Delta K_I = 26MPa.\sqrt{m}$, by 0.31%, and creates no phase shift with the mechanical response. Furthermore, this small change in the amplitude of $K_I(t)$ due to the thermoelastic effect, leads to modify the minimum and maximum values of $K_I(t)$, and consequently modifies the load ratio R near the crack tip. This is presented and discussed apart in Section §3.5.

3.4.2 Consequence on the SIF of the intrinsic dissipation due to microplasticity

For the effect resulting from the intrinsic dissipation due to microplasticity, d_1, according to Equation (3.17), the associated normal stress field, σ^d_{yy}, enables to calculate the thermal correction of the SIF, $K^d_{I_{temp}}$. The normal stress field, $\sigma^d_{yy}(t = 258.4s)$, previously computed (Figure 3.9), enables to calculate the associated thermal correction on the SIF: $K^d_{I_{temp}}(t = 258.4s) = -0.022MPa.\sqrt{m}$. It is negative because of the compressive stress field due to the part of thermal expansion induced by the intrinsic dissipation due to microplasticity. Moreover, it is very small compared to K^m_I for instance which is equal to $15.88MPa.\sqrt{m}$ for this example of loading configuration. For simplifying the analysis afterward and since $K^d_{I_{temp}}(t = 258.4s)$ is small, it is considered as time-independent during the duration of the applied fatigue test. As a result, the SIF corrected after considering the effect of the heat source, d_1, can be written as:

$$K^{corr,d}_I(t) = K_I(t) + K^d_{I_{temp}}, \tag{3.35}$$

$$= \frac{\Delta K_I}{2}\sin(2\pi ft) + K^m_I + K^d_{I_{temp}}. \tag{3.36}$$

The intrinsic dissipation due to microplasticity consequently affects the SIF by decreasing its mean value K^m_I as well as its minimum and maximum values, even though this decrease remains small. Moreover, it has no effect on the SIF range, ΔK_I.

3.4.3 The effect on the SIF of cyclic plasticity dissipated into heat in the RCPZ

For the cyclic plasticity dissipated into heat in the RCPZ, q, the associated thermal correction of the SIF, $K^q_{I_{th}}$, is calculated from σ^q_{yy}, by using Equation (3.17). For example, the computed normal stress field, $\sigma^q_{yy}(t = 258.4s)$, previously plotted in Figure 3.9, $K^q_{I_{th}}(t = 258.4s) = -0.091MPa.\sqrt{m}$, which is negative like $K^d_{I_{th}}$ because of the compressive stress field resulting from the associated thermal expansion. It is also small compared to the value of the mean SIF associated with this loading configuration ($K^m_I = 15.88MPa.\sqrt{m}$). Subsequently, the assumption of considering a constant value of $K^q_{I_{th}}$ is considered during the applied fatigue test for simplification.

Therefore, the thermal effect related to the heat source, q, modifies the SIF as:

$$K^{corr,q}_I(t) = K_I(t) + K^q_{I_{temp}}, \tag{3.37}$$

$$= \frac{\Delta K_I}{2}\sin(2\pi ft) + K^m_I + K^q_{I_{temp}}. \tag{3.38}$$

Thus, according to Equation (3.38), the heat source, q, modifies the SIF by decreasing its minimum, maximum and mean values, whereas ΔK_I is not impacted.

3.4.4 Comparison of the three thermal effects on the SIF through the applied fatigue crack growth tests

By applying the same calculation methodology with the loading configurations of the fatigue crack growth tests which are carried out to estimate the heat source, q, and fulfill the conditions of the LEFM (*i.e.* fatigue tests $T0XY$ listed in Table 2.4, Chapter II), the three types of thermal corrections on the SIF are quantified and summarized in Table 3.1.

$Test$	R	ΔK_I	K_I^m	$K_{I_{min}}$	$K_{I_{max}}$	$\Delta K_I^{corr,the}$	$\psi(rad)$	$K^d_{I_{temp}}$	$K^q_{I_{temp}}$
$T011$	0.1	13	7.94	1.44	14.44	13.04	0	0.001	-0.04
$T012$	0.1	16	9.77	1.77	17.77	16.04	0	0.002	-0.033
$T013$	0.1	20	12.22	2.22	22.22	20.06	0	-0.006	-0.051
$T014$	0.1	23	14.05	2.55	25.55	23.06	0	-0.012	-0.064
$T015$	0.1	26	15.88	2.88	28.88	26.08	0	-0.022	-0.091
$T041$	0.4	13	15.16	8.66	21.66	13.04	0	-0.002	-0.04
$T042$	0.4	16	18.66	10.66	26.66	16.02	0	-0.04	-0.04
$T061$	0.6	13	26	19.5	32.5	13.04	0	$\oslash$	-0.05

Table 3.1: Components of the main SIF, expressed in $MPa.\sqrt{m}$, according to the conditions of the applied load blocks of fatigue crack growth tests $T0XY$ (*cf.* Table 2.4, Chapter II).

From Table 3.1, it can be read that the order of magnitude of the computed thermal corrections of the SIF, for all the fatigue crack growth tests carried out in this work, is very small compared to that of the parameters of the SIF related to the mechanical loading (ΔK_I, K_I^m, $K_{I_{min}}$, and $K_{I_{max}}$). Even small, the thermal correction, $K^q_{I_{temp}}$, due to the cyclic plasticity dissipated into heat in the RCPZ, is more substantial in comparison with the thermal corrections resulting from the thermoelastic source and the intrinsic dissipation due to microplasticity.

It should be mentioned that, for the applied load block of the fatigue crack growth test $T061$, $K^d_{I_{temp}}$ was not determined since the intrinsic dissipation due to microplasticity, d_1, was not assessed under the applied load ratio $R = 0.6$ (*cf.* Section §2.4.2, Chapter II).

In the following, the consequences of these thermal corrections on the fatigue crack parameters, ΔK_I, $K_{I_{min}}$, $K_{I_{max}}$, and the R-ratio, are presented.

3.5 Consequences of the heat sources on the fatigue crack parameters

In order to well understand the consequences behind the numerical values of the computed thermal corrections on the SIF (Table 3.1) and to quantify their impact,

the relative corrections associated with: the SIF range, ΔK_I, the minimum and maximum values of the SIF, $K_{I_{min}}$ and $K_{I_{max}}$, and the load ratio near the crack tip, R, are calculated. Hereinafter, Table 3.2 presents these relative corrections, assessed for the three types of heat sources, with the following notations:

- χ_Δ denotes the relative correction associated with the SIF range, ΔK_I. As shown above, only the thermoelastic source affects the SIF range by defining the corrected range, $\Delta K_I^{corr,the}$ (Equation (3.32)). χ_Δ is null for the dissipative heat sources, d_1 and q, as they do not modify the SIF range. It is therefore calculated for the thermoelastic source, s_{the}, such that:

$$\chi_\Delta = \frac{\Delta K_I^{corr,the} - \Delta K_I}{\Delta K_I}. \tag{3.39}$$

- χ_{min} denotes the relative correction associated with, $K_{I_{min}}$, such that:
  - For the thermoelastic source s_{the}:

$$\chi_{min} = \frac{K_{I_{min}}^{corr,the} - K_{I_{min}}}{K_{I_{min}}}, \tag{3.40}$$

    where $K_{I_{min}}^{corr,the} = -\frac{\Delta K_I^{corr,the}}{2} + K_I^m$, which is the minimum value of the thermal correction $K_I^{corr,the}(t)$ (Equation (3.32)).
  - For the intrinsic dissipation d_1:

$$\chi_{min} = \frac{K_{I_{min}}^{corr,d} - K_{I_{min}}}{K_{I_{min}}}, \tag{3.41}$$

    where $K_{I_{min}}^{corr,d} = -\frac{\Delta K_I}{2} + K_I^m + K_{I_{temp}}^d$, which is the minimum value of the thermal correction $K_I^{corr,d}(t)$ (Equation (3.36)).
  - For the heat source q:

$$\chi_{min} = \frac{K_{I_{min}}^{corr,q} - K_{I_{min}}}{K_{I_{min}}}, \tag{3.42}$$

    where $K_{I_{min}}^{corr,q} = -\frac{\Delta K_I}{2} + K_I^m + K_{I_{temp}}^q$, which is the minimum value of the thermal correction $K_I^{corr,q}(t)$ (Equation (3.38)).
- χ_{max} denotes the relative correction associated with, $K_{I_{max}}$, such that:

$$\chi_{max} = \frac{K_{I_{max}}^{corr} - K_{I_{max}}}{K_{I_{max}}}, \tag{3.43}$$

where $K_{I_{max}}^{corr}$ is separately defined for the three heat sources along the same lines as $K_{I_{min}}^{corr}$ above.

- Finally, χ_R denotes the relative correction associated with the R-ratio near the crack tip, such that:

$$\chi_R = \frac{R^{corr,*} - R}{R}, \tag{3.44}$$

with $R^{corr,*}$ is the corrected R-ratio calculated for each heat source:

- For the thermoelastic source, s_{the}, and according to Equation (3.32):

$$R^{corr,the} = \frac{K_{I_{min}}^{corr,the}}{K_{I_{max}}^{corr,the}} = \frac{-\frac{\Delta K_I^{corr,the}}{2} + K_I^m}{\frac{\Delta K_I^{corr,the}}{2} + K_I^m}. \tag{3.45}$$

- For the intrinsic dissipation, d_1, and according to Equation (3.36):

$$R^{corr,d} = \frac{K_{I_{min}}^{corr,d}}{K_{I_{max}}^{corr,d}} = \frac{K_{I_{min}} + K_{I_{temp}}^d}{K_{I_{max}} + K_{I_{temp}}^d}. \tag{3.46}$$

- For the heat source, q, and according to Equation (3.38):

$$R^{corr,q} = \frac{K_{I_{min}}^{corr,q}}{K_{I_{max}}^{corr,q}} = \frac{K_{I_{min}} + K_{I_{temp}}^q}{K_{I_{max}} + K_{I_{temp}}^q}. \tag{3.47}$$

	s_{the}				d_1			q		
$Test$	χ_Δ	χ_{min}	χ_{max}	χ_R	χ_{min}	χ_{max}	χ_R	χ_{min}	χ_{max}	χ_R
$T011$	0.31	−1.39	0.14	−1.80	0.07	0.01	−0.21	−2.78	−0.28	−2.78
$T012$	0.25	−1.13	0.11	−1.63	0.11	0.01	−0.29	−1.86	−0.19	−2.07
$T013$	0.30	−1.35	0.14	−1.57	−0.27	−0.03	−0.33	−2.30	−0.23	−2.16
$T014$	0.26	−1.18	0.12	−1.49	−0.47	−0.05	−0.62	−2.51	−0.25	−2.46
$T015$	0.31	−1.39	0.14	−1.80	−0.76	−0.08	−0.96	−3.16	−0.32	−3.12
$T041$	0.31	−0.23	0.09	−0.37	−0.02	−0.01	−0.06	−0.46	−0.18	−0.32
$T042$	0.25	−0.19	0.08	−0.30	−0.08	−0.03	−0.09	−0.38	−0.15	−0.26
$T061$	0.31	−0.10	0.06	−0.16	⊘	⊘	⊘	−0.26	−0.15	−0.10

Table 3.2: Relative corrections (%) due to the three types of thermal effects.

In Table 3.2, negative relative corrections mean that the corresponding heat source leads to decrease the associated quantity, while positive values mean the opposite. It can be read that the effect of the thermoelastic source tends to slightly increase the SIF range as well as its maximum value, while it contributes to decrease the SIF minimum value and the R-ratio near the crack tip. This effect remains small and has almost the same impact over all the applied load blocks of fatigue crack growth tests. Moreover, the effect of the thermoelastic source on the minimum and maximum values of the SIF, as well as the R-ratio, is lower compared to that of the heat source, q, which has the greatest decreasing impact on these parameters. Furthermore, for the same applied R-ratio, $R = 0.1$ for instance (from fatigue test $T012$ to fatigue test $T015$), the consequences of the heat source, q, manifest as follows: the larger the applied SIF range, ΔK_I, the greater the consequence of decreasing the parameters $K_{I_{min}}$, $K_{I_{max}}$, and R. The fatigue test $T011$ is excluded from this last statement since the corresponding heat source q was estimated with a startling result (*cf.* Figure 2.24, Section §2.4.3 in Chapter II). The effects related to the intrinsic dissipation due to microplasticity, d_1, are minimal and can be neglected compared to those of the heat sources, s_{the} and q.

Moreover, increasing the applied R-ratio for the same applied ΔK_I, *i.e.* fatigue tests $T012$ and $T042$, which amounts to increase the applied mean stress, considerably reduces the consequences, of the three types of heat sources, on the fatigue crack parameters, particularly on the R-ratio near the crack tip.

Having separately quantified the effects of the three types of heat sources on the SIF, it is now reasonable and important to investigate their "total impact" on the SIF since they jointly occur during fatigue crack growth tests. Accordingly, summing the three thermal effects leads to write the SIF of the main problem (as introduced earlier in Section §3.2 of this chapter):

$$K_I^{corr}(t) = K_I(t) + K_{I_{temp}}^{the}(t) + K_{I_{temp}}^{d} + K_{I_{temp}}^{q}, \tag{3.48}$$

$$= \frac{\Delta K_I^{corr,the}}{2} \sin(2\pi f t + \psi) + K_I^m + K_{I_{temp}}^{d} + K_{I_{temp}}^{q}. \tag{3.49}$$

Equation (3.49) shows that the amplitude (and then the range) of the corrected SIF is indeed modified because of the thermoelastic coupling effect, while the thermal corrections due to the dissipative heat sources, d_1 and q, do impact the mean SIF, K_I^m, and consequently its minimum and maximum values, as well as the R-ratio near the crack tip.

From Equation (3.49), the total effect on the minimum and maximum values of

the SIF is expressed as:

$$K_{I_{min}}^{corr} = -\frac{\Delta K_I^{corr,the}}{2} + K_I^m + K_{I_{temp}}^d + K_{I_{temp}}^q, \tag{3.50}$$

$$K_{I_{max}}^{corr} = \frac{\Delta K_I^{corr,the}}{2} + K_I^m + K_{I_{temp}}^d + K_{I_{temp}}^q. \tag{3.51}$$

As a result, the total effect on the R-ratio near the crack tip is:

$$R^{corr} = \frac{K_{I_{min}}^{corr}}{K_{I_{max}}^{corr}}, \tag{3.52}$$

$$= \frac{-\frac{\Delta K_I^{corr,the}}{2} + K_I^m + K_{I_{temp}}^d + K_{I_{temp}}^q}{\frac{\Delta K_I^{corr,the}}{2} + K_I^m + K_{I_{temp}}^d + K_{I_{temp}}^q}. \tag{3.53}$$

Table 3.3 lists the calculation of the corrected minimum and maximum values of the SIF, $K_{I_{min}}^{corr}$ and $K_{I_{max}}^{corr}$, and the corrected R-ratio near the crack tip, R^{corr}, after taking into account the total effect resulting from the three types of heat sources. To see how much these fatigue crack parameters are impacted, three relative corrections are calculated and also presented in Table 3.3. That concerns, $\delta_{min} = \frac{K_{I_{min}}^{corr} - K_{I_{min}}}{K_{I_{min}}}$, which denotes the relative correction on $K_{I_{min}}$, $\delta_{max} = \frac{K_{I_{max}}^{corr} - K_{I_{max}}}{K_{I_{max}}}$, which denotes the relative correction on $K_{I_{max}}$, and $\delta_R = \frac{R^{corr} - R}{R}$ denoting the relative correction on the R-ratio near the crack tip.

$Test$	R	ΔK_I	$K_{I_{min}}$	$K_{I_{max}}$	$K_{I_{min}}^{corr}$	$K_{I_{max}}^{corr}$	R^{corr}	$\delta_{min}(\%)$	$\delta_{max}(\%)$	$\delta_R(\%)$
$T011$	0.1	13	1.44	14.44	1.38	14.42	0.095	-4.17	-0.14	-5
$T012$	0.1	16	1.77	17.77	1.72	17.76	0.097	-2.82	-0.06	-3
$T013$	0.1	20	2.22	22.22	2.13	22.19	0.096	-4.05	-0.14	-4
$T014$	0.1	23	2.55	25.55	2.44	25.51	0.095	-4.31	-0.20	-5
$T015$	0.1	26	2.88	28.88	2.73	28.81	0.094	-5.21	-0.24	-6
$T041$	0.4	13	8.66	21.66	8.60	21.64	0.397	-0.69	-0.09	-0.75
$T042$	0.4	16	10.66	26.66	10.59	26.63	0.397	-0.66	-0.11	-0.75
$T061$	0.6	13	19.5	32.5	19.43	32.47	0.598	-0.36	-0.09	-0.33

Table 3.3: Total effect of the three heat sources on the minimum and maximum values of the SIF as well as the R-ratio near the crack tip. The SIF are expressed in $MPa.\sqrt{m}$.

From Table 3.3, it can be seen that considering the total effect of the three heat sources, s_{the}, d_1, and q, particularly increases the consequences on the minimum value of the SIF as well as the applied R-ratio, while the maximum value of the SIF remains less affected and the associated impact can be neglected. Therefore, although one heat source may have low consequences on these parameters compared to other heat sources, considering their total effect leads to a significant decreasing impact on the fatigue crack parameters K_{Imin} and R, particularly at low applied load ratios and high applied SIF ranges as illustrated in the case of the fatigue crack growth test $T015$.

Besides the fatigue crack parameters, K_{Imin}, K_{Imax}, and R, it would also be interesting to know the order of impact the fatigue crack growth rate would have. This point is discussed in the next section.

3.6 Consequence of the cyclic plasticity dissipated into heat in the RCPZ, on the fatigue crack growth rate

Given the pronounced impact on the R-ratio, near the crack tip, of the cyclic plasticity dissipated into heat in the RCPZ, q, it is interesting to see how this could impact the fatigue crack growth rate, $\frac{da}{dN}$, since it is one of the key parameters used in studying the fatigue crack growth behavior.

As it has already been introduced in Section §1.2.1 in Chapter I, the load ratio, R, has indeed an effect on the fatigue crack growth rate, $\frac{da}{dN}$, and many models are proposed in the literature to take this effect into account when modeling the behavior of fatigue crack growth. For example, [Sperr, 1977] proposed the following law enabling to assess the fatigue crack growth rate by considering the load ratio effect:

$$\frac{da}{dN} = C.\frac{(\Delta K - \Delta K_{th})^m}{(1-R).K_c - \Delta K}, \tag{3.54}$$

where C and m are experimental constants, ΔK_{th} is the threshold of the SIF range, K_c is the material toughness, and ΔK is the applied SIF range.

By considering the main results obtained in the two previous sections, about consequences of the thermal effects on the SIF, namely: negligible impact on the SIF amplitude, and remarkable effect of the heat source q on the R-ratio near the

crack tip, the resulting consequence on the calculation of $\frac{da}{dN}$, according to Equation (3.54), would then come from the R-ratio by considering the thermal effect due to the heat source q, and assuming that the applied SIF range ΔK is constant[1].

In this manner, let $\Delta(\frac{da}{dN})$ and ΔR be the absolute corrections, respectively associated with, $\frac{da}{dN}$ and R, generated by the effect of the heat source q. The relative corrections associated with $\frac{da}{dN}$ can be written from Equation (3.54) and deduced as follows:

$$\Delta(\frac{da}{dN}) = C.K_c \frac{(\Delta K - \Delta K_{th})^m}{[(1-R).K_c - \Delta K]^2} \Delta R, \tag{3.55}$$

thus:

$$\frac{\Delta(\frac{da}{dN})}{\frac{da}{dN}} = \frac{K_c.R}{(1-R).K_c - \Delta K} \frac{\Delta R}{R}. \tag{3.56}$$

For the example of the applied load block of the fatigue crack growth test $T015$ ($\Delta K_I = 26MPa.\sqrt{m}$, $R = 0.1$, $f = 98.6Hz$, and $a = 31.3mm$), the effect of the heat source, q, on the R-ratio near the crack tip is $\frac{\Delta R}{R} = -3.12\%$ (*cf.* Table 3.2). As a result, with the numerical values: $\Delta K_I = 26MPa$, $R = 0.1$, and the typical value of the material toughness for mild steels $K_c = 40MPa.\sqrt{m}$, Equation (3.56) gives the impact of the heat source, q, on the fatigue crack growth rate:

$$\frac{\Delta(\frac{da}{dN})}{\frac{da}{dN}} = -1.24\%. \tag{3.57}$$

Hence, within the conditions of the fatigue crack growth test $T015$, the corresponding heat source q tends to slightly decrease the fatigue crack growth rate by 1.24%.

Now, by inversely proceeding, the point is to find the order of magnitude of the SIF thermal correction, $K^q_{I_{temp}}$, due to the heat source, q, in order to get a significant correction, of -10% for example, on the fatigue crack growth rate, $\frac{da}{dN}$.

By considering $\Delta K_I = 26MPa.\sqrt{m}$, $R = 0.1$, and $K_c = 40MPa.\sqrt{m}$, the R-ratio near the crack tip should be modified by $\frac{\Delta R}{R} = -25\%$ according to Equation (3.56). This leads to write:

[1]Under force control, the applied SIF range, ΔK, is not constant as it depends on the crack length which increases during the fatigue test. But in this context, it can be supposed constant since the change in ΔK is small during one applied load block ($\leq 7\%$).

$$\frac{\Delta R}{R} = \frac{R^{corr,q} - R}{R} = -0.25 \quad \Rightarrow \quad R^{corr,q} = 0.075. \tag{3.58}$$

In other words, and according to Equation (3.47), the thermal correction $K^q_{I_{temp}}$ is:

$$K^q_{I_{temp}} = \frac{\Delta K}{2} \frac{1 + R^{corr,q}}{1 - R^{corr,q}} - K^m_I, \tag{3.59}$$

where $K^m_I = \frac{\Delta K_I}{2} \frac{1+R}{1-R} = 15.88 MPa.\sqrt{m}$ for this example ($\Delta K_I = 26 MPa.\sqrt{m}$ and $R = 0.1$), which gives a thermal correction of $K^q_{I_{temp}} = -0.77 MPa.\sqrt{m}$. For the C40 steel and according to similar conditions of applied loading (fatigue test $T015$), $K^q_{I_{temp}} = -0.091 MPa.\sqrt{m}$ (*cf.* Table 3.1). This means that, in order to get a significant impact on the fatigue crack growth rate, $\frac{da}{dN}$, greater than 10% for example, the cyclic plastic dissipation in heat in the RCPZ needs to be about ten times that which has been estimated within the scope of this work (*cf.* Table 2.6, Chapter II). Therefore, this lets think about the factors that could amplify the effect of the heat source q.

3.7 Conclusion of Chapter III

From studying the consequences, on the SIF, of the heat sources, s_{the}, d_1, and q, it can be concluded that:

- The thermoelastic source, s_{the}, modifies the SIF range, ΔK_I, while the dissipative heat sources, d_1, and q, modify the mean SIF, K^m_I.
- Within the scope of the fatigue crack growth tests carried out in this work at loading frequencies $f \approx 100 Hz$ with C40 steel, each of the three heat sources generates a low impact on the SIF. For example, under the applied loading of the fatigue test $T015$ ($\Delta K_I = 26 MPa.\sqrt{m}$, $R = 0.1$), the thermoelastic source, s_{the}, increases the SIF range, ΔK_I, by 0.31%; the intrinsic dissipation due to microplasticity, d_1, decreases the mean SIF, K^m_I, by 0.13%; and the cyclic plastic dissipation in heat, q, decreases the mean SIF by 0.57%.
- Even though these impacts are low, the one related to the heat source, q, is distinctly higher than those generated by the heat sources, s_{the}, and d_1.
- These changes consequently lead to modify the fatigue crack parameters, $K_{I_{min}}$,

$K_{I_{max}}$, and the R-ratio near the crack tip. The cyclic plasticity dissipated into heat in the RCPZ, q, has the greatest impact on these parameters.

- When the total effect of the three heat sources is considered, it impacts more the SIF as well as the fatigue crack growth parameters. For example, for the same example of loading conditions as above (test $T015$), the heat source, q, decreases the R-ratio near the crack tip by 3.12%, while the three heat sources decrease it by 6%.

- By considering the change of the R-ratio near the crack tip generated by the heat source, q, it implies an increase of the fatigue crack growth rate, $\frac{da}{dN}$. Within the same loading example, $\frac{da}{dN}$ is increased by 1.24%, which is small and can be neglected.

- In order to get the fatigue crack growth rate, $\frac{da}{dN}$, decreased by 10% for instance, the heat source, q, should decrease the R-ratio near the crack tip by 25%, which means that the heat source, q, should be ten times greater than that dissipated in the RCPZ with C40 steel.

Having considered these conclusions, it should be known that among the key factors to get a more dissipative heat source, q:

(i) The applied SIF range, ΔK_I, since the heat source, q, is proportional to, ΔK_I^4 (*cf.* Figure 2.25, Section §2.4.3 in Chapter II). Therefore, carrying out fatigue crack growth tests at high SIF ranges implies an increase of the cyclic plasticity dissipated into heat in the RCPZ, q.

(ii) The loading frequency since the three heat sources are linearly proportional to the frequency. Thus, increasing the loading frequency leads to amplify the thermal effects, particularly that related to the cyclic plasticity dissipated into heat in the RCPZ, q.

(iii) The cyclic plastic behavior of the material since the cyclic plasticity occurring in the RCPZ is the origin of the heat source, q. A material with high cyclic plastic strain energy in the RCPZ would dissipate more considerable heat during fatigue crack growth.

For the two first items, they are unfortunately difficult to achieve in practical use since such fatigue tests imply an important increase of fatigue crack growth rate, which makes the tests complicated to carry out. Moreover, the set of hypothesis adopted in this work makes the methodology (*cf.* Section §3.2) used to calculate the

thermal corrections of the SIF, very limited, especially the hypothesis of decomposing the main problem under the conditions of the LEFM which may not be fulfilled at high applied SIF ranges. An attempt is however made, in the next chapter, to initiate the study leading to investigate the effect of the loading frequency on the heat source, q, and its resulting consequence on the SIF.

With regard to the last item above, a study carried out within the scope of this PhD work is presented in the next chapter. The idea is to correlate the heat source, q, with the cyclic behavior of the material, in order to numerically estimate its value instead of doing the experimental investigation presented in Section §2.4.3 (Chapter II). This actually enables to identify the type of materials having a cyclic plastic behavior making the heat source, q, more apparent and dissipative than that of the C40 steel.

Chapter 4

Exploring the consequences of the loading frequency and the material behavior on the cyclic plasticity dissipated into heat in the RCPZ

Contents

Ce dernier chapitre est consacré à l'exploration des effets potentiels sur la source de dissipation liée à la plasticité cyclique en pointe de fissure, que peuvent engendrer la fréquence du chargement et le comportement du matériau. Cet intérêt vient suite aux conclusions du chapitre précédent où il a été souligné que la plasticité cyclique dissipée en chaleur à la pointe de la fissure génére un effet, sur le facteur d'intensité des contraintes, plus important par rapport aux effets liés aux deux autres sources. Donc si cette source de chaleur devient plus considérable, cela induit une correction thermique plus significative sur le facteur d'intensité des contraintes.

La fréquence du chargement est parmi les facteurs qui modifient l'intensité des sources de chaleur. Son augmentation implique une amplification des effets thermiques, en particulier celui lié à la source de dissipation plastique en pointe de fissure, ce qui en conséquence peut engendrer une correction thermique non-négligeable du facteur d'intensité des contraintes. Afin de vérifier ce point, des essais de propagation de fissure sous des fréquences ultrasoniques sont effectués. Cette étude est présentée dans la première partie de ce chapitre.

En sus de la fréquence du chargement, le comportement cyclique du matériau joue aussi un rôle dans la définition de la dissipation plastique en chaleur puisque cette source tire son origine de la plasticité cyclique produite en pointe de fissure. L'étude présentée dans la deuxième partie de ce chapitre, consiste à corréler numériquement la source de dissipation plastique et le comportement plastique cyclique de l'acier utilisé dans ce travail, l'acier C40. Cette étape permet en fait d'identifier une loi élasto-plastique cyclique modélisant le comportement cyclique du C40, ce qui permettra à la fin, en modifiant les paramètres de cette loi, de voir si un matériau plus dissipatif que l'acier C40 existe.

The last chapter of this thesis explores potential effects of the loading frequency and the material behavior, on the cyclic plasticity dissipated into heat at the crack tip. The motivation behind this study actually comes from the conclusions drawn in the last chapter where it turned out that the heat source in question has the most important effect on the stress intensity factor compared to those resulting from the two other heat sources. So, if this heat source is great, its resulting consequence on the stress intensity factor is great too.

The loading frequency is among the factors that modify the heat sources. Increasing the loading frequency amplifies the thermal effects, especially that related to the cyclic plasticity dissipated into heat at the crack tip. As a consequence, the associated thermal correction of the stress intensity factor would be more significant. In order to verify this point, ultrasonic fatigue crack growth tests are carried out. This is presented in the first part of this chapter.

Besides the loading frequency, the material cyclic behavior also plays a role in defining the cyclic plasticity dissipated into heat at the crack tip. The second part of this chapter presents a study aiming to numerically correlate the cyclic plastic dissipation in the reverse cyclic plastic zone, with the cyclic behavior of the material used in this work, the C40 steel. This enables to identify a cyclic elastic-plastic constitutive model of C40 steel, whose parameters are afterward modified in order to see if a material, more dissipative than C40 steel, exists.

4.1 Effect of the loading frequency on the cyclic plasticity dissipated into heat in the RCPZ

Given the motivation mentioned at the end of the previous chapter, this section comes to present the attempt made in this work in order to estimate the effect the loading frequency may have on the cyclic plastic dissipation in the RCPZ, q. For this purpose, ultrasonic fatigue crack growth tests were carried out with loading frequencies of about $20kHz$ by using ultrasonic fatigue concepts ([Bathias and Paris, 2005]).

It should be known that in conventional fatigue tests, the frequency is that of the external load system of the testing machine, which is different from the natural frequencies of the specimen. In other words, the specimen is in forced vibration. An ultrasonic fatigue test differs from this in that the external frequency supplied by the testing machine must be one of the natural frequencies of the specimen. This is the definition of free vibration.

Therefore, the specimens used in ultrasonic fatigue crack growth tests must be specially designed. The geometry is determined with a specific procedure, detailed in [Bathias and Paris, 2005], so that the displacement is maximum at both extremities of the specimen whereas stresses and strains vanish at the same places. Moreover, in order to obtain maximum stress in the middle of the specimen, it is designed with a reduced section in the center as shown in Figure 4.1. The length L_1 is called the resonance length, the determination of which involves a numerical approach, such as FEA. The reduced section in the specimen center also enables to optimize the geometry by reducing the resonance length L_1.

Thus, a three-dimensional 'modal analysis' study using FEA was carried out, with the software *Abaqus 6.12*, to determine the geometry of notched specimens for ultrasonic fatigue crack growth tests. Indeed, free vibration modes are computed by FEA for several specimen geometries with different resonance lengths, and the final geometry is chosen so that the resonance frequency of the longitudinal vibration mode (along $\vec{z}$ axis of Figure 4.1) is as close as possible to that of the ultrasonic fatigue machine, $f \approx 20kHz$, and the other vibration modes have resonance frequencies outside the range $20Khz \pm 500Hz$ (which is the operating frequency range of the ultrasonic fatigue machine). The dimensions of the specimen shown in Figure 4.1 give a longitudinal vibration mode with a resonance frequency of $19966Hz$, while the closest vibration modes are those of torsion with resonance frequencies of $17485Hz$ and $21257Hz$. Then, the ultrasonic notched specimens made of C40 steel

are designed with the computed geometry illustrated in Figure 4.1.

Dimensions	Values (mm)
$2R_1$	2.5
$2R_2$	5
L_1	46.9
L_2	12.2
W	14
R_0	60

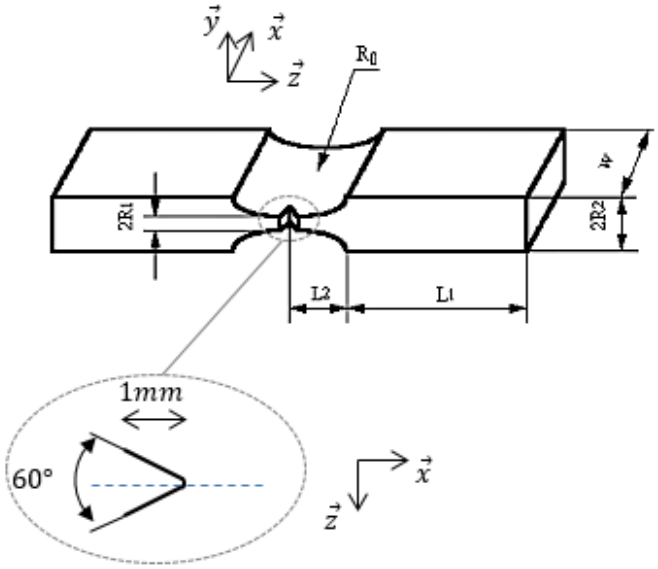

Figure 4.1: Computed dimensions of the specimen used during the ultrasonic fatigue crack growth tests. The geometry shape is that of [Wu and Bathias, 1994].

The ultrasonic fatigue crack growth tests were carried out under applied load blocks of SIF ranges, ΔK_I, with a load ratio, $R = -1$. It should be noted that at ultrasonic loading frequencies, under $R = -1$, it is not yet known how to assess the crack opening SIF, $K_{I_{op}}$, and then the effective SIF range, $\Delta K_{I_{eff}} = K_{I_{max}} - K_{I_{op}}$. That is why, it is assumed that, $K_{I_{op}} = 0$, which means that the part of cyclic loading where crack closure occurs is neglected, and then, $\Delta K_I = K_{I_{max}}$. Therefore, the determination of the SIF in a vibratory regime is needed. This can be done by FEA.

[Wu and Bathias, 1994] proposed a rough approximation of $K_{I_{max}}$ (Equation (4.1)), within the hypothesis of the LEFM for a plane strain problem, as a function of the displacement amplitude applied by the ultrasonic fatigue machine, U_0, the dynamic Young's modulus, E_d, the Poisson's ratio, ν, the crack length, a, and a geometrical function, $f(a/W)$:

$$K_{I_{max}} = \frac{E_d}{1-\nu^2}\sqrt{\frac{\pi}{a}}U_0 f(a/W), \tag{4.1}$$

with $E_d = 209GPa$ and $\nu = 0.3$ for the C40 steel. The C40 steel dynamic Young's modulus, E_d, is determined according to a method in [Bathias and Paris, 2005], and it can be seen that it is close to the static Young's modulus ($E = 210GPa$).

In order to establish the geometrical function, $f(a/W)$, $K_{I_{max}}$ is computed by carrying out three-dimensional finite element 'harmonic response analysis' with the software *ANSYS 13.0 (Mechanical APDL)*. An assembly of the ultrasonic fatigue machine horn and the specimen is modeled to better predict the resonance frequency computed before doing the harmonic analysis. Moreover, a regular fine finite element mesh resolution is applied in the crack region with 8-node isoparametric quadratic and quadrilateral elements, with a size of $70\mu m$ (Figure 4.2). This mesh resolution was checked by doing a static finite element calculation with an applied static tension stress, σ_0, at the top of the specimen, and then the SIF, K, was computed and compared with an asymptotic formula (Equation (4.2)) given for this case in [Tada et al., 2000]. For a crack length $a = 4.9mm$ for example, the relative error related to both SIF solutions is 7%. It should be mentioned that this FEA model uses a symmetry with respect to $(\vec{y}, \vec{z})$ plane, as shown in Figure 4.2, in order to reduce the computation time.

$$K_I = \sigma_0\sqrt{\pi a}\left(1.122 - 0.231(\frac{a}{W}) + 10.55(\frac{a}{W})^2 - 21.71(\frac{a}{W})^3 + 30.382(\frac{a}{W})^4\right). \tag{4.2}$$

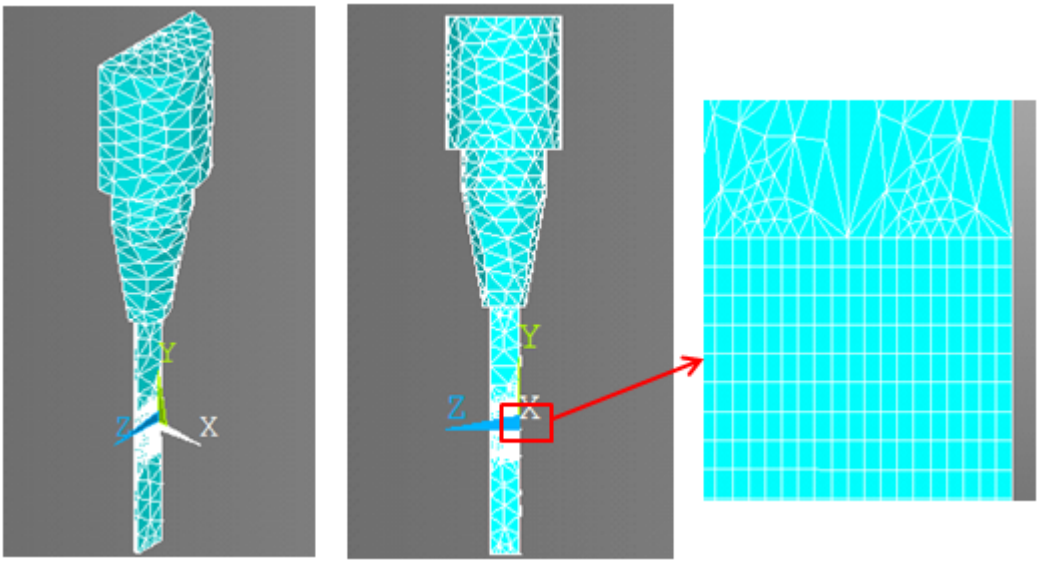

Figure 4.2: Finite element mesh used to compute the geometrical function $f(a/w)$ from the calculation of $K_{I_{max}}$.

Furthermore, the crack is assumed to be stationary in the harmonic analysis response, and the method of crack opening displacement ([Burdekin and Stone, 1966]) is used in *ANSYS* post-treatment to calculate $K_{I_{max}}$. An *ANSYS* script was

then created to carry out this calculation through three steps:

- Given a crack length, a, a first modal analysis step is done to compute the resonance frequency, denoted hereinafter by f_r, corresponding to the longitudinal vibration mode.
- A harmonic response analysis is then carried out by applying an arbitrary displacement amplitude, $U_0 = 16\mu m$ for instance, and the resonance frequency, f_r, computed in the first step.
- Then, the SIF, $K_{I_{max}}$, is computed under the plane strain condition by using the function 'KCALC' of *ANSYS*, [AnsysFracture, 2010]. The corresponding value of the geometrical function, $f(a/W)$, is therefore deduced by using Equation (4.1).

Table 4.1 reports the numerical values of the computed geometrical function, $f(a/W)$, for three given crack lengths.

$a(mm)$	a/W	$f_r(Hz)$	$K_{I_{max}}(MPa.\sqrt{m})$	$f(a/W)$
0.7	0.05	20317	8.20	0.03
2.1	0.15	20269	22.24	0.15
3.5	0.25	20192	39.05	0.35

Table 4.1: Calculation of the geometrical function $f(a/W)$.

Afterward, the geometrical function, $f(a/W)$, is plotted against, a/W, and approximated by polynomial regression as shown in Figure 4.3.

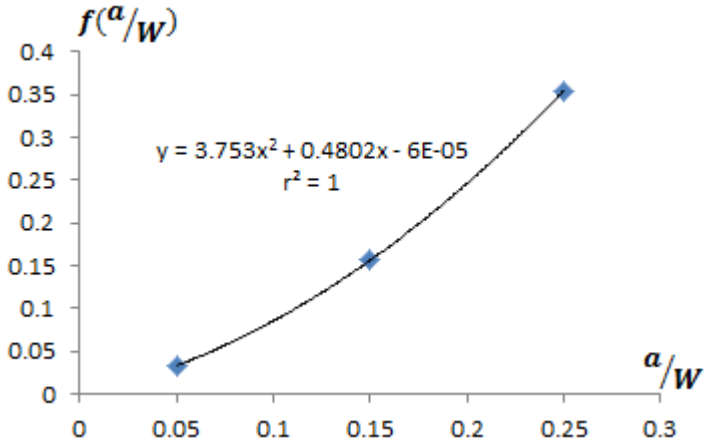

Figure 4.3: Approximation of the geometrical function, $f(a/W)$.

The approximated geometrical function is then used to expedite ultrasonic fatigue crack growth tests under applied SIF ranges.

The assumptions which enabled to carry out conventional fatigue crack growth tests, previously presented in Section §2.4.3 (Chapter II), are considered to carry out ultrasonic fatigue crack growth tests. It must be known that one major problem was encountered during these tests, that of fast crack propagation, which made applied load blocks complicated to control, particularly maintaining a quasi-constant applied SIF range under the condition $\frac{\Delta K_{I_f} - \Delta K_{I_i}}{\Delta K_{I_i}} \leq 7\%$. This problem consequently calls into question the hypothesis of stationary heat source, q, assumed during one applied load block. In addition, the condition stating that for a load block, i, the crack must be propagated outside the RCPZ created during the load block, $i-1$, was also complicated to control.

The experimental device used to carry out the ultrasonic fatigue crack growth tests is presented in Figure 4.4. The infrared camera and the optical camera used during the conventional fatigue crack growth tests are reused in this experimental investigation. The infrared camera has the same configuration presented before (Section §2.4.2 in Chapter II).

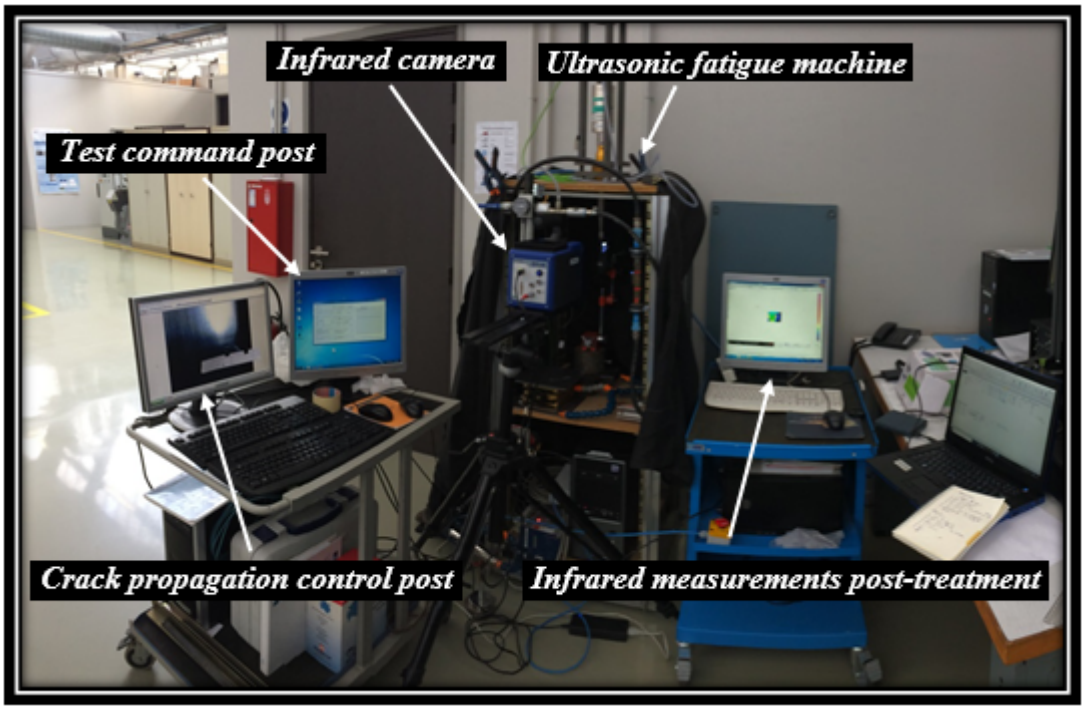

Figure 4.4: Experimental device used during the ultrasonic fatigue crack growth tests.

The experimental conditions of applied load blocks during ultrasonic fatigue crack growth tests are presented below in Table 4.2. The tests are referenced as follows: UXY, X for the specimen reference number, and Y for the test reference number. It should be mentioned that the specimens were initially pre-cracked by applying a low SIF range of, $\Delta K_I = 7MPa.\sqrt{m}$, with ultrasonic frequencies, $20119 \leq f \leq 20126Hz$, for a pre-cracking test duration varying between $60s$ and $180s$. The lengths of pre-cracks, for the three specimens reported in Table 4.2, are $2mm$, $1.4mm$, and $2.8mm$, respectively. The crack lengths, a_i and a_f, take into account the size of the machined initial notch ($1mm$, *cf.* Figure 4.1). Moreover, the size of the RCPZ, modeled by a disc with the radius, r_p^*, is estimated according to Irwin's model under plane stresses hypothesis by considering the value of ΔK_{I_f} in Equation (1.9) (*cf.* Chapter I).

Test ref.	R	Δt (s)	f (Hz)	N $(cycles)$	a_i (mm)	ΔK_{I_i} $(MPa.\sqrt{m})$	a_f (mm)	ΔK_{I_f} $(MPa.\sqrt{m})$	$\delta(\Delta K_I)$ (%)	$2r_p^*$ (mm)
$U11$	-1	894.4	20124	1.79×10^7	2	9	2	9	0	0.16
$U12$	-1	51.63	20124	1.04×10^6	2	10.5	2.1	11.04	5.14	0.24
$U13$	-1	45	20119	9.05×10^5	2.1	11	2.9	15.58	41.63	0.48
$U14$	-1	143.9	20113	2.89×10^6	2.9	12	3.4	14.37	19.75	0.41
$U15$	-1	74.9	20087	1.5×10^6	3.4	16	4.7	23.52	47	1.10
$U16$	-1	106.3	20016	2.12×10^6	4.7	20	7	33.05	65.25	2.16
$U21$	-1	1.3	20119	2.61×10^4	1.4	16	1.7	19.28	20.50	0.74
$U31$	-1	41.7	20116	8.38×10^5	2.8	14	3.3	16.85	20.35	0.56
$U32$	-1	19.6	20115	3.94×10^5	3.3	18	3.9	21.87	21.50	0.95

Table 4.2: Applied loading conditions per block during ultrasonic fatigue crack growth tests, with $\delta(\Delta K_I) = \frac{\Delta K_{I_f} - \Delta K_{I_i}}{\Delta K_{I_i}}$.

As the outcome of these tests, besides the problem of maintaining a constant applied SIF range during one load block, it was found that the intrinsic dissipation has a significant effect that is manifested by a temperature increase in the central area of the specimen far from the crack tip, and this consequently noises the temperature increase resulting from the heat source, q, generated in the vicinity of the crack tip. Indeed, at low applied SIF ranges ($\Delta K_{I_i} \leq 14MPa.\sqrt{m}$), the temperature increase at the crack tip was so low that it was impossible to be observed by the IR camera because of the effect of intrinsic dissipation becoming more significant

in all the specimen central part as the test goes on. While at high SIF ranges, the increase of temperature at the crack tip starts to be observable, but the crack moves fast and does not let the heat to diffuse enough ahead of the crack tip, in addition, the applied SIF range increases because of the increase of the crack length, and the intrinsic dissipation quickly becomes more pronounced and hides the temperature increase at the crack tip.

Given these hurdles, the only load block of ultrasonic fatigue crack growth tests which allowed to clearly observe the temperature increase due to the cyclic plastic dissipation in heat in the RCPZ, is that referenced by $U21$ in Table 4.2. Although it is so quick with a duration of $1.3s$ (2.61×10^4 cycles), the temperature increase at the crack tip, ΔT_q^{exp}, is distinctly detectable by the IR camera as shown in Figure 4.5, particularly at $t = 0.6s$ before the intrinsic dissipation due to microplasticity starts to increase. The temperature increase due to the intrinsic dissipation related to microplasticity is about $32°C$ as shown in Figure 4.5, and thus, ΔT_q^{exp} at the crack tip is obtained by subtracting the part of temperature due to this intrinsic dissipation, that being $\Delta T_q^{exp} = 6.63°C$.

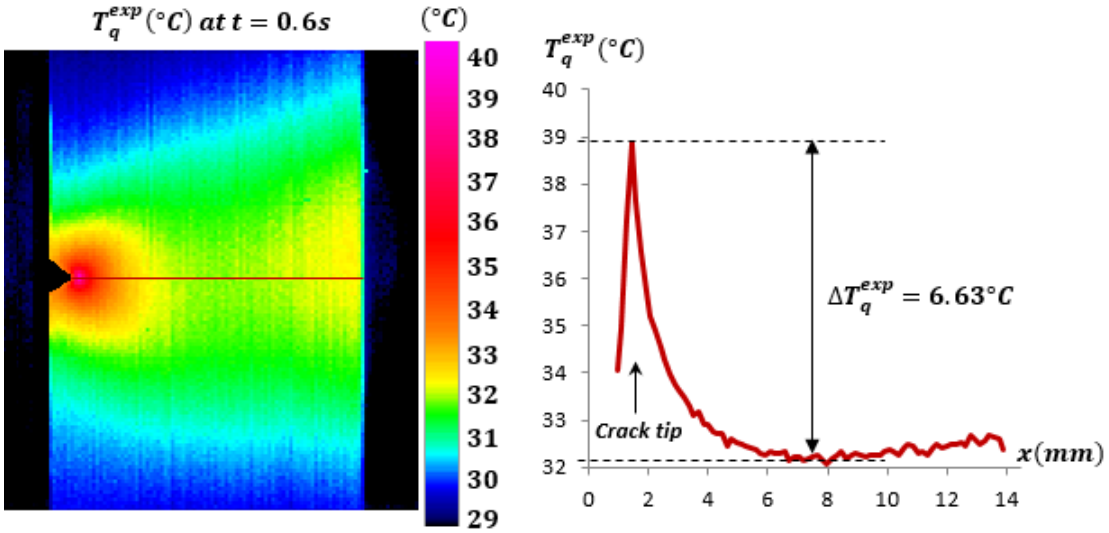

Figure 4.5: Increase of the temperature at the crack tip, at $t = 0.6s$, for the applied load block of the ultrasonic fatigue crack growth test $U21$ ($\Delta K_{I_i} = 16MPa.\sqrt{m}$, $a_i = 1.4mm$, $f = 20119Hz$, and $R = -1$). The temperature curve on the right is plotted along the red line in the middle of the specimen.

The cyclic plasticity dissipated into heat in the RCPZ and produced during the load block of the test, $U21$, is estimated by using the same method previously presented for estimating the heat source, q, in conventional fatigue crack growth tests

(*cf.* Section §2.4.3 of Chapter II). Indeed, a two-dimensional FEA, with the same *Matlab* code developed in this work for solving the thermal and thermomechanical problems previously presented, was carried out to solve the corresponding heat diffusion equation with the unit heat source, $q_1 = 1W.m^{-1}$ (*cf.* Equation (2.26)). It should be noted that this two-dimensional FEA is a simplified model which does not take into account the variable thickness of thin ultrasonic specimens. The temperature increase, ΔT_{q_1}, generated by the unit heat source, is computed and the associated value, at $t = 0.6s$, determined outside the singular region (at $x = 2.5mm$) is $\Delta T_{q_1} = 0.0055°C$. The equivalent real temperature increase, ΔT_q^{exp}, measured at the same position and time ($x = 2.5mm$ and $t = 0.6s$) is $1.91°C$. Therefore, the cyclic plasticity dissipated into heat during the test, $U21$, is $q = 347.27W.m^{-1}$ (by using Equation (2.27), Chapter II).

In order to check the validity of the calculations done above to estimate the heat source, q, the temperature field in the middle of the specimen along x axis is computed from the estimated heat source, $q = 347.27W.m^{-1}$, by solving the associated two-dimensional model of heat diffusion equation (Equation (2.26)). The order of magnitude of the computed temperature field, shown below in Figure 4.6, is in agreement with the experimentally measured temperatures (Figure 4.5).

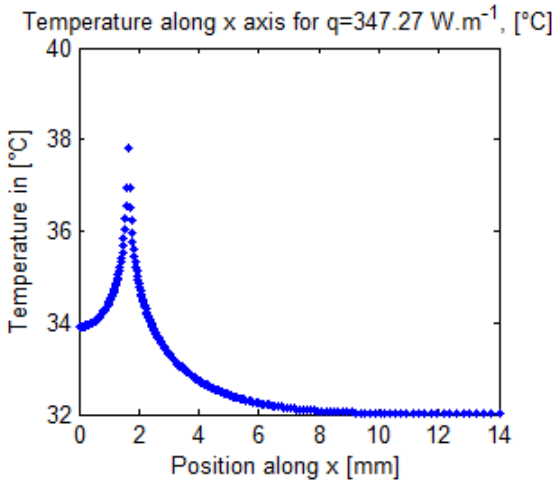

Figure 4.6: Computed temperature generated by the estimated heat source, $q = 347.27W.m^{-1}$, at $t = 0.6s$, plotted along x axis in the middle of the specimen.

The closest loading configuration to that of the test $U21$ ($\Delta K_{I_i} = 16MPa.\sqrt{m}$, $a_i = 1.4mm$, $f = 20119Hz$, and $R = -1$), in terms of applied SIF range, is that of the load block of the conventional fatigue crack growth test, $T012$, carried out under the same SIF range at loading frequency, $f = 100Hz$, and applied R-ratio, $R = 0.1$.

Its associated heat source, q, previously estimated is, $q = 17.47W.m^{-1}$. It then turns out that the heat source, q, produced during the ultrasonic fatigue test $U21$ is 19.87 times greater than that estimated during the conventional fatigue test $T012$. This ratio is however ten times lower than that expected, which actually results from the linear proportionality with respect to the loading frequencies, $\frac{20119}{100} = 201.19$. Two explanations are possible, either the cyclic behavior of the material has changed in the ultrasonic regime, or the heat source, q, estimated during the ultrasonic test has not yet reached its stabilized regime since it was determined at a very early time of the test $U21$ (at $t = 0.6s$).

With the estimated heat source, $q = 347.27W.m^{-1}$, the thermal correction of the SIF, $K^q_{I_{temp}}$, is computed by using the same methodology, presented in the previous chapter, used to calculate the thermal corrections of the SIF at loading frequencies $f \leq 100Hz$. That numerically gives, $K^q_{I_{temp}} = -0.152MPa.\sqrt{m}$, which however remains small compared with the values of the applied SIF range during the test $U21$, $16 \leq \Delta K_I \leq 19.28MPa.\sqrt{m}$.

Therefore, by starting exploring the effect of the loading frequency on the cyclic plasticity dissipated as heat in the RCPZ, it can be concluded that, ultrasonic fatigue crack growth tests do amplify the heat source q. This increase of the heat source, q, can consequently lead to a non-negligible thermal correction on the SIF contrary to what has been found in conventional fatigue crack growth tests. It should be noted that the methodology of decoupling the problem, which is implemented in this work in order to calculate the thermal corrections on the SIF, may unfortunately be not valid in the ultrasonic regime since the increase of temperature at the crack tip becomes more considerable as well as the intrinsic dissipation due to microplasticity, in other words, the thermomechanical coupling becomes more important and makes questionable the hypothesis of decoupling the problem. Then, a new calculation model needs to be implemented within this study in order to take into consideration the thermomechanical coupling when computing the stress field leading to calculate the thermal corrections on the SIF. Moreover, further work needs to be done in order to overcome the technical problems encountered during the ultrasonic experimental investigation.

4.2 Another approach to estimate the cyclic plasticity dissipated into heat in the RCPZ

The aim of this section is to propose a numerical correlation of the cyclic plasticity dissipated into heat in the RCPZ, q, with the cyclic plastic behavior of the material used in this work, C40 steel, in order to deduce the characteristics of potential materials more dissipative than the C40 steel. This is based on the statement assuming that the cyclic plasticity occurring in the RCPZ during fatigue crack growth tests, is mostly converted into heat for ductile materials. The purpose is first to experimentally characterize the cyclic behavior of the C40 steel by carrying out cyclic tension-compression tests with smooth flat specimens, and then establish a cyclic elastic-plastic constitutive model describing the behavior of the C40 steel as well as its plastic flow evolution. Afterward, this model is numerically implemented in order to compute the cyclic plastic energy dissipated per cycle in the RCPZ by using the software *Abaqus 14.5*. The validity of the results of the computed heat source, q, are first compared with those experimentally estimated in Section §2.4.3 (Chapter II), then the parameters of the C40 steel cyclic constitutive model can be modified in order to find a material with a cyclic plastic dissipation more significant than that obtained with the C40 steel.

4.2.1 Brief review of the cyclic behavior of materials

In the plasticity theory ([Lemaitre and Chaboche, 1990]), there are different ways of schematically representing the hardening of materials induced by deformations, namely:

- Isotropic hardening: a material will be considered to justify the hypothesis of isotropic hardening if the boundary of the elastic domain is found to depend only on a scalar parameter (Figure 4.7). The compression curve, subsequent to the initial loading in tension in a work-hardening test, can be derived from the monotonic tensile curve by a homothetic transformation centered at the point of the zero stress (point B in Figure 4.7) with ratio 1. The loading curves, which represent points corresponding to the limit of elasticity in a two-dimensional stress space, of normal stress and shear stress (tension-torsion tests on thin-walled tubes at different states of hardening), are derived from one another by homothetic transformation about the center 0 (Figure 4.7).

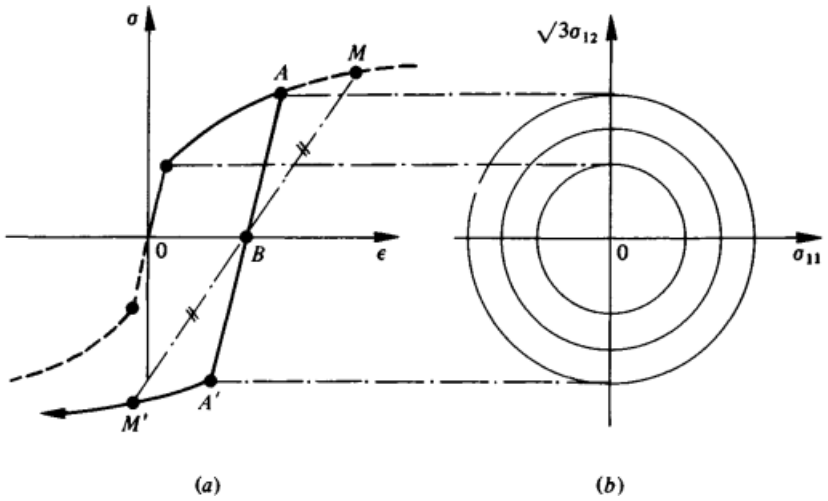

Figure 4.7: Isotropic hardening: (a) Tension-compression test, (b) tension-torsion test, [Lemaitre and Chaboche, 1990].

- Kinematic hardening: a very useful schematic representation of anisotropic hardening is that of kinematic hardening in which the elastic domain retains a constant size but moves about in the stress space by translation. The center of the elastic domain (point C in Figure 4.8) represents the internal stress of the neutral state (or back-stress). The one-dimensional compression curve can be derived from the new tension curve by a homothetic transformation with ratio -1 and center C. In the tension-torsion test, the loading curves corresponding to different hardening states, can be derived from one another by translation of the vectors such as $\overrightarrow{OC}$ (Figure 4.8).

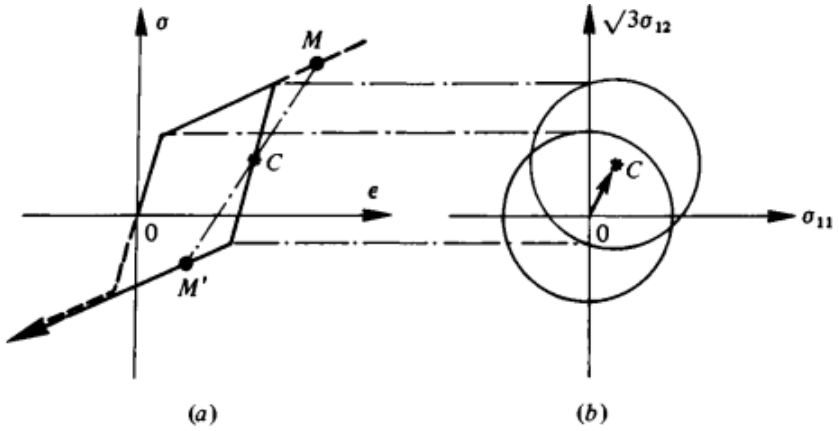

Figure 4.8: Kinematic hardening: (a) Tension-compression test, (b) tension-torsion test, [Lemaitre and Chaboche, 1990].

- Bauschinger effect: the Bauschinger effect manifests itself when a specimen is subjected to a tension followed by a compression. It is often found that since the tension test was carried out first, the material has hardened in tension (increased yield stress) but has softened in compression. Figure 4.9 shows that the yield stress in compression is lower than that if the test was carried out in compression first.

  Of the two simple schematic representations mentioned above, the kinematic hardening is closer to the real case and represents a first approximation to the Bauschinger effect, but this remains dependent on the material.

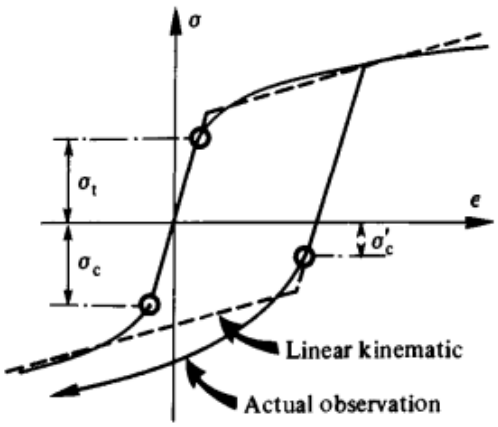

Figure 4.9: Bauschinger effect, [Lemaitre and Chaboche, 1990].

- Effect of cyclic loadings: under cyclic loadings, most metals and alloys experience a variation in their hardening properties. They may soften or harden depending on the material, temperature, and the initial state. The quantities generally used in describing the results of cyclic tests (with stabilized cycles) are defined in Figure 4.10.

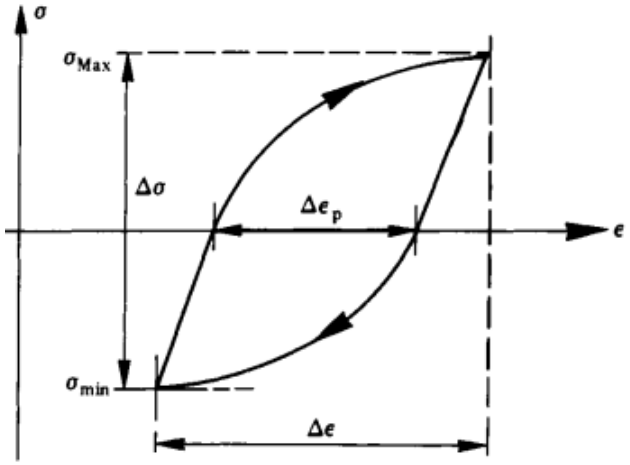

$$\bar{\sigma} = \frac{\sigma_{Max} + \sigma_{min}}{2}$$

$$\Delta\epsilon = \Delta\epsilon_e + \Delta\epsilon_p = \Delta\sigma/E + \Delta\epsilon_p$$

Figure 4.10: A stress-strain cycle, [Lemaitre and Chaboche, 1990].

The softening is said to occur when the stress range, $\Delta\sigma$, decreases during successive cycles under strain control, or when the strain range, $\Delta\varepsilon$, increases in a stress-controlled test. On the other hand, a cyclic hardening corresponds to a rise in the stress range, $\Delta\sigma$, when strain is controlled or to a fall in the strain range, $\Delta\varepsilon$, when the test is stress-controlled. When a periodic load induces a periodic response, there is a stabilized cycle leading to a stabilized stress-strain response.

If the load is not purely alternating, additional effects can occur. In non-symmetric stress-controlled tests, either shakedown may occur (stress-strain curve (a) of Figure 4.11) or, more often, a ratchetting effect may be induced (stress-strain curve (b) in Figure 4.11). Correspondingly, in a strain-controlled test, the phenomena of relaxation or non-relaxation of the mean stress may occur (stress-strain curves (c) and (d) in Figure 4.11).

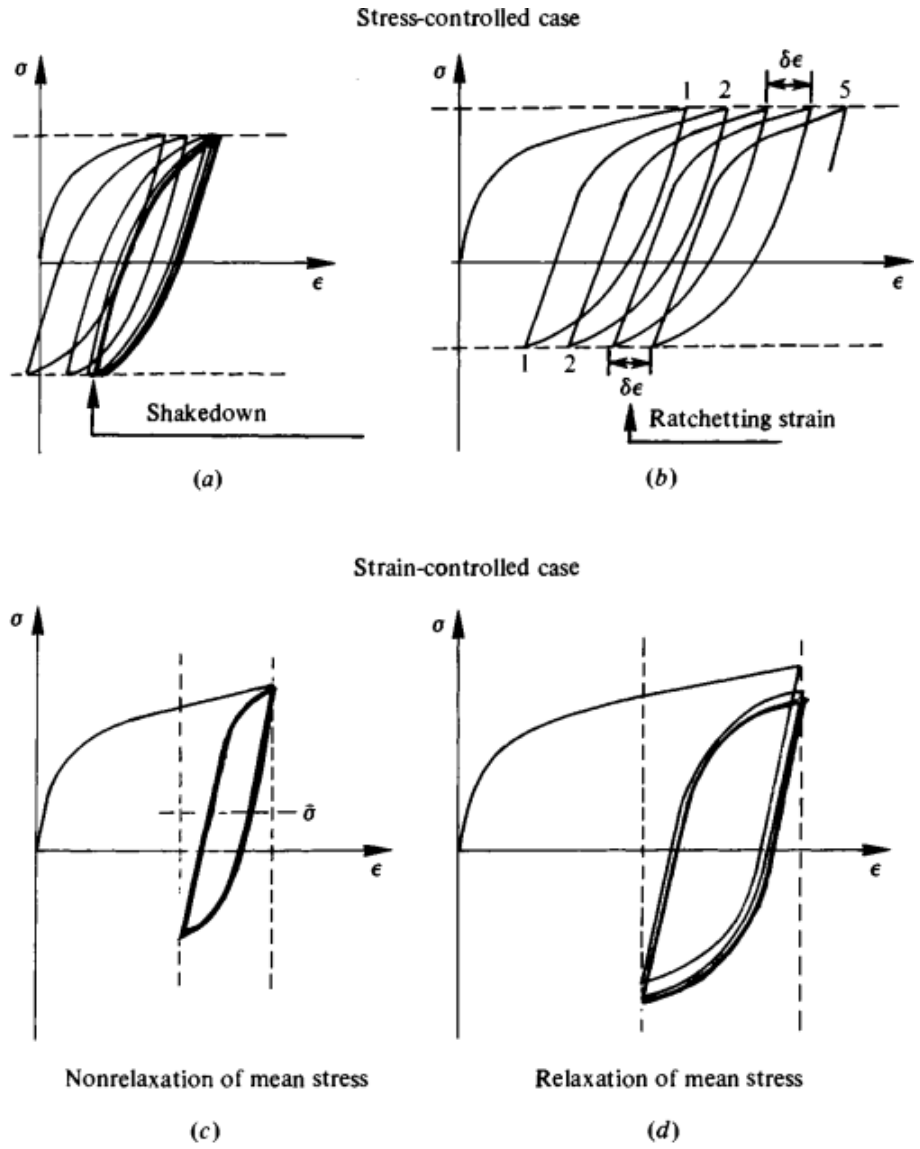

Figure 4.11: Phenomena of (a) shakedown, (b) ratchetting, (c) non-relaxation and (d) relaxation of the mean stress. [Lemaitre and Chaboche, 1990].

It should be reminded that during fatigue crack growth tests, previously presented in Chapter II, cyclic plasticity occurs in the RCPZ, while the behavior of the remainder of the CCT plate specimen is linear elastic. The emphasis is afterward made on the cyclic plastic behavior of the C40 steel. For this purpose, the hypothesis of partition, consisting in decomposing strain into elastic and plastic parts, as well as the assumption of time-independent plastic behavior are considered ([Lemaitre and Chaboche, 1990]) .

It is known that the hypothesis of kinematic hardening, mentioned above, can be used to model the inelastic behavior of materials that are subjected to cyclic loadings

([AbaqusPlasticity, 2012]). The models of kinematic hardening, used to simulate the behavior of metals subjected to cyclic loading, are pressure-independent plasticity models, in other words, yielding of metals is independent of the hydrostatic stress. These models are suited for most metals subjected to cyclic loading conditions, except voided materials.

In the following, the hypothesis of kinematic hardening model is considered. Moreover, the plasticity criteria used in this work is that of Von Mises yield surface defined by Equation (4.3) ([Lemaitre and Chaboche, 1990]):

$$F = f(\bar{\bar{\sigma}} - \bar{\bar{X}}) - \sigma_y = 0, \tag{4.3}$$

where σ_y is the monotonic yield stress defining the size of the yield surface, and $f(\bar{\bar{\sigma}} - \bar{\bar{X}})$ is the equivalent Von Mises stress with respect to the back-stress tensor $\bar{\bar{X}}$ (the back-stress is defined above by point C in the one-dimensional schematic stress-strain curve of Figure 4.8). The equivalent Von Mises stress is here defined by:

$$f(\bar{\bar{\sigma}} - \bar{\bar{X}}) = \sqrt{\frac{3}{2}.(\bar{\bar{\sigma}}^d - \bar{\bar{X}}^d) : (\bar{\bar{\sigma}}^d - \bar{\bar{X}}^d)}, \tag{4.4}$$

where $\bar{\bar{\sigma}}^d$ is the deviatoric stress tensor, and $\bar{\bar{X}}^d$ is the deviatoric part of the back-stress tensor.

Furthermore, the kinematic hardening models assume the hypothesis of associated plastic flow expressed by Equation (4.5):

$$\dot{\bar{\bar{\varepsilon}}}_p = \dot{\varepsilon}_p \frac{\partial F}{\partial \bar{\bar{\sigma}}}, \tag{4.5}$$

where $\dot{\bar{\bar{\varepsilon}}}_p$ is the rate of plastic flow and $\dot{\varepsilon}_p$ is the equivalent plastic strain rate. The evolution of the equivalent plastic strain rate is obtained from the following equivalent plastic work formula ([Lemaitre and Chaboche, 1990]):

$$\sigma_y.\dot{\varepsilon}_p = \bar{\bar{\sigma}} : \dot{\bar{\bar{\varepsilon}}}_p, \tag{4.6}$$

which yields $\dot{\varepsilon}_p = \sqrt{\frac{2}{3}\dot{\bar{\bar{\varepsilon}}}_p : \dot{\bar{\bar{\varepsilon}}}_p}$ for isotropic Von Mises plasticity.

When the kinematic hardening model is considered as linear, the simulation of the hardening behavior is carried out with a constant hardening rate. This hardening rate should be matched to the average hardening rate measured in stabilized cycles over a strain range, $\Delta\varepsilon$, corresponding to that expected in reality. A stabilized

cycle is obtained by cycling over a fixed strain range until a steady-state condition is reached, in other words, until the stress-strain curve no longer changes from one cycle to the next. When the kinematic hardening model is considered as non-linear, it gives better predictions by improving the shape of the cycles. Moreover, it enables to take into consideration the Bauschinger effect.

Therefore, in order to predict the cyclic behavior of the C40 steel, the model of non-linear kinematic hardening is considered. The evolution law of this model consists of two components: a non-linear kinematic hardening component, and a constant isotropic hardening component.

Indeed, the kinematic hardening component is defined to be an additive combination of a purely kinematic term (known as linear Ziegler hardening law, [Ziegler, 1959]) and a relaxation term (or the recall term) which introduces the non-linearity. By assuming that the temperature and field variables dependencies are neglected[1], the criterion and the non-linear kinematic hardening law can be respectively expressed in the form:

$$F = f(\bar{\bar{\sigma}} - \bar{\bar{X}}) - k = 0, \tag{4.7}$$

$$\dot{\bar{\bar{X}}} = C\frac{1}{\sigma_y}(\bar{\bar{\sigma}} - \bar{\bar{X}})\dot{\bar{\varepsilon}}_p - \gamma\bar{\bar{X}}\dot{\bar{\varepsilon}}_p, \tag{4.8}$$

where k, C, and γ, are material parameters that must be calibrated from experimental cyclic test data. Indeed, the parameter k is a specific cyclic yield stress generally different from the monotonic yield stress, σ_y. The parameter C is the kinematic hardening modulus, and the parameter γ determines the rate at which the kinematic hardening modulus decreases with increasing plastic deformation (Figure 4.12). When γ is zero, the kinematic hardening law (Equation (4.7)) becomes linear.

[1]In this study, this assumption is reasonable because of the very low temperature change compared with the material transformation temperatures.

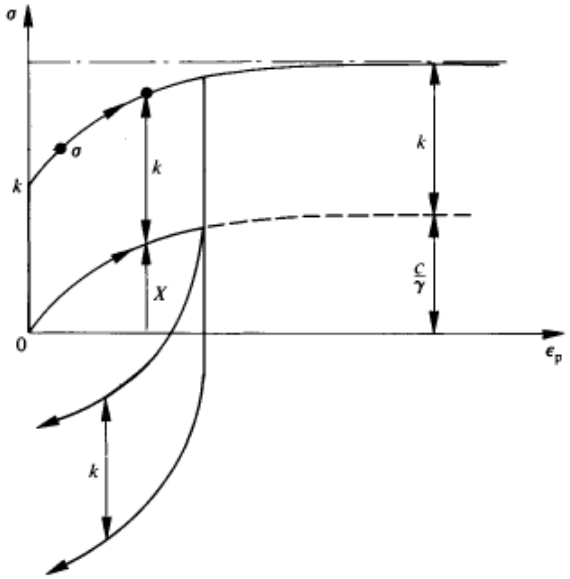

Figure 4.12: Non-linear kinematic hardening model in tension/compression, [Lemaitre and Chaboche, 1990].

Therefore, an identification of the material characteristic coefficients, k, C, and γ, is needed. This can be done in tension/compression from the stabilized hysteresis loops which correspond to different strain amplitudes, $\frac{\Delta\varepsilon}{2}$. According to [Lemaitre and Chaboche, 1990], estimating the values of k, C, and γ, can be done in three steps:

i. Determine the parameter, k, approximately from the elastic domain;
ii. Determine the ratio, $\frac{C}{\gamma}$, as an asymptotic value of the measure, $\frac{\Delta\sigma}{2} - k$, as $\Delta\varepsilon$ increases;
iii. Determine the γ coefficient by using Equation (4.9), and then deduce the C coefficient:

$$\frac{\Delta\sigma}{2} - k = \frac{C}{\gamma} \tanh\left(\gamma \frac{\Delta\varepsilon_p}{2}\right), \tag{4.9}$$

where $\Delta\varepsilon_p$ is the plastic strain range (Figure 4.10).

For this purpose, an experimental investigation consisting in determining the parameters, k, C, and γ, of the C40 steel is done by carrying out cyclic uniaxial tension/compression tests under strain control.

4.2.2 Cyclic tension/compression tests to determine the non-linear kinematic hardening coefficients of C40 steel

The testing machine used in this work to carry out uniaxial cyclic tension/compression tests is a $100kN$ MTS servo-hydraulic testing machine with vertical wedge grips. An axial contact extensometer, MTS 632.13 model with a $10mm$ gauge length, was used to perform strain measurement over the middle of the specimen gauge section. The specimens, made of C40 steel, were machined from large rectangular plates ($950 \times 700 \times 5mm$) in the rolling direction, and designed in a classical dog-bone thin and flat form (Figure 4.13) with narrower gauge section in order to ensure that the deformation occurs along the length with a constant area cross-section.

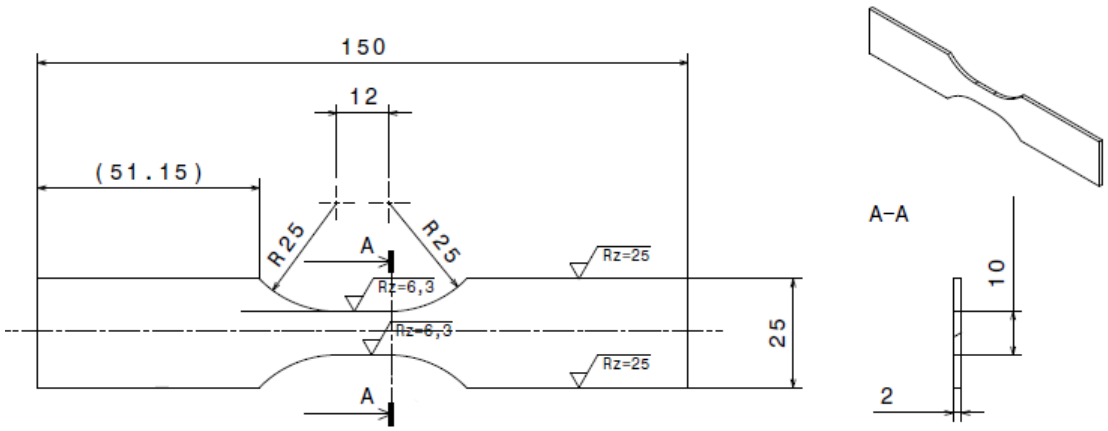

Figure 4.13: Geometry of the C40 steel specimens used in cyclic tension/compression tests. Dimensions are in mm.

The cyclic tension/compression tests were performed, at room temperature (around $20°C$), under strain control with constant strain amplitudes and a constant loading frequency, $f_L = 0.1Hz$, with a triangular waveform (Figure 4.14).

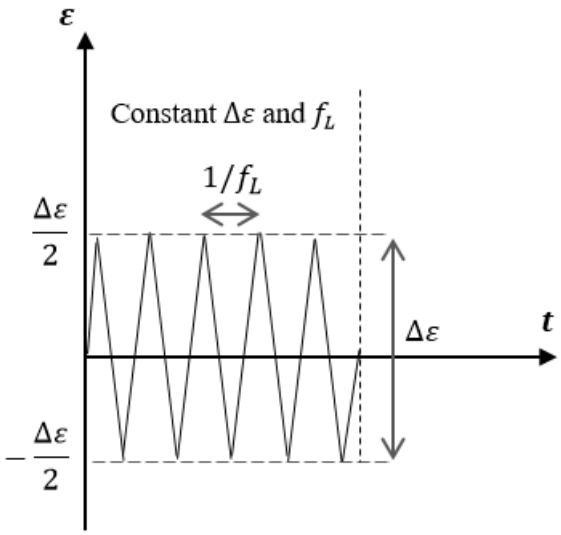

Figure 4.14: Schematic strain-time curve of applied loading.

In order to prevent instability due to possible buckling of the specimen in compression, an anti-buckling device was used as shown in Figure 4.15.

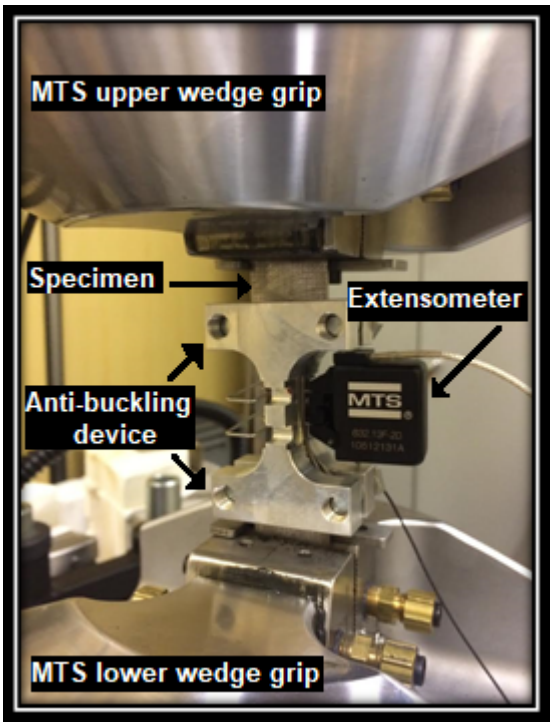

Figure 4.15: Assembly of the MTS machine, the specimen, the anti-buckling device, and the extensometer.

The cyclic test data, extracted during this experimental investigation, concern the axial strain and stress in the one-dimensional case, where the true strain, ε_{tr}, and the true stress, σ_{tr}, are considered for taking into account eventual changes of the specimen cross-sectional area. The assumption of material incompressible plasticity is adopted to write the true strain and true stress as follows ([Lemaitre and Chaboche, 1990]):

$$\varepsilon_{tr} = ln(1+\varepsilon), \tag{4.10}$$

$$\sigma_{tr} \approx \sigma(1+\varepsilon). \tag{4.11}$$

Figure 4.16 shows the stabilized hysteresis loops obtained for various applied strain amplitudes, $\frac{\Delta\varepsilon}{2}$ = 0.1%, 0.25%, 0.3%, 0.5%, 0.8%, 1%, and 1.5%. For each applied strain amplitude, a new specimen is used. It should be pointed out that the stabilized cycle is reached after about ten cycles of tension/compression loading. From the applied strain amplitude 1.5%, the buckling in the specimen gauge part starts to be more apparent, and that makes the tests complicated to carry out, even with the use of the anti-buckling device.

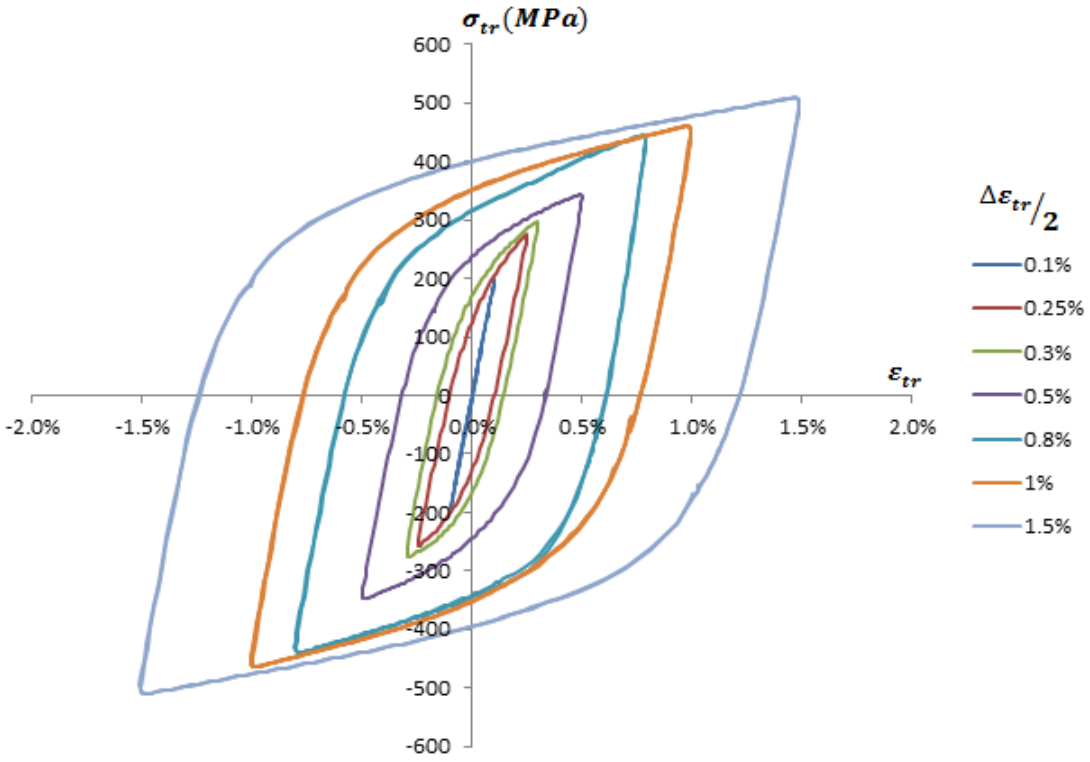

Figure 4.16: Stabilized hysteresis loops of C40 steel obtained from cyclic tension/compression tests.

To examine if the material has a cyclic hardening or softening, the maximum true stress, $\sigma_{tr_{max}}$, can be plotted over time to see if it increases (cyclic hardening) or decreases (cyclic softening). An example of this curve, corresponding to data of the test with applied strain amplitude $\frac{\Delta\varepsilon}{2} = 0.25\%$, is plotted in Figure 4.17 below. This figure shows that the maximum true stress slightly increases with time in the first cycles before reaching a constant value, which indeed means that the C40 steel hardens cyclically before stabilizing.

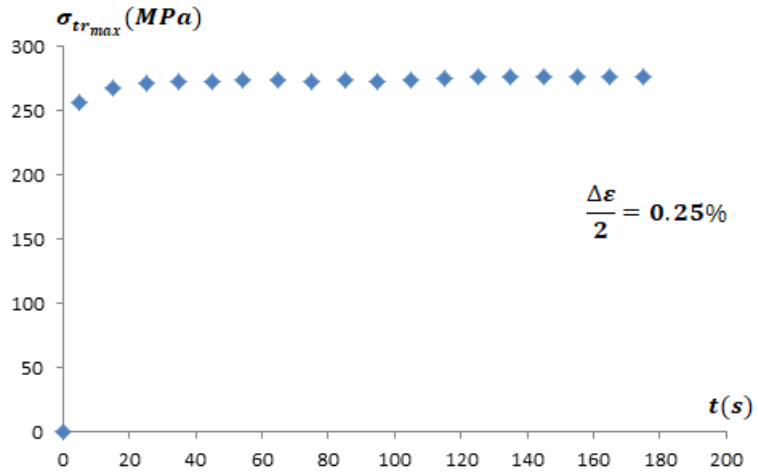

Figure 4.17: Cyclic hardening of the C40 steel observed for the test example with the applied strain amplitude $\frac{\Delta\varepsilon}{2} = 0.25\%$.

This cyclic hardening can also be confirmed by plotting the 'cyclic hardening curve', obtained from the maximum true stresses reached by the stabilized hysteresis loops of Figure 4.16 against the true strain ε_{tr}, superposed to the 'monotonic hardening curve' of the C40 steel as shown in Figure 4.18. The data points of the monotonic hardening curve are reported from [Gaudillière, 2012]. It can be seen in Figure 4.18 that the cyclic hardening curve is above the monotonic hardening curve, which indeed accounts for the cyclic hardening effect of the C40 steel.

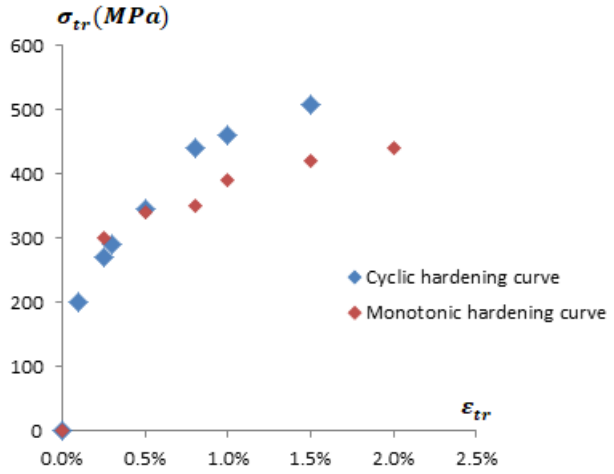

Figure 4.18: Cyclic hardening stress-strain curve in comparison with the monotonic hardening curve.

Therefore, according to the three steps presented at the end of the previous section, the non-linear kinematic hardening coefficients of the C40 steel can be determined from the experimentally obtained loops as follows:

- Figure 4.19 shows the four stabilized cycles corresponding to applied strain amplitudes 0.5%, 0.8%, 1%, and 1.5%, plotted against the plastic strain. The plasticity is more apparent in these four configurations and the coefficient, k, can then be approximated from the values of elastic domains defined with a 0.2% offset yield point with respect to the plastic strain (Figure 4.19). That roughly gives:

$$k = \frac{1}{2}\left(\frac{462.23 + 612.72 + 623.12 + 675.19}{4}\right), \tag{4.12}$$

$$= 296.66 MPa. \tag{4.13}$$

- Figure 4.20 illustrates the determination of coefficients, C and γ, with plotted data points corresponding to the applied strain amplitudes 0.5%, 0.8%, 1%, and 1.5%. The asymptotic value of, $\frac{C}{\gamma}$, is roughly determined by extrapolating the plotted data points.

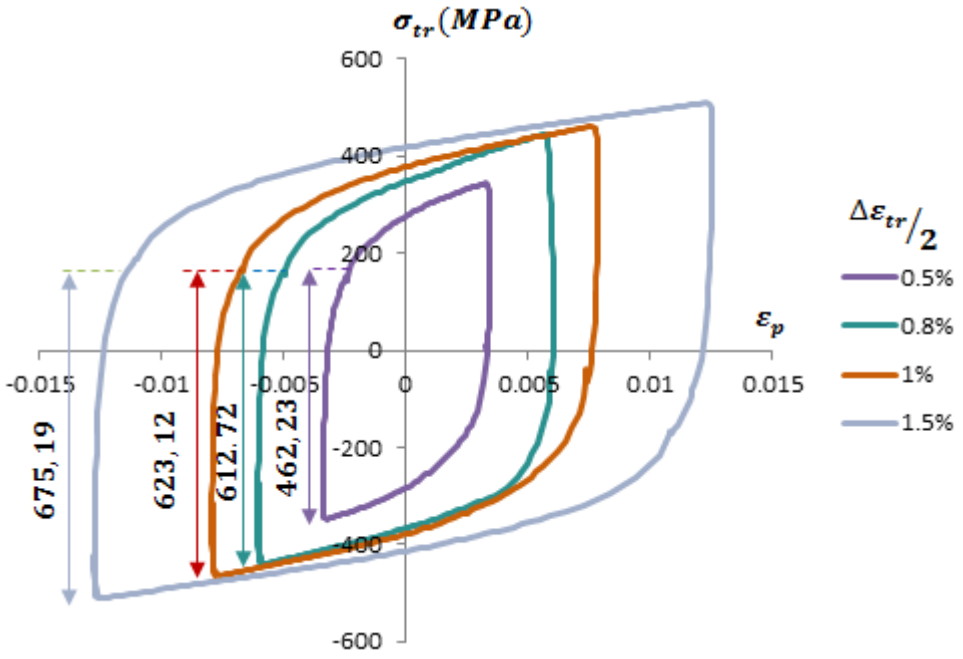

Figure 4.19: Identification of the coefficient k from stabilized stress-plastic strain curves.

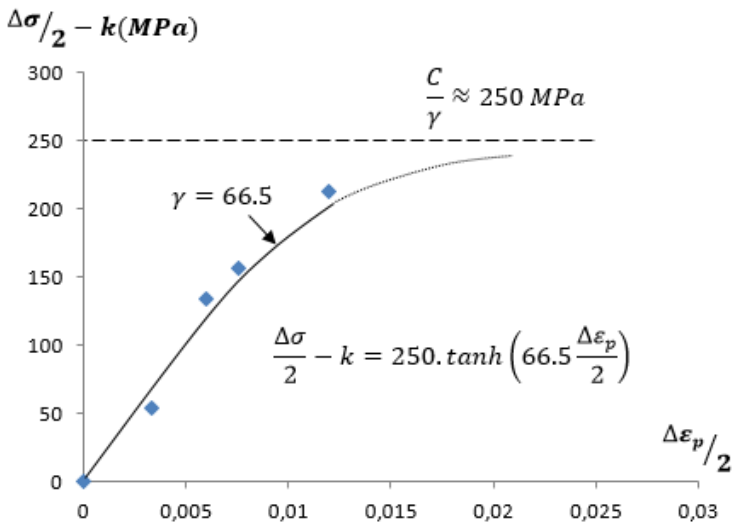

Figure 4.20: Identification of the coefficients C and γ.

Thus, with the coefficients, $k = 296.66MPa$, $C = 16625MPa$, and $\gamma = 66.5$, the non-linear kinematic hardening model of the C40 steel is fully defined and can be numerically implemented.

As mentioned earlier in this section, the software *Abaqus* is used. After numerically defining the inputs of the non-linear kinematic model characterized above, the

validity of the model was assessed through a comparison with experimental data. Figure 4.21 depicts simulated stabilized cycles compared with experimental ones for applied total strain amplitudes 1% and 1.5% since in the real application (modeling the cyclic plastic dissipation in the RCPZ during fatigue crack growth tests) the expected strain ranges are high. This comparison shows that the computed stabilized cycles fits well with the experimental curves.

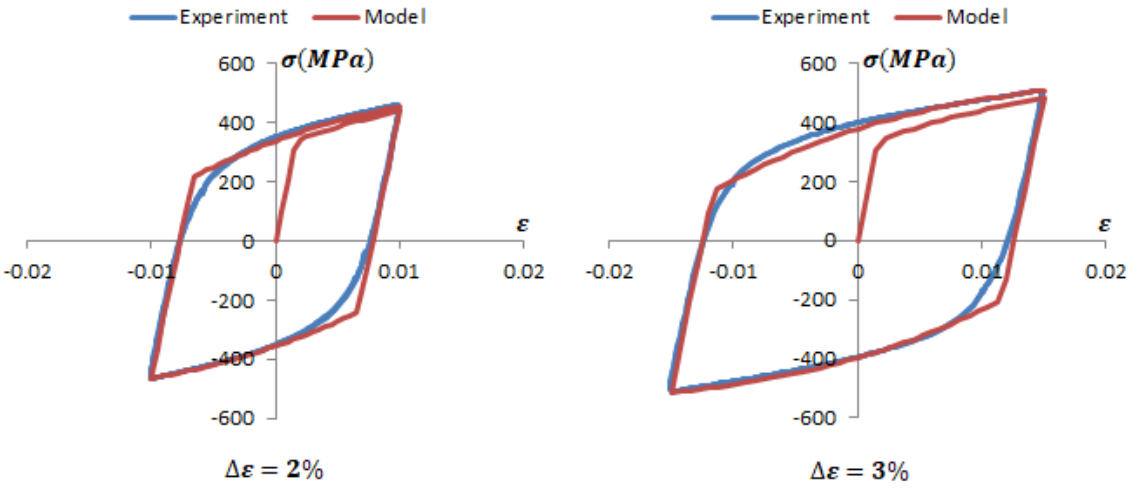

Figure 4.21: Verification of the model.

Furthermore, for the experimental and simulated curves of Figure 4.21, the cyclic plastic strain energy density, W_{cyc} (Equation (4.14)) is calculated in the one-dimensional case for determining the associated relative error between experimental data and the model.

$$W_{cyc} = \oint_{cycle} \sigma d\varepsilon_p. \tag{4.14}$$

	$\frac{\Delta\varepsilon}{2} = 1\%$		$\frac{\Delta\varepsilon}{2} = 1.5\%$	
	Experiment	Model	Experiment	Model
$W_{cyc}(MJ.m^{-3}.cycle^{-1})$	10.956	11.251	19.483	19.552

Table 4.3: Cyclic plastic strain energy density per cycle calculated for checking the accuracy of simulated curves.

According to the results reported in Table 4.3, the relative error in energy density for the case of the applied strain amplitude, $\frac{\Delta\varepsilon}{2} = 1\%$, is: $\delta_1 = \frac{11.251-10.956}{10.956} = 2.69\%$,

while that for the case of the applied strain amplitude, $\frac{\Delta\varepsilon}{2} = 1.5\%$, it is equal to: $\delta_{1.5} = \frac{19.552-19.483}{19.483} = 0.35\%$. Thus, the model gives a good agreement with experimental data.

It must be known that this non-linear kinematic model was determined from experimental data obtained with strain ranges lower than those expected in the RCPZ during fatigue crack growth tests, it is however used as an approximated model to compute, by FEA, the plastic strain energy dissipated per cycle in the RCPZ according to the conditions of conventional fatigue crack growth tests carried out in this work. The method of computing this energy as well as the corresponding results are presented in the next section.

4.2.3 Computing the cyclic plastic dissipation in the RCPZ

In order to compute the cyclic plasticity dissipated into heat in the RCPZ, q, which was previously estimated by carrying out infrared measurements during fatigue crack growth tests (*cf.* Section §2.4.3, Chapter II), the non-linear kinematic hardening model identified in the previous section is used. The aim is to carry out numerical calculation by FEA of the plastic strain energy per cycle over the RCPZ, denoted here by E_p^{cyc}, which can be expressed as:

$$E_p^{cyc} = \iiint \left(\oint (\bar{\bar{\sigma}} : d\bar{\bar{\varepsilon}}_p) \right) dV, \tag{4.15}$$

where the cyclic integral signifies the accumulation of plastic work at each point in the RCPZ over the course of a complete load cycle, while the subsequent integration over the RCPZ provides the plastic strain energy per cycle.

In the following, the quantity, E_p^{cyc}, is computed from the plastic work performed during a single load cycle on a stationary crack. With this simplifying assumption, possible plasticity-induced crack closure is intentionally neglected for simplification (such a problem has been extensively treated in the literature, [Ellyin, 1997]). Moreover, a stationary crack modeling assumption also neglects the contribution of the actual crack extension to the total plastic dissipation occurring during any given load cycle. This contribution is actually negligible in Paris-regime crack growth for ductile materials ([Klingbeil, 2003]).

Under this hypothesis, the plastic strain energy per cycle, E_p^{cyc}, is computed with the software *Abaqus 14.5* by a two-dimensional elastic–plastic finite element model of a stationary mode I crack under static amplitude loading. The applied loading conditions are those of the fatigue crack growth tests $T0XY$ carried out to experimentally estimate the cyclic plastic dissipation in heat in the RCPZ (*cf.* Table 2.4, Chapter II). The quarter model of the CCT plate specimen as well as the assumption of plane stresses are considered in this calculation. The elastic response of C40 steel is defined by $E = 210GPa$, and $\nu = 0.3$. While the cyclic plastic behavior is approximated by the non-linear kinematic hardening model previously identified.

The type of finite elements is an 8-node isoparametric quadratic and quadrilateral mesh (CPS8R, [AbaqusElements, 2012]) uniformly refined in the RCPZ region with the smallest element ahead of the crack tip measuring $40\mu m$. Moreover, reduced-integration elements are chosen for their accurate performance during nearly incompressible material response, [AbaqusElements, 2012].

Figure 4.22 shows schematic boundary conditions, due to symmetries, as well as the applied load scheme. Indeed, the load is defined as a normal stress uniformly applied over the upper edge of the specimen, by using four steps defining two load cycles, which are subdivided with a load step of 0.01 as recommended for enhancing the convergence and integration accuracy of *Abaqus* algorithms ([AbaqusAnalysis, 2012]).

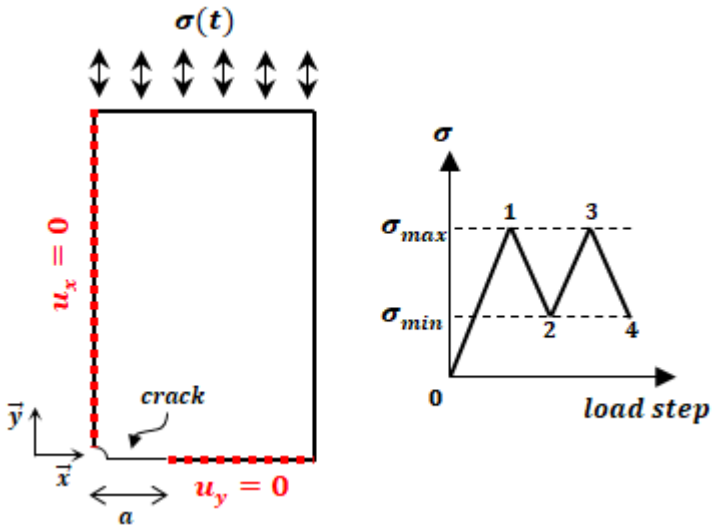

Figure 4.22: Boundary conditions and applied load steps.

Since *Abaqus* automatically computes the plastic strain energy (Equation (4.15)) during each load step by using the function 'ELPD', extraction of the plastic strain energy per cycle, in the RCPZ, from the finite element results can be done as follows:

- Compute E_p^{cyc} over the RCPZ area computed from *Abaqus* finite element solution during the second cycle, that is:

$$E_p^{cyc} = 2 \iint \left(\int_{Step\ 2}^{Step\ 4} (\bar{\bar{\sigma}} : d\bar{\bar{\varepsilon}}_p) \right) B \ \mathrm{d}A, \tag{4.16}$$

  where B is the CCT specimen thickness, and the factor 2 accounts for the use of symmetrical model with half RCPZ. It should be pointed out that two cycles are necessary because, during the first cycle, the plastic strain occurs throughout the monotonic plastic zone, while in subsequent cycles, the plastic strain occurs in the RCPZ (*cf.* Figure 1.7, Chapter I).
- Then, divide the obtained quantity, E_p^{cyc}, by the CCT plate specimen thickness, $B = 4mm$, in order to get the plastic strain energy per cycle and unit length of the crack front, denoted afterward by q^{model}, which is comparable with the experimentally estimated cyclic plastic dissipation in heat, q.

By considering configurations of crack lengths corresponding to the end of applied load blocks of the fatigue tests $T0XY$, previously presented in Table 2.4 (Chapter II), the plastic strain energy per cycle and unit length of the crack front, q^{model}, is computed by following the method explained above. The numerical results are reported in Table 4.4.

$Test\ ref.$	R	ΔK_I $(MPa.\sqrt{m})$	q $(J.m^{-1}.cycle^{-1})$	q^{model} $(J.m^{-1}.cycle^{-1})$
$T012$	0.1	16	0.17	0.13
$T013$	0.1	20	0.32	0.24
$T014$	0.1	23	0.43	0.44
$T015$	0.1	26	0.65	0.67
$T041$	0.4	13	0.23	0.04
$T042$	0.4	16	0.27	0.12
$T061$	0.6	13	0.25	0.04

Table 4.4: Experimentally estimated heat source, q, and numerically computed cyclic plastic strain energy, q^{model}

From the results in Table 4.4, it can be concluded that, for $R = 0.1$, by assuming that all the cyclic plastic strain energy in the RCPZ is dissipated in heat and responsible for the existence of the heat source q, the heat source in the RCPZ is realistic. This is in agreement with the results in [Pippan and Stüwe, 1983]. Moreover, for $R = 0.4$ and 0.6, the gap between q^{model} and q reveals a non-representative model. Further work is needed to understand this difference.

Computed data for $R = 0.1$ can be used to verify if the model predicts a ΔK^4 dependence of the cyclic plastic dissipation in the RCPZ. Indeed, Figure 4.23 shows that the computed cyclic plastic dissipation is close to that estimated by infrared measurements, especially when experimental uncertainties are considered, and the corresponding values are nearly proportional to ΔK^4.

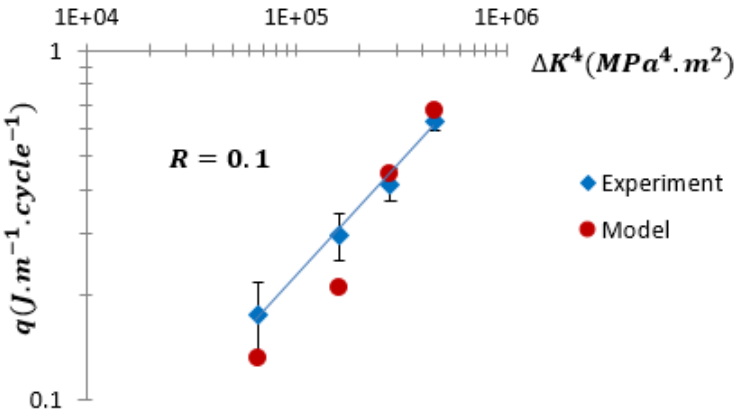

Figure 4.23: Computed and experimentally estimated cyclic plastic dissipation in heat, for $R = 0.1$, plotted against ΔK^4.

The important difference between q, and q^{model}, obtained for high load ratios, $R = 0.4$ and $R = 0.6$ (Table 4.4), may be due to the fact that cyclic tension/compression tests for determining the non-linear kinematic hardening model were carried out at $R = -1$, which is close to $R = 0.1$ and not convenient to characterize the material cyclic behavior for high load-ratios. Furthermore, cyclic tension/compression tests were carried out under strain control loading, while fatigue crack growth tests were performed under stress control loading, this may generate accumulated ratchetting strains in the RCPZ, which are not well simulated by the proposed non-linear kinematic hardening model.

However, this model can be used as a first order approximation with the applied load-ratio $R = 0.1$ in order to see if a more dissipative material exists. This is done by adjusting the non-linear kinematic hardening parameters, k, C, and γ, previously presented in the previous section. The idea is to know if such material does manifest

a more considerable cyclic plastic dissipation in the RCPZ compared to that of C40 steel, under the same loading conditions.

Having considered the following numerical values: $k = 100MPa$, $C = 800GPa$, and $\gamma = 10^4$, with the same applied loading conditions as the load block of the fatigue test $T014$ ($a = 27mm$, $\Delta K_I = 23MPa.\sqrt{m}$, $R = 0.1$), the resulting computed cyclic plastic dissipation is $q^{model} = 22.26J.m^{-1}.cycle^{-1}$. Thus, such a material would dissipate about 50 times more heat, in the RCPZ, than the C40 steel (for the test $T014$, $q = 0.43J.m^{-1}.cycle^{-1}$).

Therefore, the thermal correction, $K^q_{I_{temp}}$, due to the computed heat source, $q^{model} = 22.26J.m^{-1}.cycle^{-1}$, with the theoretical material, is computed with the resulting effects on, $K_{I_{min}}$, $K_{I_{max}}$, and the R-ratio near the crack tip. This is presented in Table 4.5. From these results, such material would generate a cyclic plastic dissipation in heat in the RCPZ with significant consequences on the SIF.

R	ΔK_I	$K_{I_{min}}$	$K_{I_{max}}$	$K^q_{I_{temp}}$	$K^{corr,q}_{I_{min}}$	$K^{corr,q}_{I_{max}}$	$R^{corr,q}$
0.1	23	2.55	25.55	-3.11	-0.56	22.44	-0.025

Table 4.5: Effects of the thermal correction, $K^q_{I_{temp}}$, due to the heat source, $q^{model} = 22.26J.m^{-1}.cycle^{-1}$, of the theoretical material.

Figure 4.24 depicts the stress-strain hysteresis loop of the theoretical material computed under the applied strain amplitude, $\frac{\Delta\varepsilon}{2} = 1.5\%$.

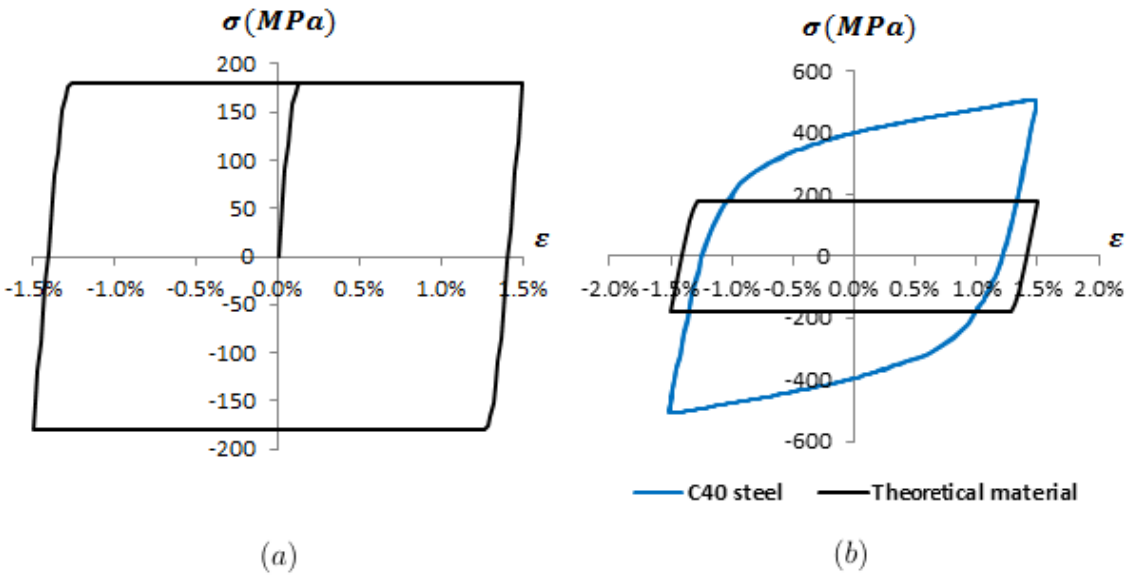

(a) (b)

Figure 4.24: (a) Hysteresis loop of the theoretical material computed at $\frac{\Delta\varepsilon}{2} = 1.5\%$. (b) Comparison with the hysteresis loop of C40 steel.

From Figure 4.24, it can be seen that, for this example of applied strain amplitude, $\frac{\Delta\varepsilon}{2} = 1.5\%$, even though the hysteresis loop of the theoretical material is less wide-open than that of C40 steel, its cyclic plastic strain energy dissipated in the RCPZ, computed above, is greater than that of C40 steel. Indeed, the cyclic yield stress of the theoretical material is lower compared to that of C40 steel, and since the size of the RCPZ is inversely proportional to the square of the cyclic yield stress, the RCPZ region in the theoretical material is greater than that of C40 steel. Therefore, even with a reduced area of hysteresis loop, in other words a low 'plastic strain energy density', the 'plastic strain energy' dissipated in the RCPZ per cycle can be high if the size of the RCPZ is large, and of course, small enough to fulfill the small scale yielding condition.

4.3 Conclusion of Chapter IV

- The experimental investigation about ultrasonic fatigue crack growth tests enabled to verify that at ultrasonic loading frequencies, the cyclic plasticity dissipated into heat in the RCPZ, q, is amplified. Moreover, it should be noted that not only the heat source, q, but also the intrinsic dissipation due to microplasticity becomes significant. In the example presented in this study, the intrinsic dissipation due to microplasticity is not taken into account, and the heat source, q, is estimated at, $q = 347.27 W.m^{-1}$, under the applied loading conditions: $1.4 \leq a \leq 1.7 mm$, $N = 2.61 \times 10^4 cycles$, $16 \leq \Delta K_{I_i} \leq 19.28 MPa.\sqrt{m}$, $f = 20119 Hz$, and $R = -1$. The value of this heat source is about 20 times greater than that estimated during the conventional fatigue test with close applied SIF range and load ratio, $\Delta K_I = 16 MPa.\sqrt{m}$ and $R = 0.1$, respectively. However, its resulting thermal correction on the SIF, $K^q_{I_{temp}} = -0.152 MPa.\sqrt{m}$, is small compared to the values of the applied SIF range. But, this result should be treated cautiously because since the heat source, q, amplifies in ultrasonic frequencies, it may be high enough, in other configurations of applied loading, to generate a considerable thermal correction on the SIF.

- With numerically correlating the cyclic plastic behavior of C40 steel with the cyclic plasticity dissipated into heat in the RCPZ (at loading frequencies $f \approx 100 Hz$), the associated constitutive model was modified to see if a material with a great cyclic plastic strain energy in the RCPZ exists. An example of the cyclic behavior of such material was computed. With the following non-linear

kinematic hardening parameters, $k = 100MPa$, $C = 800GPa$, and $\gamma = 10^4$, the cyclic plastic dissipation in heat in the RCPZ is about 50 times higher than that of C40 steel, which means that, since the calculations are linear, the resulting consequences on the SIF are also about 50 times greater than those quantified for the C40 steel. As a result, for such material, the consequences of the cyclic plasticity dissipated into heat in the RCPZ, q, on the SIF are significant and should be taken into consideration.

Conclusion and Prospects

The aim of this doctoral work was to investigate the consequences on the mode I SIF of three types of heat sources generated during fatigue crack growth tests, carried out at room temperature, in the case of a long propagating fatigue crack in a thin-flat CCT specimen made of C40 steel. These heat sources concern the thermoelastic coupling source, the intrinsic dissipation due to microplasticity, and the cyclic plasticity dissipated as heat in the RCPZ ahead of the crack tip. The first step was to assess these heat sources. The thermoelastic coupling source was then computed within the framework of linear-isotropic thermoelasticity. The intrinsic dissipation was approximated with a specific method based on experimental results of self-heating fatigue tests. And the cyclic plastic dissipation in heat in the RCPZ was experimentally estimated from infrared measurements conducted during fatigue crack growth tests. The second step was to separately compute the temperature fields generated by each heat source by using the linearity of the heat diffusion problem. Then, the third step was to solve the stress field, within the hypothesis of LEFM, corresponding to each thermal effect and leading to calculate the associated three types of thermal corrections on the mode I SIF. As a result, the following conclusions can be drawn:

- The three types of heat sources studied in this work have negligible impacts on the SIF during fatigue crack growth tests conducted at loading frequencies close to $100Hz$.

- Although the thermal consequences on the SIF are small at this scale of loading frequencies ($f \approx 100Hz$), the thermal effect related to the cyclic plasticity dissipated as heat in the RCPZ has a relatively greater impact on the SIF compared to the effects due to the thermoelastic coupling source and the intrinsic dissipation.

- Not only the SIF, but also the parameters associated with fatigue crack growth tests, namely: the SIF range, the minimum and maximum values of the SIF, and the R-ratio, are modified because of these thermal effects. Indeed, the

thermoelastic coupling source tends to increase the SIF range by increasing the SIF maximum value and decreasing its minimum value, while it decreases the initial value of the applied R-ratio near the crack tip. The two remaining dissipative heat sources, do not change the SIF range, but both decrease the minimum and maximum values of the SIF as well as the R-ratio near the crack tip.

- By taking into consideration the overall thermal effects on the SIF, the resulting consequences on the minimum and maximum values of the SIF as well as the value of R-ratio, increase, particularly the consequence on the R-ratio when its initial applied value is low ($R = 0.1$) and the applied SIF range gets higher ($16 \leq \Delta K_I \leq 26MPa.\sqrt{m}$).

- By considering the thermal effect on the R-ratio due to the cyclic plastic dissipation in heat in the RCPZ, the fatigue crack growth rate tends to increase, but this increase remains negligible for the material used in this work (C40 steel) at loading frequencies $f \approx 100Hz$.

- To get an important impact on the fatigue crack growth rate, for example modifying its initial value by 10%, the cyclic plasticity dissipated as heat in the RCPZ should be 10 times greater than that obtained with the C40 steel at the loading frequency, $f = 100Hz$, the applied SIF range, $\Delta K_I = 26MPa.\sqrt{m}$, and the applied load ratio $R = 0.1$. For that purpose, two effects associated with the loading frequency and the material behavior on the cyclic plastic dissipation in heat in the RCPZ, are carried out at the end of this doctoral work.

- The effect of the loading frequency on the cyclic plastic dissipation in heat in the RCPZ aimed to launch a new line of research work leading to investigate the thermal correction on the SIF at the scale of ultrasonic frequencies since they generate considerable thermal effects. In the study presented in this thesis, only the thermal effect related to cyclic plastic dissipation in heat in the RCPZ is considered. It was experimentally estimated from infrared measurements during ultrasonic fatigue crack growth tests conducted with loading frequencies of about $20kHz$. Many technical obstacles have been encountered during this experimental investigation, particularly fast crack propagation at high applied SIF ranges, making the condition of applying a constant SIF range during one load block difficult to fulfill, and the significant intrinsic dissipation effect due to microplasticity occurring outside the RCPZ at low applied SIF ranges,

which prevents the observation of the increase of temperature at the crack tip. However, it was possible to use infrared data of one applied ultrasonic fatigue crack growth test to confirm the amplification, in the ultrasonic regime, of the cyclic plasticity dissipated as heat in the RCPZ. According to the loading conditions, $f = 20119Hz$, $\Delta K_{I_i} = 16MPa.\sqrt{m}$, and $R = -1$, the cyclic plastic dissipation in heat is estimated at $q = 347.27W.m^{-1}$, which is about 20 times greater than that estimated during a fatigue crack growth test carried out at $f = 100Hz$ with a close loading configuration ($\Delta K_{I_i} = 16MPa.\sqrt{m}$, and $R = 0.1$).

- In order to find the class of materials with a considerable cyclic plastic dissipation in heat in the RCPZ, a numerical correlation between this thermal effect and the cyclic plastic behavior of C40 steel is first established. The aim was to implement a cyclic plastic behavior model enabling to predict the heat dissipated by cyclic plasticity in C40 steel, and then use this model for finding characteristics of potential materials which would dissipate more heat, in the RCPZ, compared to C40 steel. For such materials, thermal corrections on the SIF would be more significant contrary to what has been reported with the C40 steel. By way of conclusion of this last study, a material with low cyclic yield stress ($\approx 100MPa$), high kinematic hardening modulus ($\approx 800GPa$), and high rate of kinematic hardening ($\approx 10^4$), would have a RCPZ 50 times more dissipative than that of C40 steel under applied SIF range, $\Delta K_I = 23MPa.\sqrt{m}$, and applied R-ratio, $R = 0.1$.

In addition to these conclusions, it should be reminded that the calculations presented in this thesis fulfilled the LEFM assumption of small scale yielding because the SIF is calculated as a LEFM parameter. This condition may be seen as the main limitation of this work since when the crack ligament yielded during fatigue crack growth tests under high applied SIF ranges and R-ratios, the tests were not exploitable, while it turned out that those tests generate more considerable thermal effects which could consequently impact the SIF. That is why, potential further work would be to use a new calculation method of the SIF under large scale yielding.

Additional work should also be done in order to overcome the problems encountered during ultrasonic fatigue crack growth tests, especially developing a new estimation method of heat sources enabling to properly quantify the cyclic plastic dissipation in heat in the RCPZ as well as the intrinsic dissipation due to microplasticity which is not negligible in the ultrasonic regime. Moreover, decoupling the thermomechanical problem, with the decomposition considered in this work for

loading frequencies around $100Hz$, may no longer be valid because of the high thermomechanical coupling order generated by the dynamic effect due to ultrasonic frequencies. This remains to be confirmed, otherwise, a new methodology with new hypothesis adapted to solve the thermal corrections of the SIF in the ultrasonic regime is needed.

A last prospect would be to find a real material with a cyclic behavior close to the simulated one proposed in the last conclusion above because in such a case, the thermal corrections on the SIF become significant and can have a more apparent impact on the extension of long propagating fatigue cracks.

References

AbaqusAnalysis. Analysis procedures, solution, and control. *Abaqus Analysis User's Manual*, 6.12, 2012.

AbaqusElements. General-purpose continuum elements. *Abaqus Analysis User's Manual*, 6.12, 2012.

AbaqusPlasticity. Models for metals subjected to cyclic loading. *Abaqus Analysis User's Manual*, 6.12, 2012.

AnsysFracture. Post1 - crack analysis. *Mechanical APDL Command Reference*, 19.8., 2010.

D. S. Antolovich, A. Saxena, and G. Chanani. A model for fatigue crack propagation. *Eng. Frac. Mech.*, 7:649–652, 1975.

ASTM-E647. Standard test method for measurement of fatigue crack growth rates. *Standard ASTM E647 - 13e1*, 2013.

C. Bathias and P. C. Paris. *Gigacycle Fatigue in Mechanical Practice*. Marcel Dekker, New York, 2005.

B. Berthel, B. Wattrisse, A. Chrysochoos, and A. Galtier. Thermographic analysis of fatigue dissipation properties of steel sheets. *International Conference on Photomechanics*, 43:273–279, 2007.

T. Boulanger, A. Chrysochoos, A. Mabru, and A. Galtier. Calorimetric analysis of dissipative and thermoelastic effects associated with the fatigue behavior of steels. *International Journal of Fatigue*, 2004.

W. Brocks. *Plasticity and Fracture*, volume 244. Springer, 2017.

D. Broek and J. Schijve. Report number nlr-tr-101-361. *National Aeronautical and Astronautical Research Institute, Amsterdam*, 1963.

J. D. Bryant, D. D. Makel, and H. G. F. Wilsdorf. Observations on the effect of temperature rise at fracture in two titanium alloys. *Mater. Sci. Engn.*, 77:85–93, 1986.

H. F. Bueckner. The propagation of cracks and the energy of elastic deformation. *Trans ASME*, 80E:1225–1230, 1958.

H. F. Bueckner. A novel principle for the coputation of stress intensity factors. *ZAMM*, 50:529–545, 1970.

H. F. Bueckner. Weight functions for the notched bar. *ZAMM*, 51:97–109, 1971.

F. M. Burdekin and D. E. W. Stone. The crack opening displacement approach to fracture in yielding materials. *Journal of Strain Analysis for Engineering Design*, 1:145–153, 1966.

E. Byskov. The calculation of stress-intensity factors using the finite-element method with cracked elements. *International Journal of Fracture Mechanics*, 6:159–167, 1970.

A. Capatina and R. Stavre. Algorithms and convergence results for an inverse problem in heat propagation. *International Journal of Engineering Science*, 38: 575–587, 2000.

D. J. Cartwright. Stress intensity factor determination, developments in fracture mechanics (chapter 2). *G. G. Chell (Ed.), London, England: Applied Science Publishers Ltd.*, pages 29–66, 1979.

D. J. Cartwright and D. P. Rooke. Green's functions in fracture mechanics. *Royal Aircraft Establishment*, 1980.

S. K. Chan, I. S. Tuba, and W. K. Wilson. On the finite element method in linear fracture mechanics. *Eng. Frac. Mech.*, 2:1–17, 1970.

A. Chrysochoos and H. Louche. An infrared image processing to analyse the calorific effects accompanying strain localisation. *International Journal of Engineering Science*, 38:1759–1788, 2000.

A. Chrysochoos, T. Boulanger, and A. E. Morabito. Dissipation and thermoelastic coupling associated with fatigue of materials. *M. Frémond and F. Maceri, Mechanics, Models and Methods in Civil Engineering*, pages 147–156, 2012.

R. J. Cooke, P. E. Irving, G. S. Booth, and C.J. Beevers. The slow fatigue crack growth and threshold behaviour of a medium carbon alloy steel in air and vacuum. *Eng. Fract. Mech.*, 7:69–77, 1975.

W. Döll. An experimental study of the heat generated in the plastic region of a running crack in different polymeric materials. *Eng. Frac. Mech.*, 5:259–268, 1973.

D. Dugdale. Yielding of steel sheets containing slits. *Journal of the Mechanics and Physics of Solids*, 8, 1960.

W. Elber. Fatigue crack closure under cyclic tension. *Eng. Frac. Mech.*, 2:37–45, 1970.

W. Elber. The significance of fatigue crack closure. *Damage Tolerance in Aircraft Structures*, pages 230–242, 1971.

F. Ellyin. Fatigue damage, crack growth and life prediction. *NY: Chapman and Hall*, 1997.

B. Farahmand and K. Nikbin. Predicting fracture and fatigue crack growth properties using tensile properties. *Eng. Fract. Mech.*, 75:2144–2155, 2008.

W. Farren and G. Taylor. The heat developed during plastic extension of metals. *Proc Roy Soc A*, pages 422–451, 1925.

Katharine M. Flores and Reinhold H. Dauskardt. Local heating associated with crack tip plasticity in zr-ti-ni-cu-be bulk amorphous metals. *J. Mater. Res.*, 14: 638–643, 1999.

K. N. G. Fuller and P. G. Fox. The temperature rise at the tip of fast-moving cracks in glassy polymers. *Proc. R. Soc. London*, A 341:537–557, 1975.

D. Gan and J. Weertman. Fatigue crack closure after overload. *Eng. Frac. Mech.*, 18:155–160, 1983.

C. Gaudillière. *Cisaillage à grande vitesse: des essais à la simulation.* PhD thesis, Arts et Métiers ParisTech, 2012.

P. Germain, Q. Son Nguyn, and P. Suquet. Continuum thermodynamics. *Journal of Applied Mechanics*, 105:1010–1020, 1983.

G. Green. An essay on the application of mathematical analysis to the theories of electricity and magnetism. *Nottingham, England: T. Wheelhouse*, 1828.

A. A. Griffith. The phenomena of rupture and flow in solids. *Philosophical Transactions of the Royal Society of London*, 221:163–198, 1920.

A.K. Head. The growth of fatigue cracks. *Philosophical Magazine*, 44:925–938, 1953.

J. A. Hult and F. A. McClintock. Elastic-plastic stress and strain distribution around sharp notches under repeated shear. *9th International Congress on Applied Mechanics*, 8, 1956.

G. R. Irwin. Analysis of stresses and strains near the end of a crack transversing a plate. *Journal of Applied Mechanics*, 24:361–364, 1957.

G. R. Irwin. Plastic zone near a crack tip and fracture toughness. *Sagamore Ordnance Material Conference*, 4:63–78, 1960.

M. Katcher and M. Kaplan. Effects of r-factor and crack closure on fatigue crack for alluminium and titanium alloys. *ASTM STP 559*, 6:264–282, 1974.

N. W. Klingbeil. A total dissipated energy theory of fatigue crack growth in ductile solids. *International Journal of Fatigue*, 25:117–128, 2003.

J. Lemaitre and JL. Chaboche. *Mechanics of Solid Materials*. Cambridge University Press, 1990.

M. P. Luong. Infrared thermographic scanning of fatigue in metals. *Nuclear Engineering and Design*, 158:363–376, 1995.

T. Mura and C. T. Lin. Theory of fatigue crack growth for work hardening materials. *International Journal of Fracture*, 10:284–287, 1974.

Y. Murakami. Stress intensity factors handbook. *Oxford, Pergamon press*, 1987.

N. I. Muskhelishvili. Some basic problems of the mathematical theory of elasticity: Fundamental equations, plane theory of elasticity, torsion and bending. *Pennsylvania State University*, 1953.

A. Ohta, M. Kosuge, and E. Sasaki. Fatigue crack closure over the range of stress ratios from -1 to 0.8 down to stress intensity threshold level in ht80 steel and sus304 stainless steel. *International Journal of Fracture*, 14:251–264, 1978.

P. C. Paris and F. Erdogan. A critical analysis of crack propagation laws. *Journal of Basic Engineering*, 85:528–534, 1960.

R. Pippan and H. P. Stüwe. Thermische bestimmung der plastischen deformation um die rissfront eines ermüdungsbruches. *Zeitschrift für Metalkunde*, pages 699–704, 1983.

R. Pippan and H. P. Stüwe. On the energy balance of fatigue crack growth. *Computers and Structures*, 44:13–17, 1992.

R. Pippan and H.P. Stüwe. The heat produced around the fatigue crack tip near the threshold stress intensity. *2nd International Conference on Fatigue and Fatigue Thresholds*, 1984.

J. H. Poynting and Sir J. J. Thomson. A text-book of physics, vol i: Properties of matter. *Charles Griffin Company, London*, Ch. xv, 1913.

N. Ranc, D. Wagner, and P.C. Paris. Study of thermal effects associated with crack propagation during very high cycle fatigue tests. *Acta Mater*, pages 4012–21, 2008.

N. Ranc, T. Palin-Luc, and P.C. Paris. Thermal effect of plastic dissipation at the crack tip on the stress intensity factor under cyclic loading. *Engineering Fracture Mechanics*, 78:961–972, 2011.

N. Ranc, T. Palin-Luc, P.C. Paris, and N. Saintier. About the effect of plastic dissipation in heat at the crack tip on the stress intensity factor under cyclic loading. *International Journal of Fatigue*, 58:56–65, 2014.

J. R. Rice. Plastic yielding at a crack tip. *1st International Conference on Fracture, Sendai, Japan*, pages 283–308, 1965.

J. R. Rice. *Fatigue Crack Propagation. The mechanics of crack tip deformation and extension by fatigue.* ASTM Special Technical Publication 415. Philadelphia, 1967.

J. R. Rice. A path independent integral and the approximate analysis of strain concentration by notches and cracks. *Journal of Applied Mechanics*, 35:379–386, 1968.

R.O. Ritchie. Near-threshold fatigue-crack propagation in steels. *International Metals Reviews*, 5 and 6:205–230, 1979.

D. P. Rooke and D. J. Cartwright. Compendium of stress intensity factors. *HMSO*, 1976.

P. Rosakis, A. J. Rosakis, G. Ravichandran, and J. Hodowany. A thermodynamic internal variable model for the partition of work into heat and stored energy in metals. *Journal of the Mechanics and Physics of Solids*, 48:581–607, 2000.

A. Saxena, Jr. Stephen Hudak, and G. M. Jouris. A three component model for representing wide range fatigue crack growth data. *Eng. fract. mech.*, 12:103–115, 1979.

T. T. Shih and R. P. Wei. A study of crack closure in fatigue. *Eng. Frac. Mech.*, 6: 19–32, 1974.

G. C. Sih. Handbook of stress intensity factors. *Institute of Fracture and Solid Mechanics, Lehigh University, Bethlehem, Pennsylvania*, 1973.

W. R. Sperr. A phenomenological approach to fatigue crack growth rate prediction. *Proc. of Fracture*, 2, 1977.

S. Suresh, C. M. Moss, and R. O. Ritchie. Paper 27b23. *Proc. 2nd Japan Institute of Metals int. symp. on hydrogen in metals, Sendai, Japan*, 1979.

H. Tada, P. C. Paris, and G. R. Irwin. *The Stress Analysis of Cracks Handbook*. 1st Ed. Del Research Corporation, Hellertown, PA, 1973.

H. Tada, P.C. Paris, and R. Geroge Irwin. *The Stress Analysis of Cracks Handbook*. ASME Press, Three Park Ave, New York 10016, third edition, 2000.

G. Taylor and H. Quinney. The latent energy remaining in a metal after cold working. *Proc Roy Soc A*, pages 307–26, 1934.

W. Thomson. On thermoelastic and thermomagnetic properties of matter. *Quaterly Journal of Mathematics*, 1:57–77, 1857.

D. M. Tracey. Finite elements for determination of crack-tip elastic stress-intensity factors. *English Fracture Mechanics*, 3:255–265, 1971.

J. Weertman. Theory of fatigue crack growth based on a bcs crack theory with work hardening. *International Journal of Fracture*, 9:125–131, 1973.

R. Weichert and K. Schönert. Heat generation at the tip of a moving crack. *J. Mech. Phys. Solids*, 26:151–161, 1978.

H. M. Westergaard. Bearing pressures and cracks. *Journal of Applied Mechanics*, 6: 49–53, 1939.

W. K. Wilson. Some crack tip finite elements for plane elasticity. *ASTM STP 513*, pages 90–105, 1972.

W. K. Wilson and I. W. Yu. The use of the j-integral in thermal stress crack problems. *International Journal of Fracture*, 15:377–387, 1979.

T. Wu and C. Bathias. Application of fracture mechanics concepts in ultrasonic fatigue. *Eng. Frac. Mech.*, 47:683–690, 1994.

H. Ziegler. A modification of prager's hardening rule. *Quarterly of Applied Mathematics*, 17:55–65, 1959.

Conséquences des effets thermiques générés pendant la propagation d'une fissure de fatigue sur le facteur d'intensité des contraintes en mode I

RESUME :

Lors du chargement cyclique d'une pièce métallique fissurée, un champ de température hétérogène est créé à la pointe de la fissure. Ce champ de température est dû à trois types de sources de chaleur : (i) la première source est une source de couplage thermoélastique liée à la partie hydrostatique du tenseur des contraintes résultant de la sollicitation mécanique cyclique. Elle fluctue périodiquement dans le temps et l'énergie qui lui est associée est nulle à la fin de chaque cycle de chargement ; (ii) la deuxième source de chaleur est une source dissipative et intrinsèque au comportement du matériau. Elle est reliée au phénomène de l'auto-échauffement dû à la microplasticité dissipée en chaleur dans le matériau à l'échelle microscopique. Elle est positive et s'accumule dans le temps ; (iii) enfin, la troisième source de chaleur a les mêmes origines et propriétés que la deuxième source, mais elle est associée à la plasticité, à l'échelle macroscopique, qui se dissipe en chaleur dans la zone de plasticité cyclique à la pointe de la fissure. En présence de ces trois sources de chaleur, le champ de température résultant génère un champ de contrainte dû au phénomène de la dilatation thermique. Ce nouveau champ des contraintes s'ajoute au champ des contraintes dû au chargement mécanique cyclique, et donc l'état des contraintes sur la fissure est modifié. En conséquence, le facteur d'intensité des contraintes, qui est un paramètre clé dans la modélisation de la propagation des fissures, est modifié. D'où l'objectif de cette thèse qui vise à quantifier les conséquences de ces trois sources de chaleur sur le facteur d'intensité des contraintes, et ce dans le cas d'une fissure longue de fatigue.

Mots clés : Facteur d'intensité des contraintes, Couplage thermoélastique, Dissipation intrinsèque, Plasticité cyclique, Fatigue, Propagation des fissures.

Consequences of the thermal effects generated during fatigue crack growth on the mode one stress intensity factor

ABSTRACT :

By subjecting a cracked specimen to a cyclic loading, thermal effects take place and create a heterogeneous temperature field around the crack tip. Those thermal effects are associated with coupling and dissipative heat sources, namely: (i) the heat source due to thermoelastic coupling generated by the hydrostatic part of the stress tensor related to cyclic mechanical loading; (ii) the heat source due to intrinsic dissipation associated with the self-heating phenomena originating from plasticity at the microscopic scale; (iii) and the heat source due to cyclic plasticity, at the macroscopic scale, which occurs in the reverse cyclic plastic zone ahead of the crack tip, and dissipates into heat. The overall heterogeneous temperature field resulting from the heat sources induces a heterogeneous stress field due to thermal expansion phenomena. As a consequence, the stress state over the crack is modified and leads to modify the stress intensity factor, which is a key parameter in modeling fatigue crack growth. Therefore, the aim of this PhD thesis is to quantify the consequences of the heat sources on the stress intensity factor, in the case of a long propagating fatigue crack.

Keywords : Stress intensity factor, Thermoelastic coupling, Intrinsic dissipation, Cyclic plasticity, Fatigue, Crack propagation.

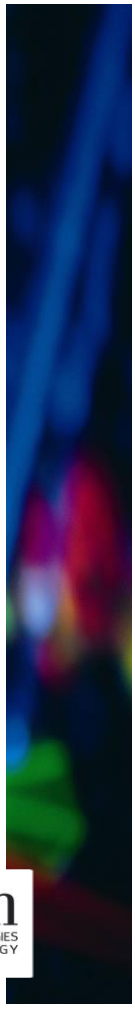

ARTS ET MÉTIERS ParisTech

ParisTech INSTITUT DES SCIENCES ET TECHNOLOGIES PARIS INSTITUTE OF TECHNOLOGY